UNIVERSITÀ DEGLI STUDI di NAPOLI FEDERICO II

PhD School in Earth Science

Doctorate in Earth, Environmental and Resources Science

XXXII cycle

PhD Thesis

MHODE Inversion of potential fields of complex structures

Ivano Pierri

Tutor
Prof. Maurizio Fedi
Prof. Giovanni Florio

Co-tutor:
Prof. Dimitrios Tsoulis

PhD Coordinator:
Prof. Maurizio Fedi

2018-19

CONTENTS

INTRODUCTION

Geophysical exploration helps solving practical environmental, engineering or exploration problems. When more detailed information about the subsurface is needed, quantitative models need to be calculated mainly through inversion algorithms. In integrate exploration geophysics gravity data are often used to investigate the edges and bottom part of causative bodies, such as salt domes, while constraining the top part of the body from seismic information.

The goal of the inverse problem is to determine the distribution of the physical property or the main geometrical features of the source distribution properties that give rise to the data. Unfortunately, this is not completely possible in practical surveys because only a limited number of data can ever be measured, and problems are not inherently unique. So, in order the calculated solution could more likely represent the true subsurface structure, we need other information about the source distribution.

The main objective of this thesis is to reconstruct complex geometric structures from gravity data, following an approach based on inverting not the gravity data themselves but a derived quantity, the scaling function (Fedi, 2005). The approach has been defined in previous papers, referred to as the MHODE method (Fedi et al., 2015), and its application to 2D gravity profiles demonstrated its efficacy (Chauhan, Fedi & Sen, 2018). We here extend the method to the 2.x D case and to the 3D case.

In the first chapter we introduce some general aspects of potential field theory, of most interest to this thesis.

In chapter 2 we introduce the MHODE method (Multi HOmogeneity Depth Estimation) (Fedi et al., 2015) from a theoretical point of view. This method concerns the homogeneity properties of complex models, namely a multi-homogeneous model. This is done using the scaling function data, because it has the main advantage of being not dependent on the density, but only on the geometric features.

Then, in chapter 3, we focus on the definition of the 2.5D, 2.x D (Rasmussen & Pedersen, 1979), and 3D forward problems (Tsoulis, 2012). In contrast to the 2D case, this type of problems allows us to consider a finite strike length for the sources and so to manage the symmetry of the profile with respect to the source in correct way. 2-D formulae were early established by Talwani and Heirtzler (1964), while 2.5D ones were established by Shuey and Pasquale (1973). Rasmussen & Pedersen (1979) determined for cases 2.5D and 2.x D formulae to calculate the gravity field, the

first-order vertical derivative for the gravity field and the magnetic field. In conformity with this work, starting from the same formulae by Rasmussen & Pedersen, we calculated the second-order and the third-order vertical derivatives for the gravity field, and the first-order and second-order derivatives of the vertical component of magnetic field.

In chapter 4 we look more in depth at the inversion, more specifically the VFSA optimization method (Very Fast Simulated Annealing). VFSA is a global optimization algorithm adapted on thermodynamic processes, on establishing how a molten material could cross different states to cool down or to reach the state of equilibrium. The main state of this process is the state of balance. If the cooling is very rapid, we will meet a local minimum. If, on the other hand, the process reaches equilibrium slowly, we will find global minimum (Sen & Stoffa, 2013).

In the 5th and 6th chapters we apply, for a synthetic case and for a real case respectively, a 3D inversion with *a priori* conditions starting from 2.x D MHODE inversion. In the first case, we start from the 2.x D interpretation of data generated by a 3D polyhedral model, thanks to a formula developed by Tsoulis (2012), whose FORTRAN code has been translated to the MATLAB environment. We defined a set of 2.x D gravity field profiles and its first order derivatives. By the MHODE inversion, the VFSA (Very Fast Simulated Annealing) inversion algorithm solves an equations system that has only geometric unknowns, because the scaling function has the peculiarity of not depending on the density. In the real case, we used the data taken from an existing gravity dataset from the Nevada Test Site (Ponce, 1997). We extracted eight parallel profiles and inverted them with the 2.x D MHODE method. These models and the estimated average density contrast constituted the main *a priori* information for the 3D inversion We so obtained a 3D density model, interpreted as a paleozoic dolomitic-quartzitic basement, buried under alluvial and cenozoic tuff deposits.

Finally, in the 7th chapter we discuss about the work on the model uncertainty for the scaling function inversion of potential fields.

CHAPTER 1. POTENTIAL FIELDS THEORY (hints)

This chapter describes some general aspects of potential theory of most interest to this thesis. In physics the *potential theory* describes not only the gravitational attraction but also a large class of phenomena, including magnetostatic and electrostatic fields, fields generated by uniform electrical currents, steady transfer of heat through homogeneous media, steady flow of ideal fluids, the behaviour of elastic solids, probability density in random-walk problems, unsteady water-wave motion, and the theory of complex functions and conformal mapping (Blakely, 1996).

1.1 Potential Fields

A *field* is a function of space and time. Fields can be classed as either *scalar* or *vector.* A scalar field is a single function of space and time; a vector field, such as flow of heat, velocity of a fluid, and gravitational attraction, must be characterized by three functions of space and time, namely, the components of the field in three orthogonal directions. However, in many cases only a component of the vector field is measured.

For example, gravimeters used in geophysical surveys only measure the vertical component g_z (a scalar field) of the acceleration of gravity $\mathbf{g}$ (a vector field).

1.2 Newtonian Potential

According to Newton's law of gravitational attraction, the magnitude of the gravitational force between two masses is proportional to each mass and inversely proportional to the square of their distance. In cartesian coordinates (Figure 1.1), the mutual force between a particle of mass m centred at point $P' = (x', y', z')$ and a particle of mass m_0 at $P = (x, y, z)$ is given by

$$F = \gamma \frac{m m_0}{r^2} \tag{1.1}$$

where

$$r = [(x - x')^2 + (y - y')^2 + (z - z')^2]^{\frac{1}{2}} \tag{1.2}$$

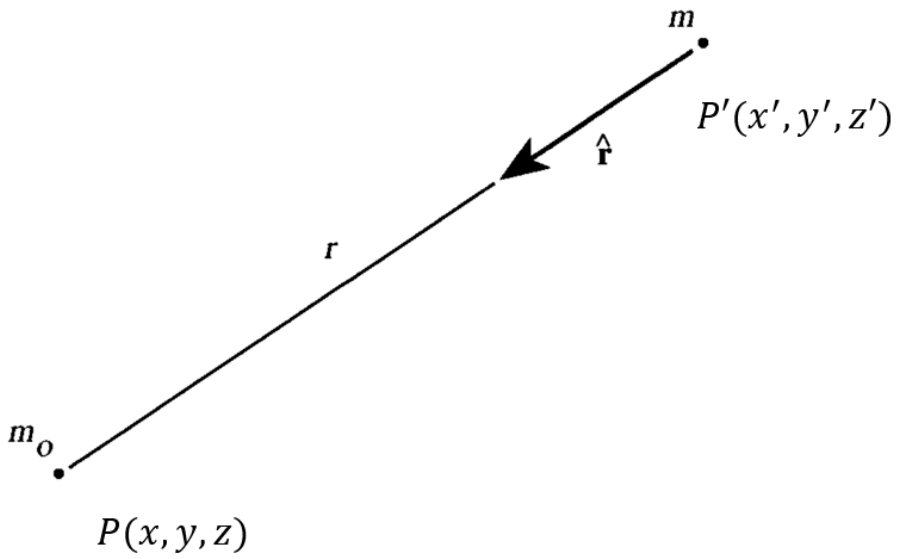

Figure 1.1 – Masses m and m_0 experience a mutual gravitational force which is proportional to m, m_0 and r^{-2}. By convention, unit vector $\hat{\mathbf{r}}$ is directed from the gravitational source to the observation point, which in this case is located at test mass m_0 (modified from Blakely, 1996).

and where γ is the Newton's gravitational constant. If we let mass m_0 be a test particle with unit-mass, then dividing the force of gravity by m_0 provides the gravity field, expressing the gravitational attraction produced by mass m at the location of the test particle:

$$\mathbf{g}(P) = -\gamma \frac{m}{r^2} \hat{\boldsymbol{r}} \tag{1.3}$$

where $\hat{\boldsymbol{r}}$ is the unit vector directed from the mass m to the observation point P, that is, in cartesian coordinates:

$$\hat{\boldsymbol{r}} = \frac{1}{|\boldsymbol{r}|}\left[(x - x')\hat{\mathbf{i}} + (y - y')\hat{\mathbf{j}} + (z - z')\hat{\mathbf{k}}\right] \tag{1.4}$$

The minus sign in equation 1.4 is necessary because of the convention that $\hat{\boldsymbol{r}}$ is directed from the source to the observation point, opposite in sense to the gravitational attraction. Because $\mathbf{g}$ is force divided by mass, it has units of acceleration and is called *gravitational acceleration*.

Gravity field, as described by equation 1.4, is irrotational because

$$\nabla \times \mathbf{g} = 0 \tag{1.5}$$

So, the field is conservative and can be represented as the gradient of a scalar potential

$$\mathbf{g}(P) = \nabla U(P) \tag{1.6}$$

where

$$U(P) = \gamma \frac{m}{r} \tag{1.7}$$

is the gravitational potential or Newtonian potential.

1.3 Gravity Method

The gravitational potential is harmonic at all the points outside of the mass, that yields $\nabla^2 U = 0$, but in the source region (the volume occupied by masses), according to Poisson's equation:

$$\nabla^2 U = -4\pi\gamma\rho \tag{1.8}$$

where ρ is the density of the mass distribution at a given point. In geophysical exploration, gravimeters measure only the vertical component of the gravity, as given by:

$$g_z = \frac{\partial U}{\partial z} \tag{1.9}$$

In the gravity method the collected data need correction for all the variation in the Earth's gravitational field, which do not result from the difference of density of the underlying rocks. When a gravimeter collects gravimetric data, they are (Blakely, 1996):

- component due to the reference ellipsoid (theoretical gravity);
- effect of elevation above sea level on the theoretical gravity (free air effect);
- effect of “topographic” mass (Bouguer slab and terrain effects).
- time-dependent variations (tidal and instrumental drift effects).
- effect of moving platform (Eötvös effect).
- effect of masses that support topographic loads (isostatic effects).
- effects from the crust density variations ("geological field").

The main objective of computing “Bouguer anomalies” is to reduce gravity measurements made on or near the Earth's surface to anomaly values that reflects density variations in the crust only.

In the Table 1, we represent the factors of gravimetric case expressed in units of International and cgs systems:

Factor	**SI**	**cgs**
Mass m	kilograms (kg)	Grams (g)
Distance r	meters (m)	Centimetres (cm)
Gravitational attraction $\mathbf{g}$	$\mathrm{m} \cdot \mathrm{sec}^{-2}$	$Gal = cm \cdot sec^{-2}$
Gravitational constant γ	$6.67 \times 10^{-11}\ \mathrm{m^3 kg^{-1} sec^{-2}}$	$6.67 \times 10^{-8}\ \mathrm{cm^3 g^{-1} sec^{-2}}$

CHAPTER 2. MHODE METHOD

2.1 Upward Continuation

One of the fundamental steps for the MHODE method is the upward continuation. The upward continuation is a technique that allows us to transform the potential field measured on a given surface in that we would have measured on another surface at an upper altitude. With upward continuation we can accentuate the anomalies caused from deep sources, decreasing the contribute of the shallow sources (Blakely, 1996).

To show how the upward continuation works, we start from the Green's third identity:

$$U(P) = -\frac{1}{4\pi}\int_{R}\frac{\nabla^2 U}{r}dv + \frac{1}{4\pi}\int_{S}\frac{1}{r}\frac{\partial U}{\partial n}dS - \frac{1}{4\pi}\int_{S}U\frac{\partial}{\partial n}\frac{1}{r}dS \qquad (2.1)$$

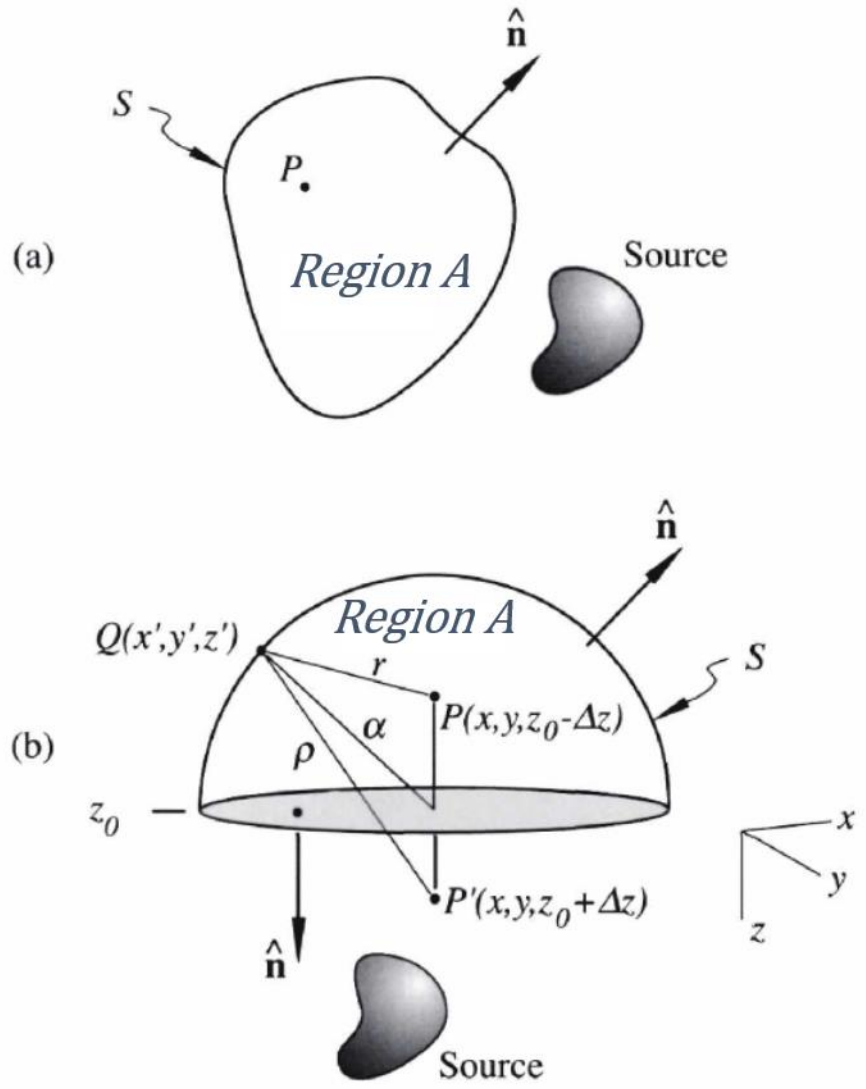

Figure 2.1 – (a) A function harmonic throughout region R can be evaluated at any point within R from its behaviour on boundary S. Unit vector h is normal to surface S. (b) Upward continuation from a horizontal surface. Potential field is known on horizontal plane $z = z_0$ and desired at point $(x, y, z_0 - \Delta z)(\Delta z > 0)$. Surface S consists of the horizontal plane plus a hemispherical cap of radius α. Point P' is the mirror image of P projected through the plane. The point of integration Q is on surface S, and r and ρ denote distance from Q to P and from Q to P', respectively (modified from Blakely, 1996).

We see that if U is harmonic and has continuous derivatives, hence for the Green's third identity the value of U at any point P within A (called free-source or harmonic region) is given by:

$$U(P) = \frac{1}{4\pi} \int_S \left[\frac{1}{r} \frac{\partial U}{\partial n} - U \frac{\partial}{\partial n} \frac{1}{r} \right] dS \qquad (2.2)$$

where S represents the boundary of A, n is the outward normal direction, and r is the distance from P to the point of integration on S. From this equation, assuming a half-space source

volume, it is well known (Blakely (1996) eq. 2.39) that we may, with some algebra, obtain the well-known upward continuation formula:

$$U(x', y', -\Delta z) = \frac{\Delta z}{2\pi} \int_S \frac{U(x, y, 0)}{(x - x')^2 + (y - y')^2 + \Delta z^2} dxdy \qquad (2.3)$$

where S is an infinitely extended plane surface, Δz is the difference from the altitudes of the measurement plane, with points of coordinates $[x, y, 0]$, and any upper altitude plane with points of coordinates $[x', y', -\Delta z]$.

To sum up, the important meaning of upward continuation is that a potential field can be calculated at any point within a region from the behaviour of the field on a surface enclosing the region. No knowledge is required about the sources of the field, provided they are below the measurement plane. This equation is evidently of great importance for multiscale methods, such as imaging methods, such as migration or DEXP, multiridge methods and methods based on the continuous wavelet transform, since they are expressly related to the variations of the field along the vertical axis. Among them, we are particularly interested to the MHODE (Multi Homogeneity Depth Estimation) method, which is heavily based on the multiscale properties of potential fields.

2.2 The scaling function

DEXP, Depth from EXtreme Points (Fedi, 2007), is a method to interpret potential field data on the basis of a meaningful property of 3D potential fields. It applies to the Newtonian potential and to its n^{th}-order derivatives and will be characterized by a high-degree of stability and accuracy in retrieving the location, the type (SI), and the excess source density. The DEXP method is implemented in four stages:

1. Create a 3D data volume of the potential field. In practice, this means that data are needed both horizontally and vertically.
2. Scale the 3D field using specific laws — namely, the 3D field $f(\mathbf{r}, \mathbf{r_0})$, which originates from a source at $\mathbf{r_0}$, is transformed into a scaled field $W(\mathbf{r}, \mathbf{r_0})$.
3. Determine the depth to source, which involves a search for the extreme points of

the scaled potential field. We will show that extreme points will occur for $W(\mathbf{r}, \mathbf{r_0})$ at points $\mathbf{r}(\mathrm{x}, \mathrm{y}, \mathrm{z})$ which are symmetrical (versus the xy-plane, Figure 2.2) to $\mathbf{r_0}(x_0, y_0, z_0)$ that is, at points enjoying the meaningful correspondence $x = x_0; y = y_0;\ z = -z_0$.

4. Compute the excess mass, or the excess dipole moment intensity for the magnetic field, from the value of the scaled potential field at the extreme points. The final result will then be a depth distribution of extreme points and the computation of the excess mass and the scaling exponent.

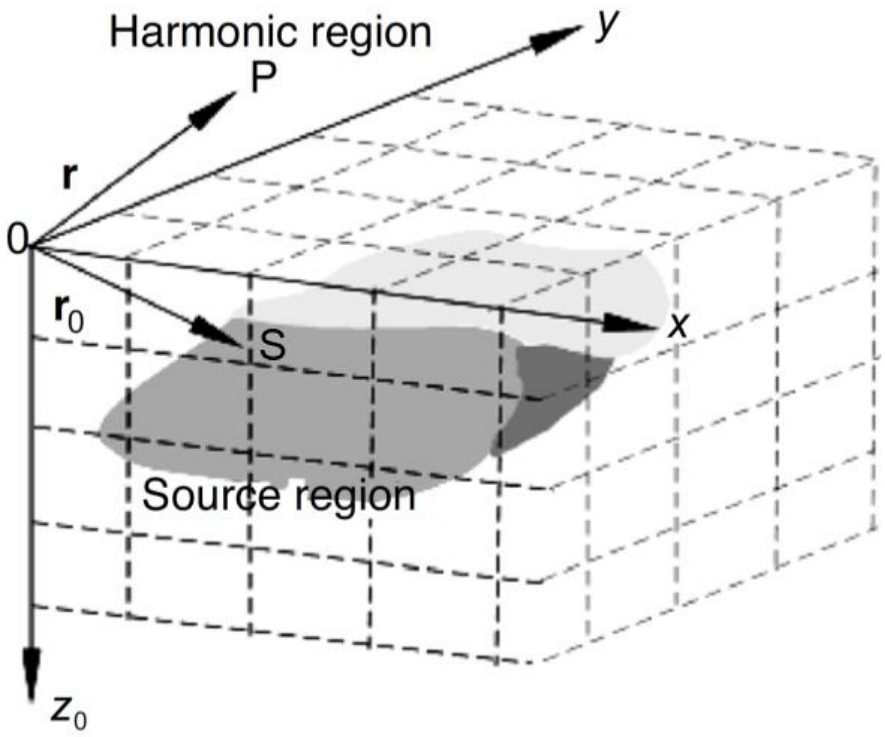

Figure 2.2 – Position vectors for DEXP transformation theory. The position vectors $\mathbf{r}$ and $\boldsymbol{r_0}$ indicate field points $P(\mathbf{r})$ in the harmonic region and source points $S(\boldsymbol{r_0})$ in the source region (modified from Fedi, 2007).

The scaling function (Fedi, 2007), was introduced in Fedi, 2005 in the context of DEXP theory. It does not depend on density or other physical constants, but only on the geometric characteristics of the model source. It is a dimensionless function of altitude that characterize the behaviour of homogeneity field. The scaling function τ is the ratio between the derivative of the logarithm of the homogeneous field g and the derivative of the logarithm of depth:

$$\tau(z) = \frac{\partial \log g}{\partial \log z} = \frac{nz}{z - z_0} \tag{2.4}$$

where n is the homogeneity degree (integer or fractional) of the observed field, z is the altitude and z_0 is the depth to the source.

Using standard differentiation calculus of logarithmic functions, we may use an equivalent formula for the scaling function $\frac{\partial \log g}{\partial \log z}$ in equation 2.4 and rewrite τ as follows:

$$\tau(z) = \frac{\partial \log g}{\partial \log z} = \frac{1}{g}\frac{\partial g}{\partial z}z \tag{2.5}$$

So, considering the Rasmussen and Pedersen's gravity formula (eq. 3.7), the theoretical scaling function, called τ_T, will be completely defined by computing the expression of $\frac{\partial g}{\partial z}$ (eq. 3.8). Similar computation may be made for computing the scaling function of order p, as follows:

$$\tau_p = \frac{\partial \log g_p}{\partial \log z} = \frac{1}{F_p}\frac{\partial g_p}{\partial z}z \tag{2.6}$$

Formulas for $p = 1$ and $p = 2$ are described in paragraph 3.1 and in Appendix A respectively. Let us assume a source approximated by a polygonal (Talwani's formula).

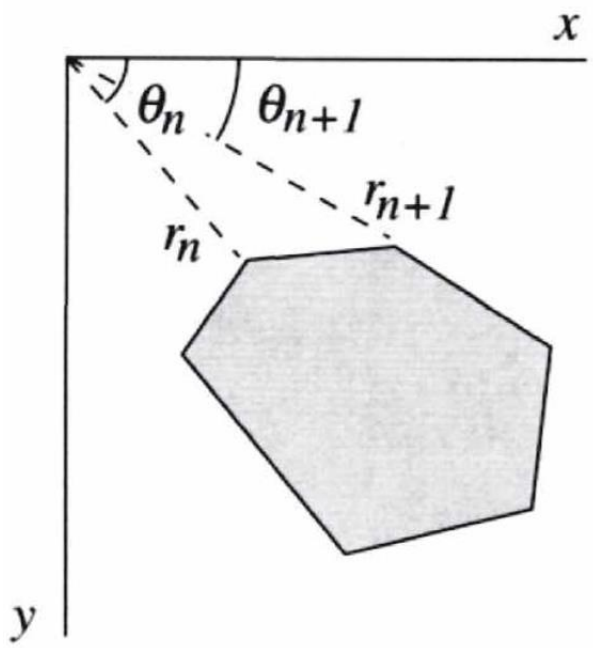

Figure 2.3 – Representation of a polygonal source (modified from Blakely, 1996)

In this case the unknowns are the source-density and the vertex coordinates for the gravity problem, and the only set of vertex coordinates for the scaling function problem. In order to estimate the unknown quantities of the scaling function, i.e., the coordinates $(x_1 \ldots\ldots x_q, z_1 \ldots\ldots z_q)$ of the Q vertices of the body, we will so form the following system of non-linear equation along the ridges (see paragraph 2.3):

$$\begin{bmatrix} \tau_T(\bar{x}_1, \bar{y}_1, \bar{z}_1, x_1, .., x_q, z_1, .., z_q) = \tau(\bar{x}_1, \bar{z}_1) \\ \ldots \qquad\qquad \ldots \\ \tau_T(\bar{x}_i, \bar{y}_i, \bar{z}_i, x_1, .., x_q, z_1, .., z_q) = \tau(\bar{x}_i, \bar{z}_i) \\ \ldots \qquad\qquad \ldots \\ \tau_T(\bar{x}_L, \bar{y}_L \bar{z}_L, x_1, .., x_q, z_1, .., z_q) = \tau(\bar{x}_L, \bar{z}_L) \end{bmatrix} \tag{2.7}$$

where: $\tau(\bar{x}_i, \bar{z}_i)_{\ i=1,\ldots,L}$ refers to the scaling function estimated at points of coordinates $(\bar{x}_i, \bar{z}_i)_{\ i=1,\ldots,L}$ along the ridge and τ_T refers to the theoretical expression computed thanks to equation (2.6) and to the related equations (3.1) (3.2) (3.3) (3.5) (3.7) (3.8) (3.9) (3.12). For instance, to calculate the scaling function of order $p = 2$, we have to calculate the second-order and third-order derivatives of the gravity field for the 2.5D and 2.x D cases.

2.3. Multiridge Analysis

The scaling function is calculated along ridges, the ridges are lines passing through the maxima of a field and of its derivatives at different scales. The multiridge analysis (Fedi et al., 2009) is a multiscale method that is used when the field and its derivatives can be expressed by harmonic functions. This method mainly consists of:

- the creation of a multiscale dataset by performing upward continuation (Blakely, 1996) from the original measurement level to different levels
- individuation and representation of the edges
- representation and continuation of the ridges down to the source-region, to individuate the correct position of the source at the intersection of more ridges.

According to Fedi et al., 2009 there are three types of ridges:

- Zeros of the horizontal derivative
- Zeros of the vertical derivative
- Zeros of the field itself

The intersection of the ridges usually occurs in the source region at the source position (i.e. at the depth to the centre of a sphere or at the depth to the top of an infinite vertical cylinder). The number of ridges depends on the order of the partial derivatives of the field, it increases according to the order of the field.

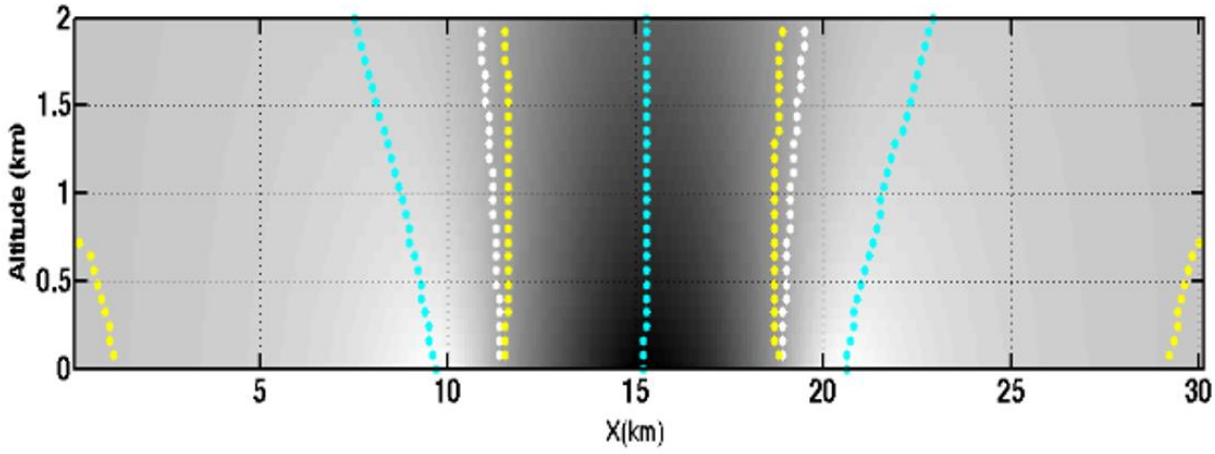

Figure 2.4 – Multiridge Analysis calculated for the first-order vertical derivative of gravity field for a polygonal source. The dotted cyan lines represent the zeros of horizontal derivative, the dotted yellow lines represent the zeros of vertical derivative and the dotted white lines represent the zeros of the field itself.

2.4 Theory of MHODE

The MHODE (Multi-HOmogeneity Depth Estimation) method (Fedi et al., 2015) is the inversion of inhomogeneous fields at different altitudes.

Concerning homogeneous fields, there are many automatic methods to interpret the potential fields: those based on the Euler deconvolution (e.g., Thompson, 1982; Reid et al., 1990; Ravat, 1996; Fedi et al., 2009); the local wavenumber (e.g., Thurston and Smith, 1997; Smith et al., 1998), the Continuous Wavelet Transform (CWT) (e.g., Moreau et al., 1997; Fedi et al., 2010; Fedi and Cascone, 2011), the Depth from Extreme Point (DEXP) (Fedi, 2007; Fedi and Pilkington, 2012; Fedi and Florio, 2013; Abbas et al., 2014; Abbas & Fedi, 2014; Baniamerian et al., 2016) and the Multi-ridge Method (Fedi et al., 2009; Florio and Fedi, 2014).

Homogeneous potential fields f satisfy the homogeneity law:

$$f(tx, ty, tz) = t^n f(x, y, z) \tag{2.8}$$

or, equivalently, the Euler's differential homogeneity equation:

$$\frac{\partial f}{\partial x}(x - x_0) + \frac{\partial f}{\partial y}(y - y_0) + \frac{\partial f}{\partial z}(z - z_0) = -nf \tag{2.9}$$

where n is the homogeneity degree, $t > 0$ and $\{x_0 y_0 z_0\}$ are the coordinates of the unknown single source.

When the potential field f is generated by one-point sources (the source distribution of such sources may be defined by a single point) *n* is integer. The best example is the homogeneously dense sphere (*n*=2) whose field is equivalent to that of a point-mass having its mass distribution concentrated on its centre, so that the gravity field may be defined by this single point (Fedi, 2016).

The homogeneity degree n, for one-point sources, assumes the integer values $\{-3, -2, -1, 0\}$. All the methods for interpreting homogeneous fields assume the homogeneity degree as an integer value at least within a local set of data points.

However, Fedi et al. (2015) argued that any inhomogeneous field can be homogeneous in two asymptotical conditions, either, *a)* measurements are very near to the source region, so horizontal extension can be approximated to infinite, or *b)* measurements are very far from source

region, so any types of sources behave like a point source and the homogeneity degree tends to -3 in magnetic case or -2 in gravity case. But we know that in the real world the causative sources are complex sources and measured fields are no longer homogeneous. Also, we know that the homogeneity degree *n* is a function of distance for a complex source, and that it may hold fractional values as well (Steenland 1968). This is confirmed by other authors, dealing with sources which are not one-point sources and whose homogeneity degree *n* is fractional: in that case, the retrieved depth is somewhere between the source top and centre (Keating and Pilkington, 2004; Gerovska et al., 2005). On the other hand, Fedi et al. (2015) generalized the homogeneity law, similar to multifractal scaling laws from monofractals and redefined Equation 2.8 in the following manner:

$$f(ax, ay, az) = a^{n(x,y,z)} f(x, y, z) \tag{2.10}$$

so Euler differential becomes:

$$\frac{\partial f}{\partial x}(x - x_0) + \frac{\partial f}{\partial y}(y - y_0) + \frac{\partial f}{\partial z}(z - z_0) = \\ = -n(x, y, z) f(x, y, z) \tag{2.11}$$

where *n* is now a function of distance to the source and f is an inhomogeneous field.

In contrast to ideal sources, real sources are finite and not necessarily equivalent to sources concentrated at a single point. So, real sources are expected to generate, as a general behaviour, inhomogeneous fields. For these fields the local homogeneity-degree may be computed by current methods revealing to be a function $n(r)$ varying versus the distance to the source (see fig. 2 in Steenland 1968), with their values being either fractional or integer, as well (Fedi et al., 2015). In general, these sources are finite in all extent and we may also refer to them as multiple or multipoint sources. Fedi et al., (2015) have shown that any type of field homogenous or inhomogeneous may have integer or fractional values of the homogeneity degree and that it changes with respect to distance from the source. For many sources (Fedi et al., 2015; Ravat, 1994; Steenland, 1968), the field homogeneity-degree *n*, is varying from 0 to -2 with respect to the depth to the top of the source. So, in the case of a single-scale study, the homogeneity degree may occasionally assume an integer value but in reality, it is continuously tending from 0 to a higher fractional value at higher distance. Therefore, to study the field of realistic sources, real and varying values of the homogeneity degree should are expected along the whole multiscale dataset.

Fedi et al. (2015) defined the local homogeneity by distinguishing homogenous and locally homogeneous functions. Consider $f(\mathbf{r})$ is a continuously differentiable in the region R, then it is locally homogeneous of degree n, if and only if:

$$\nabla f(\mathbf{r})(\mathbf{r}-\mathbf{r_0}) = -nf(\mathbf{r}) \tag{2.12}$$

From Equation 2.12 it follows that: *a*) $f(\mathbf{r})$ is locally homogeneous of degree n in a region R if and only if f it is homogeneous of degree n in some neighbourhood of every point of R; and *b)* locally homogeneous fields are not necessarily homogeneous, since *n* may change in subregions of R, as exemplified with a counterexample by Gelbaum & Olmsted (2003); conversely, homogeneous fields are always locally homogeneous. Since the homogeneity degree is different in different domains of the space, Fedi et al. (2015) introduced a new expression for such potential fields, called *multi-homogeneous field*.

Therefore, following the concept of multi-homogeneity, any function can be approximated as:

$$f(\mathbf{r}) \sim F_H(\mathbf{r}) \tag{2.13}$$

where $F_H(\mathbf{r})$ is the best homogeneous field of degree n in the considered window *W* (Fedi et al., 2009; Fedi et al., 2015; Florio and Fedi, 2014).

The main assumption of this method is therefore that at any altitude the inhomogeneous field could be approximated by a homogeneous field, with fractional or integer degree.

Inhomogeneous fields may be studied by classical methods, such as Euler Deconvolution, provided they are analysed at different altitudes. In this work we will instead not process directly the gravity data, but a correlated quantity, the scaling function, which we described in section 2.2. One of the main advantages of the scaling function is that it does not depend on density or other physics constants, but only on the geometric characteristics of the source. MHODE (Multi-HOmogeneity Depth Estimation) is a new technique of source parameter estimation, permitting retrieval of the source parameters of complex sources (Fedi et al., 2015). Fedi et al. (2015) examined in detail the application of a multi-homogeneous model to inhomogeneous fields and showed that the whole multiscale behaviour of $n(r)$ and of $z_0(r)$ is needed to study potential fields and to

improve substantially their interpretation. We show in figure 2.3 the curves of $z_0(z)$ and $n(z)$ computed for the inhomogeneous field due to a finite cylinder.

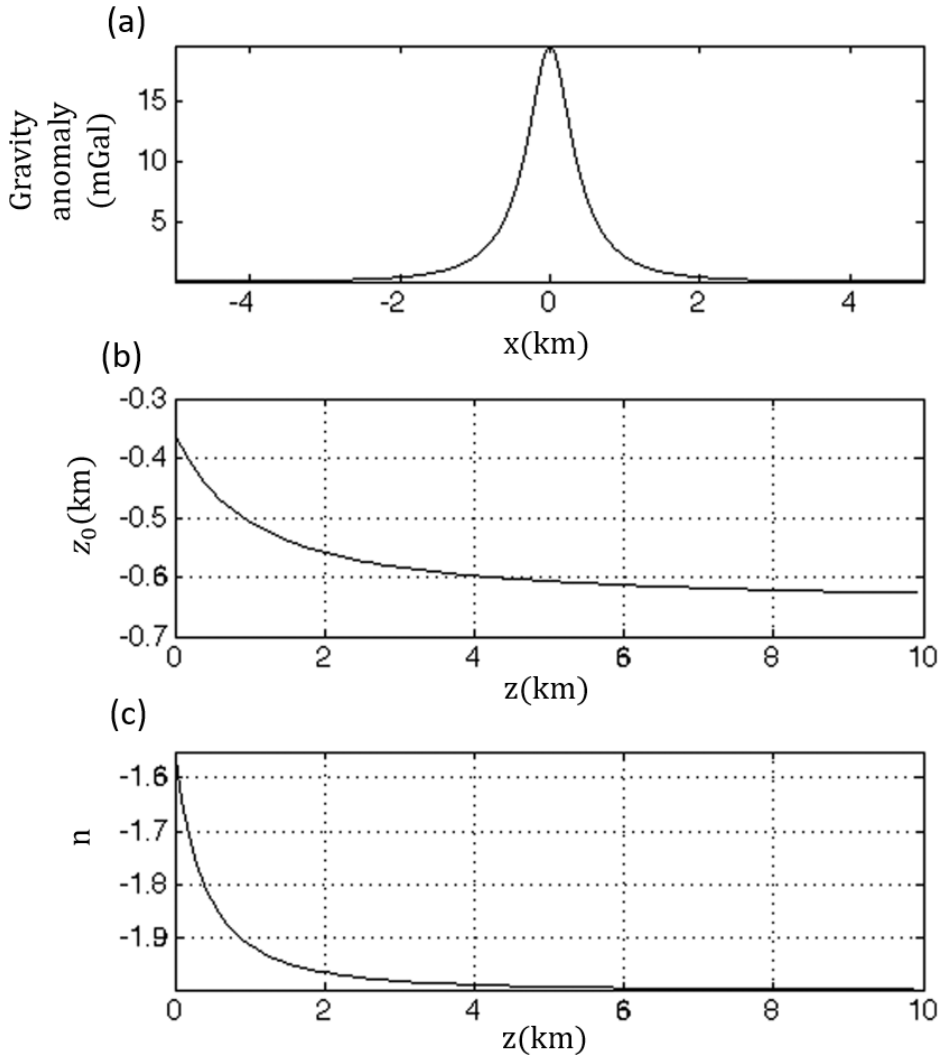

Figure 2.3 - Multiscale Euler deconvolution of the gravity field of a cylindrical model. The model is a vertical cylinder having z_{01} = 300 m, z_{02} = 1 km, a 100 m radius and a 2 g cm^{-3} density. The analysed data are along a ridge of type I of the gravity field shown in (a); (b) depth to source estimates versus the altitude, $z_0(z)$; (c) homogeneity degree estimates versus the altitude, n(z). As expected, $z_0(z)$ and n(z) are both not constant functions of the altitude indicating that the field is inhomogeneous (modified from Fedi et al., 2015).

The theoretical expression of the scaling function for an inhomogeneous field is:

$$\tau_T = n(z)\frac{z}{z - z_0(z)} \tag{2.14}$$

Fedi et al. (2015) formed the system:

$$\begin{bmatrix} -z_1 \dfrac{2z_1 - z_{01} - z_{02}}{(z_1 - z_{01})(z_1 - z_{02})} = -n(z_1) \dfrac{z_1}{z_1 - z_0(z_1)} \\ \cdot \quad \cdot \quad \cdot \\ \cdot \quad \cdot \quad \cdot \\ \cdot \quad \cdot \quad \cdot \\ z_M \dfrac{2z_M - z_{01} - z_{02}}{(z_M - z_{01})(z_M - z_{02})} = -n(z_M) \dfrac{z_M}{z_M - z_0(z_1)} \end{bmatrix} \tag{2.15}$$

$$i = 1, \dots, M.$$

where the scaling function refers to M altitudes and the first members of the M equations refer to the theoretical expression of the scaling function of the first order derivative of a finite vertical cylinder. The unknowns are z_{01} and z_{02}, i.e. the depths to the top and to the bottom of the cylinder. Using an optimization code based on the Levenberg–Marquardt algorithm, they got the true solution for a synthetic case very quickly.

CHAPTER 3. FORWARD PROBLEM FOR THE SCALING FUNCTION OF THE GRAVITY FIELD AND OF ITS DERIVATIVES

As we have seen, in order to form the equation system (2.7), we need to compute the scaling function at different altitudes along the ridges and we have also to compute the theoretical forward problems for the scaling function. In the case illustrated above, the theoretical formula of a finite cylinder was obviously known, and the unknown quantities were just the depths to the top and to the bottom of the finite cylinder. In the case of a general source we need to define the forward problem for the gravity field and its derivatives in the 2.5D, 2.x D cases for a general polygon of unknown vertex coordinates and for a general polyhedron in the 3D case. However, being this case very complex, in this project we will merely consider the 2.x D formulae for a general source, which is indeed a substantial task developed in this research project, and we will use the 3D formulae to create a synthetic gravity map to extract the profiles that represent the observed data in the synthetic case. Once these formulas are fixed, we can use equations 2.5 and 2.6 to have the theoretical equations of the scaling function for the gravity field and its derivatives in the 2.5D, 2.x D approximation.

3.1 2.5D and 2.x D formulae for the gravity forward problem

The 2.x D forward problem has several advantages vs. the 2D case. First of all, it allows us to consider the strike length of the body source like a finite length. Besides, we can manage the symmetry of the profile with respect to the source in a correct way.

To obtain this type of forward problem is often enough to treat three-dimensional problems by introducing end corrections to allow the finite extent of the causative bodies. The important feature about these corrections is that they can really be considered as corrections to the simple 2D expressions, therefore calculating the fields from such bodies becomes quite rapid (Figure 3.1).

The 2.5D and 2.x D modelling is obtained starting from the well-known 2-D formulae of Talwani and Heirtzler (1964), slightly changed to represent the body with a geometry “two-and-a-half-dimensional”, or 2.5D by the Shuey and Pasquale (1973) formulae:

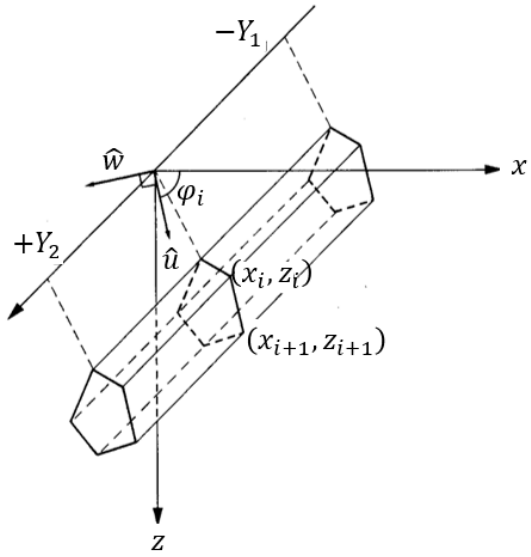

Figure 3.1 – Representation of a body in 2.5 dimension. Y is the strike length, for Y1 = Y2 we have a symmetrical body and for Y1≠Y2 we have an asymmetrical body (modified from Rasmussen & Pedersen, 1979).

To calculate the gravity field expressed by a source in 2.5 dimension we use the equation 8 from the Rasmussen & Pedersen (1979) paper:

$$g_z = -2YG\rho \sum_i -\cos\varphi_i \log\frac{u_{i+1}+R_{i+1}}{u_i+R_i} + \\ +2G\rho \sum_i \frac{x_i z_{i+1} - z_i x_{i+1}}{\Delta x_i{}^2 + \Delta z_i{}^2} \left\{ \begin{array}{c} \Delta z_i \log\frac{r_{i+1}(Y+R_i)}{r_i(Y+R_{i+1})} + \\ +\Delta x_i \left(tan^{-1}\frac{u_{i+1}Y}{w_i R_{i+1}} - tan^{-1}\frac{u_i Y}{w_i R_i} \right) \end{array} \right\} \quad (3.1)$$

Where: G is the gravitational constant, ρ is the density of the body, Y is the strike length, $\Delta x_i = x_{i+1} - x_i$; $\Delta z_i = z_{i+1} - z_i$; $R_{i+1} = (u_{i+1}^2 + w_i^2 + Y^2)^{1/2}$; $R_i = (u_i^2 + w_i^2 + Y^2)^{1/2}$; $r_{i+1} = (u_{i+1}^2 + w_i^2)^{1/2}$; $r_i = (u_i^2 + w_i^2)^{1/2}$; $w_i = w_{i+1} = -\sin\varphi_i x_i + \cos\varphi_i z_i$; $u_i = \cos\varphi_i x_i + \sin\varphi_i z_i$; $u_{i+1} = \cos\varphi_i x_{i+1} + \sin\varphi_i z_{i+1}$.

The first-order vertical derivative of gravity field is represented by the equation 16 in the Rasmussen & Pedersen (1979):

$$\frac{\partial g_z}{\partial z} = -2G\rho \sum_i \frac{\Delta x_i}{{\Delta x_i}^2 + {\Delta z_i}^2} \left\{ \Delta z_i \log \frac{r_i(R_{i+1} + Y)}{r_{i+1}(R_i + Y)} - \right.$$
$$\left. - \Delta x_i \left(tan^{-1} \frac{u_{i+1} Y}{w_i R_{i+1}} - tan^{-1} \frac{u_i Y}{w_i R_i} \right) \right\} \tag{3.2}$$

where:

$R_{i+1} = (u_{i+1}^2 + w_i^2 + Y^2)^{1/2}$; $r_{i+1} = (u_{i+1}^2 + w_i^2)^{1/2}$;

$R_i = (u_i^2 + w_i^2 + Y^2)^{1/2}$; $r_i = (u_i^2 + w_i^2)^{1/2}$;

$w_i = w_{i+1} = -\sin \varphi_i x_i + \cos \varphi_i z_i$;

$u_i = \cos \varphi_i x_i + \sin \varphi_i z_i$; $u_{i+1} = \cos \varphi_i x_{i+1} + \sin \varphi_i z_{i+1}$;

During my period abroad, in collaboration with the Aristotle University of Thessaloniki, we developed the formulae for the second-order and third-order vertical derivative of gravity. Using equation (3.3) we calculated the second-order vertical derivative of gravity field

$$\frac{\partial^2 g_z}{\partial {z^2}} = -2G\rho \sum_i \frac{\Delta_{x_i}}{\Delta_{x_i^2} + \Delta_{z_i^2}} \frac{\partial D}{\partial z} \tag{3.3}$$

where:

$$D = \Delta z_i \, log \frac{r_i(R_{i+1} + Y)}{r_{i+1}(R_i + Y)} - \Delta x_i \left(tan^{-1} \frac{u_{i+1} Y}{w_i R_{i+1}} - tan^{-1} \frac{u_i Y}{w_i R_i} \right) \tag{3.4}$$

See equations A.1, A.2 and A.7 for the complete mathematical definition of $\frac{\partial^2 g_z}{\partial z^2}$. for all development of the second-order vertical derivative of the field for the symmetrical case see the Appendix A.1.

The third-order vertical derivative of gravity field is given by:

$$\frac{\partial^3 g_z}{\partial z^3} = -2G\rho \sum_i \frac{\Delta_{x_i}}{\Delta_{x_i^2} + \Delta_{z_i^2}} \frac{\partial^2 D}{\partial z^2} \tag{3.5}$$

where:

$$D = \Delta z_i \frac{\partial C_1}{\partial z} - \Delta x_i \left(\frac{\partial C_2}{\partial z} - \frac{\partial C_3}{\partial z} \right) \tag{3.6}$$

See equations A.30 and A.31 for the complete mathematical definition of $\frac{\partial^3 g_z}{\partial z^3}$ for all development of the third-order vertical derivative of the field for the symmetrical case see the Appendix A.3.

While for the asymmetrical case 2.x D the formula to calculate the gravity field:

$$\begin{aligned} g_z = & -Y_2 G\rho \sum_i \hat{\mathbf{z}} \cdot \hat{\mathbf{n}}_\mathbf{i} \log \frac{u_{i+1} + R_{i+1}}{u_i + R_i} \\ & + G\rho \sum_i \frac{x_i z_{i+1} - z_i x_{i+1}}{{\Delta x_i}^2 + {\Delta z_i}^2} \begin{Bmatrix} \Delta z_i \log \dfrac{r_{i+1}(Y_2 + R_i)}{r_i(Y_2 + R_{i+1})} + \\ + \Delta x_i \left(tan^{-1} \dfrac{u_{i+1} Y_2}{w_i R_{i+1}} - tan^{-1} \dfrac{u_i Y_2}{w_i R_i} \right) \end{Bmatrix} + \\ & + Y_1 G\rho \sum_i \hat{\mathbf{z}} \cdot \hat{\mathbf{n}}_\mathbf{i} \log \frac{u_{i+1} + R_{i+1}}{u_i + R_i} + \\ & + G\rho \sum_i \frac{x_i z_{i+1} - z_i x_{i+1}}{{\Delta x_i}^2 + {\Delta z_i}^2} \begin{Bmatrix} \Delta z_i \log \dfrac{r_{i+1}(Y_1 + R_i)}{r_i(Y_1 + R_{i+1})} + \\ + \Delta x_i \left(tan^{-1} \dfrac{u_{i+1} Y_1}{w_i R_{i+1}} - tan^{-1} \dfrac{u_i Y_1}{w_i R_i} \right) \end{Bmatrix} \end{aligned} \tag{3.7}$$

And, for the first-order vertical derivative of gravity field, we have:

$$\begin{aligned} \frac{\partial g_z}{\partial z} = & -G\rho \sum_i \frac{\Delta x_i}{{\Delta x_i}^2 + {\Delta z_i}^2} \left\{ \Delta z_i \log \frac{r_i(R_{i+1} + Y_2)}{r_{i+1}(R_i + Y_2)} - \Delta x_i \left(tan^{-1} \frac{u_{i+1} Y_2}{w_i R_{i+1}} - tan^{-1} \frac{u_i Y_2}{w_i R_i} \right) \right\} + \\ & + G\rho \sum_i \frac{\Delta x_i}{{\Delta x_i}^2 + {\Delta z_i}^2} \left\{ \Delta z_i \log \frac{r_i(R_{i+1} + Y_1)}{r_{i+1}(R_i + Y_1)} \right. \\ & \left. - \Delta x_i \left(tan^{-1} \frac{u_{i+1} Y_1}{w_i R_{i+1}} - tan^{-1} \frac{u_i Y_1}{w_i R_i} \right) \right\} \end{aligned} \tag{3.8}$$

From the equation 3.8 we have calculated the second order of vertical derivative of gravity field:

$$\frac{\partial^2 g_z}{\partial z^2} = -G\rho\left\{\sum_i \frac{\Delta_{x_i}}{\Delta_{x_i^2}+\Delta_{z_i^2}}\frac{\partial D_2}{\partial z} + \sum_i \frac{\Delta_{x_i}}{\Delta_{x_i^2}+\Delta_{z_i^2}}\frac{\partial D_1}{\partial z}\right\} \tag{3.9}$$

where D_2 and D_1 factors are:

$$D_2 = \Delta z_i \, log\frac{r_i(R_{i+1}+Y_2)}{r_{i+1}(R_i+Y_2)} - \Delta x_i\left(tan^{-1}\frac{u_{i+1}Y_2}{w_i R_{i+1}} - tan^{-1}\frac{u_i Y_2}{w_i R_i}\right) \tag{3.10}$$

$$D_1 = \Delta z_i \, log\frac{r_i(R_{i+1}+Y_1)}{r_{i+1}(R_i+Y_1)} - \Delta x_i\left(tan^{-1}\frac{u_{i+1}Y_1}{w_i R_{i+1}} - tan^{-1}\frac{u_i Y_1}{w_i R_i}\right) \tag{3.11}$$

See equations A.11 A.12 A.17 A.21 and A.26 for the complete mathematical definition of $\frac{\partial^2 g_z}{\partial z^2}$ for all development of the third-order vertical derivative of the field for the asymmetrical case see the Appendix A.2.

The third-order vertical derivative of the gravity field for the asymmetrical case:

$$\frac{\partial^3 g_z}{\partial z^3} = -G\rho\left\{\sum_i \frac{\Delta_{x_i}}{\Delta_{x_i^2}+\Delta_{z_i^2}}\frac{\partial^2 D_2}{\partial z^2} + \sum_i \frac{\Delta_{x_i}}{\Delta_{x_i^2}+\Delta_{z_i^2}}\frac{\partial^2 D_1}{\partial z^2}\right\} \tag{3.12}$$

where D_2 and D_1 factors are:

$$D_2 = \Delta z_i \frac{\partial C_1}{\partial z} - \Delta x_i\left(\frac{\partial C_2}{\partial z} - \frac{\partial C_3}{\partial z}\right) \tag{3.13}$$

$$D_1 = \Delta z_i \frac{\partial C_1}{\partial z} - \Delta x_i \left(\frac{\partial C_2}{\partial z} - \frac{\partial C_3}{\partial z} \right) \tag{3.14}$$

See equations A.47 A.48 and A.64 for the complete mathematical definition of $\frac{\partial^3 g_z}{\partial z^3}$ for all development of the third-order vertical derivative of the field for the asymmetrical case see the Appendix A.4.

3.2 2.5D and 2.x D formulae for the magnetic forward problem

In collaboration with the Aristotle University of Thessaloniki, we also developed the formulae for symmetrical 2.5D and asymmetrical 2.x D cases for the magnetic field. From the work of Rasmussen & Pedersen (1979) we have the formula to calculate the vertical component B_z of magnetic field in a symmetrical case:

$$B_z = -2J \sum_i \frac{\Delta x_i}{{\Delta x_i}^2 + {\Delta z_i}^2} \left\{ (j_x \Delta x_i + j_z \Delta z_i) \log \frac{r_i (R_{i+1} + Y)}{r_{i+1}(R_i + Y)} + \right. \\ \left. + (j_x \Delta z_i - j_z \Delta x_i) \left(tan^{-1} \frac{u_{i+1} Y}{w_i R_{i+1}} - tan^{-1} \frac{u_i Y}{w_i R_i} \right) \right\} \tag{3.15}$$

where, J is the magnetization of the body and j_x, j_y, and j_z are the magnetization directions.

From the equation (3.15) we calculated the first-order vertical derivative of the vertical component of magnetic field:

$$\frac{\partial B_z}{\partial z} = -2J \sum_i \frac{\Delta z_i}{\Delta x_i^2 + \Delta z_i^2} \frac{\partial D}{\partial z} \tag{3.16}$$

where:

$$D = (j_x \Delta x_i + j_z \Delta z_i) \, log \frac{r_i (R_{i+1} + Y)}{r_{i+1}(R_i + Y)} - (j_x \Delta z_i - j_z \Delta x_i) \left(tan^{-1} \frac{u_{i+1} Y}{\omega_i R_{i+1}} - tan^{-1} \frac{u_i Y}{\omega_i R_i} \right) \tag{3.17}$$

See equations A.80 A.81 and A.86 for the complete mathematical definition of $\frac{\partial B_z}{\partial z}$ for all development of the first-order vertical derivative of the vertical component of magnetic field for the symmetrical case see the Appendix A.5.

The second-order vertical derivative of the vertical component of magnetic field is represented by the equation:

$$\frac{\partial^2 B_z}{\partial z^2} = -2CmJ \sum_i \frac{\Delta_{x_i}}{\Delta_{x_i^2} + \Delta_{z_i^2}} \frac{\partial D}{\partial z} \tag{3.18}$$

where:

$$D = (j_x \Delta x_i + j_z \Delta z_i) \frac{\partial C_1}{\partial z} + (j_x \Delta z_i - j_z \Delta x_i) \left(\frac{\partial C_2}{\partial z} - \frac{\partial C_3}{\partial z} \right) \tag{3.19}$$

See equations A.125 and A.126 for the complete mathematical definition of $\frac{\partial^2 B_z}{\partial z^2}$ for all development of the first-order vertical derivative of the vertical component of magnetic field for the symmetrical case see the Appendix A.7.

For the asymmetrical case we have the formula to calculate the vertical component B_z of magnetic field:

$$
\begin{aligned}
B_z = & \\
& -J\left\{\sum_i \frac{\Delta x_i}{{\Delta x_i}^2+{\Delta z_i}^2}\left[(j_x\Delta x_i + j_z\Delta z_i)\, log\,\frac{r_i(R''_{i+1}+Y_2)}{r_{i+1}(R''_i+Y_2)}\right.\right. \\
& + (j_x\Delta z_i - j_z\Delta x_i)\left(tan^{-1}\frac{u_{i+1}Y_2}{\omega_i R''_{i+1}} - tan^{-1}\frac{u_i Y_2}{\omega_i R''_i}\right) \\
& \left. + j_y\left(\frac{1}{2}log\,\frac{(R''_{i+1}-u_{i+1})(r_{i+1}+u_{i+1})}{(R''_{i+1}+u_{i+1})(r_{i+1}-u_{i+1})} - \frac{1}{2}log\,\frac{(R''_i-u_i)(r_i+u_i)}{(R''_i+u_i)(r_i-u_i)}\right)\right] \\
& + \sum_i \frac{\Delta x_i}{{\Delta x_i}^2+{\Delta z_i}^2}\left[(j_x\Delta x_i + j_z\Delta z_i)\, log\,\frac{r_i\left(R'_{i+1}+(-Y_1)\right)}{r_{i+1}\left(R'_i+(-Y_1)\right)}\right. \\
& + (j_x\Delta z_i - j_z\Delta x_i)\left(tan^{-1}\frac{u_{i+1}(-Y_1)}{\omega_i R'_{i+1}} - tan^{-1}\frac{u_i(-Y_1)}{\omega_i R'_i}\right) \\
& \left.\left. + j_y\left(-\frac{1}{2}\log\frac{(R'_{i+1}-u_{i+1})(r_{i+1}+u_{i+1})}{(R'_{i+1}+u_{i+1})(r_{i+1}-u_{i+1})} + \frac{1}{2}\log\frac{(R'_i-u_i)(r_{i+1}+u_i)}{(R'_i+u_i)(r_{i+1}-u_i)}\right)\right]\right\}
\end{aligned}
\tag{3.20}
$$

where $R''_i = (u_i^2 + w_i^2 + Y_2^2)^{1/2}$; $R''_{i+1} = (u_{i+1}^2 + w_i^2 + Y_2^2)^{1/2}$;

$R'_i = (u_i^2 + w_i^2 + (-Y_1)^2)^{1/2}$; $R'_{i+1} = (u_{i+1}^2 + w_i^2 + (-Y_1)^2)^{1/2}$;

The formula to calculate the first-order vertical derivative of vertical component of magnetic field is:

$$
\frac{\partial B_z}{\partial z} = -CmJ\sum_i \frac{\Delta_{x_i}}{\Delta_{x_i^2}+\Delta_{z_i^2}}\left[\frac{\partial D_2}{\partial z} - \frac{\partial D_1}{\partial z}\right] \tag{3.21}
$$

where D_2 and D_1 factors are:

$$
D_2 = (j_x\Delta x_i + j_z\Delta z_i)C_1 + (j_x\Delta z_i - j_z\Delta x_i)(C_2 - C_3) + j_y\left(-\frac{1}{2}C_4 + \frac{1}{2}C_5\right) \tag{3.22}
$$

$$
D_1 = (j_x\Delta x_i + j_z\Delta z_i)C_1 + (j_x\Delta z_i - j_z\Delta x_i)(C_2 - C_3) + j_y\left(-\frac{1}{2}C_4 + \frac{1}{2}C_5\right) \tag{3.14}
$$

See equations A.90 A.91 A.98 A.108 and A.115 for the complete mathematical definition of $\frac{\partial B_Z}{\partial z}$ for all development of the first-order vertical derivative of the vertical component of magnetic field for the asymmetrical case see the Appendix A.6.

Finally, we wrote these formulae in a Matlab code, implementing them in MHODE inversion algorithm.

3.3 3D forward problem

Among the different works about 3D forward problem (Fueg & Xia, 1996; Gotze & Lameyer, 1988; Hansen, 1999; Holstein & Ketteridge, 1996; Holstein et al., 2007; Moraes & Hansen, 2001; Pohanka, 1988; Richardson & MacInnes, 1989; Talwani & Ewing, 1960; Tsoulis, 2012; Wu & Hu, 2006), we chose the one about the calculus of a polyhedral source gravity field.

The 3D forward problem by *polyhedron code* (Tsoulis, 2012) consists in calculating the gravitational potential, the field and the its first-order derivative of a 3D source model, defined by polyhedral faces which are built by closed polygons S_P along these calculates line integrals. The advantage of this algorithm is the possibility to create sources with general shapes, since it is a flexible model tool.

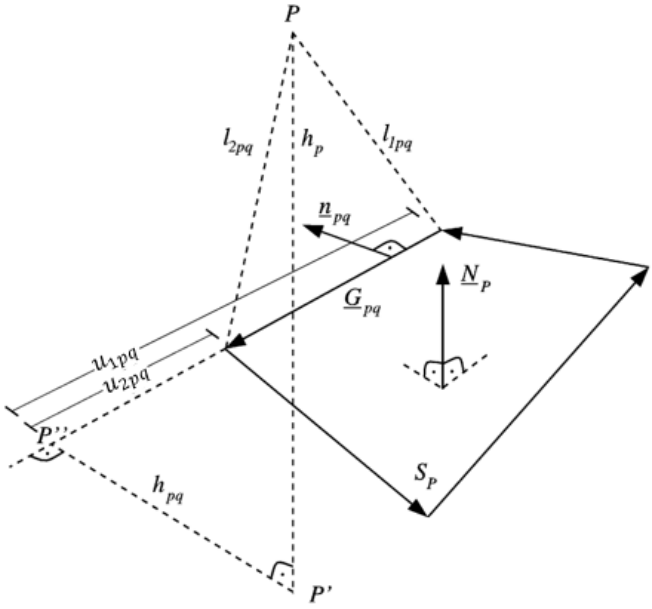

Figure 3.2 – Geometrical definitions of the quantities used in the evaluation procedure for an individual face of the polyhedron (modified from Tsoulis & Petrovic, 2001).

In figure 3.2 P' is the projection of the computation point P, P'' is the orthogonal projection of P' on the straight line of the line segment G_{pq}, line segments that form the plane of polygon S_p, while S_{pq} are the distances between $P''$and the end points of G_{pq}.

Even if we have not intention to develop the 3D MHODE modelling for polyhedron-like sources during this project, we are, however, interested in these formulae in order to generate anomalies from realistic sources. We will then interpret these anomalies by 2.x D models and will try to use them for building a 3D model with the VOXI algorithm.

To this end we have two formulae that we are interested in, the formula of gravitational field and the formula of first-order vertical derivative:

$$V_{x_i} = G\rho \sum_{p=1}^{n} cos(\mathbf{N}_\mathrm{p}, \mathbf{e}_\mathrm{i}) \left[\sum_{q=1}^{m} \sigma_{pq} h_{pq} LN_{pq} + h_p \sum_{q=1}^{m} \sigma_{pq} AN_{pq} + SING_{\mathcal{A}_p} \right] \qquad (3.13)$$

$$(i = 1,\ 2,\ 3)$$

$$V_{x_i x_j} = G\rho \sum_{p=1}^{n} cos(\mathbf{N}_\mathrm{p}, \mathbf{e}_\mathrm{i}) \left[\sum_{q=1}^{m} cos(\mathbf{n}_\mathrm{pq}, \mathbf{e}_\mathrm{j})\, LN_{pq} + \sigma_p\, cos(\mathbf{N}_\mathrm{p}, \mathbf{e}_\mathrm{j}) \sum_{q=1}^{m} \sigma_{pq} AN_{pq} + SING_{B_{pj}} \right] \qquad (3.14)$$

$$(i, j = 1,\ 2,\ 3)$$

where $\mathbf{N}_p$ is the outer unit normal of the polyhedral plane p, $\mathbf{n}_{pq}$ the normal of segment q that lies on the plane of polygon S_p, h_p is the positive distance between the plane p and the computation point P, σ_p variable indicates the sign of h_p, h_{pq} distance between P' and P'' and σ_p variable indicates the sign of h_{pq}.

The terms $SING_{\mathcal{A}_p}$and $SING_{B_{pj}}$ are parameters of control on the positions of the projections of the calculation point P, so they depend on the location of P', if P' is located out of polygonS_p $SING_{\mathcal{A}_p} = SING_{B_{pj}} = 0$ (Tsoulis and Petrovic, 2001).

Finally, we have two quantities LN_{pq} and AN_{pq} that are abbreviations of the following transcendental expressions:

$$LN_{pq} = \ln \frac{u_{2pq} + l_{2pq}}{u_{1pq} + l_{1pq}}; \qquad AN_{pq} = arctan \frac{h_p u_{2pq}}{h_{pq} l_{2pq}} - arctan \frac{h_p u_{1pq}}{h_{pq} l_{1pq}};$$

here, we have $l_{1_{pq}}$ and $l_{2_{pq}}$ that are the distances between P and the end points of G_{pq}, while $u_{1_{pq}}$ and $u_{2_{pq}}$ are the distances between P'' and the end points of G_{pq}.

In each of these formulae we have two summations, one inner for the sum of line segments q, is running from one to m for each face p, and the other one outer for the sum of all faces of polyhedron.

The calculus of the second-order vertical derivative and also of their high-order derivatives for the polyhedral source is very complex, that is why we decided to use MHODE for the 3D case, through different 2.x D sections. The set of the so interpreted sections will then be used as a priori model for the 3D inversion with VOXEL method (Ellis, 2012).

CHAPTER 4. 2.x D MHODE INVERSION

The word *inversion* in geophysics refers to mathematical and statistical techniques for recovering in an automatic way information on the subsurface physical properties from observed geophysical data. If N measurements are performed in a particular experiment, for instance, one might consider these numbers as the elements of a vector $\mathbf{d}$ of length N**.** Similarly, the model parameters can be represented as the elements of a vector $\mathbf{m}$**,** which, is of length M.

$$\begin{aligned} &\text{data:} && \mathbf{d} = [d_1, d_2, d_3, d_4, \dots, d_N]^T \\ &\text{model parameters:} && \mathbf{m} = [m_1, m_2, m_3, m_4, \dots, m_N]^T \end{aligned} \tag{4.1}$$

where ^{T} denotes transpose (Menke, 1989).

In an inverse problem the model parameters and the data are in some way related. This relationship is given by the theory, that is one or more formulas that the data and model parameters are expected to follow.

In more realistic situations the data and model parameters are related in complicated ways, by one or more implicit equations such as

$$\begin{aligned} f_1(\mathbf{d}, \mathbf{m}) &= 0 \\ f_2(\mathbf{d}, \mathbf{m}) &= 0 \\ &\cdot \\ &\cdot \\ &\cdot \\ f_L(\mathbf{d}, \mathbf{m}) &= 0 \end{aligned} \tag{4.2}$$

where L is the number of equations.

When the relationship among $\mathbf{d}$ and $\mathbf{m}$ is linear, we have to solve the system:

$$\mathbf{d} = \mathbf{Am} \tag{4.3}$$

in order to estimate $\mathbf{m}$.

A solution to an inverse problem is not unique. When trying to solve an inverse problem, the error function (misfit) *E* can be defined by a sum of squares of the individual misfit error as:

$$E = \sum_{i=1}^{N} e_i^2 \tag{4.4}$$

This is the squared Euclidean length of the vector $\mathbf{e}^T\mathbf{e}$. The Euclidean length is one of the possible ways to quantifying the size or length of a vector. In general, the norm is used to refer for measuring the length and indicated by a set of double vertical bars: $\|e\|$ is the norm of vector $\mathbf{e}$ (Menke, 1989). A general norm L_p (e.g., Menke, 1989; Dimri, 1992; Sen and Stoffa, 2013) is defined as:

$$L_p\ norm\colon \|e\|_p = \left[\sum_{i=1}^{N} |e_i|^p\right]^{1/p} \tag{4.5}$$

where N is the number of data points. In geophysical application, the $L_2\ norm$ is commonly used, as given by:

$$L_2\ norm\colon \|e\|_2 = \left[\sum_{i=1}^{N} |e_i|^2\right]^{1/2} \tag{4.6}$$

Use of other norms, e.g. L1 can also be found in the geophysical literature. One main requirement is that the found parameters could generate computed data which could well approximate the true data. In this case the misfit error depends on being the problem linear or nonlinear.

Geophysical problems are often non-linear and the error function can have multiple minima of various size. In this case, we must distinguish among local optimization algorithms and global optimization algorithms (Dimri, 1992; Sen and Stoffa, 2013). To find and quantify the error function minimum, we have to kinds of algorithms. On the one hand, local optimization algorithms calculate the gradient of the problem and typically try to find a local minimum in the close neighbourhood of the starting solution. On the other hand, global optimization algorithms try to find the global minimum of the error function. These types of algorithms (Sen and Stoffa, 2013) are stochastic in nature and use global information about the error surface to update their current position. In many cases, global optimization algorithms are still able to find the good solution starting with poor initial models. Global optimization algorithms include genetic algorithm, simulated annealing algorithms and others (Ingber, 1989; Kirkpatrick et al., 1983; Sen & Stoffa, 1995; Sen & Stoffa 2013).

To optimize our inverse problem in the MHODE method we used the Very Fast Simulated Annealing algorithm (VFSA). In the next paragraphs, we will first introduce how to approach an inverse problem with MHODE, then we will examine the VFSA more closely.

4.1 Global optimization algorithm with MHODE

As we said in the previous chapter, with MHODE we can approximate the measured inhomogeneous field at any altitude to a homogeneous field. With MHODE we invert the scaling function, calculated along the ridges at different altitudes, solving a set of non-linear equations. The main objective is to find only the parameters related to the source geometry, as the scaling function does not depend on density but only on the geometrical features of the body (vertex coordinates).

Obtaining *a priori* information, that can be geological, seismic or other geophysical data information, we can approach to the solution of the following problem: the more are the sides of the polygon, the more precise will the gravity field computation, but at the same time this implicates more difficulties in the solution of the inversion problem.

In the case of salt domes, we will see a clear image of a salt dome structure top through the seismic method, but not the rest of the body. For this reason, we will use gravity to investigate the edges and the bottom of the source body, while constraining the top part of the body from seismic information.

We will solve Equation 2.7 by using the Very Fast Simulated Annealing method. As we said before, MHODE method includes the inversion of the scaling function, so we can write the error function as:

$$E = \sum (\tau^T - \tau)^2 \qquad (4.7)$$

where τ^T is the scaling function value computed using the estimated source model and τ is the scaling function calculated along the ridges.

4.2 VFSA (Very Fast Simulated Annealing) algorithm

One of the main aims of the geophysical inversion is searching for a minimum of an error function $E(\mathbf{m})$, where $\mathbf{m}$ is a model vector. Very Fast Simulated Annealing (VFSA) has been chosen as it is a method for finding the global minimum of a function $E(\mathbf{m})$. The basic concepts of VFSA are taken from problems in statistical mechanics that concern the analysis of the properties of several atoms in samples of liquid or solid. It is a modified form of simulated annealing (SA), a global optimization method used in many geophysical parameter estimation problems.

SA is a method for solving unconstrained and bound-constrained optimization problems. The method models the physical process of heating a material and then slowly lowering the temperature to decrease defects, thus minimizing the system energy. In particular, it is used for finding the global minimum of a function $E(\mathbf{m})$. Many geophysical inverse problems also involve finding the minimum of an error function $E(\mathbf{m})$ and, as a consequence, SA has been applied on these problems.

VFSA has recently is even more efficient from a computational point of view. In contrast to SA, in VFSA the perturbations are generated from the model parameters according to a Cauchy-like distribution whose shape changes with each iteration. This results in an algorithm that converges much faster than a SA. In finding the optimal solution, VFSA tries several models from the search space. All these models can be used to obtain estimates of uncertainty in the derived solution. This method makes no assumptions about the shape of an *a posteriori* probability density function in the model space.

The VFSA Method compares the parameters (model parameters) of an optimization problem and particles in an idealized physical system. A process of physical annealing occurs when a solid in a heat bath is initially heated by increasing the temperature so that the particles are distributed randomly in a liquid phase. Then a slow cooling process follows, so that the particles arrange themselves in the low-energy ground state where crystallization happens. The optimization process involves the simulation of the evolution of the physical system as it cools down and anneals in a state of minimum energy. In the terminology of stochastic processes every particles configuration is defined as *state*. At each temperature, the solid is allowed to reach thermal equilibrium, where the probability of being in a state i with energy E_i is given by the following Gibbs or Boltzmann pdf:

$$P(E_i) = \frac{exp\left(-\frac{E_i}{KT}\right)}{\sum_{j \in S} exp\left(-\frac{E_j}{KT}\right)} = \frac{1}{Z(T)} exp\left(-\frac{E_i}{KT}\right) \tag{4.8}$$

where the set S is made of all the possible configurations, K is the Boltzmann's constant, T is the temperature and $Z(T)$, partition function, which is given by

$$Z(T) = \sum_{j \in S} exp\left(-\frac{E_j}{KT}\right) \tag{4.9}$$

The temperature is gradually reduced after the thermal equilibrium is reached so that in the limit $T \to 0$, the state of minimum energy becomes intensely probable. The key to this process is the requirement of the equilibrium. If the cooling is too rapid (quenching), the material will freeze at a local minimum of E_j, forming a glass. Nevertheless, if the melt is cooled too slowly, annealing), the nit will eventually freeze at an energy state that is very close to the global minimum of E_j, forming a crystal (Sen & Stoffa, 2013).

In our case the VFSA algorithm is characterized by a starting model with a random distribution, limited between the constraints assigned. From this model we calculated an initial error (objective function) between the scaling function of the observed data and the scaling function calculated of this model. Now we assigned an initial temperature T_{0i} and let this temperature, that will tend to a value of zero, to change for any iteration, assuming for example a total iteration

number equal to 1000. For each temperature $T_i(k)$ (eq. 4.10) we have a new model with a Cauchy distribution, a distribution that depends on the temperature, and calculate a new error function that is subtracted to the previous one. If the new error function decreases, we proceed to the next state of temperature, until the allowed maximum of iterations is reached. The final model will have an error function representing the global minimum error, with a temperature equal to T_{fi} (eq. 4.11).

$$T_i(k) = T_{0i} exp\left(-c_i k^{1/NM}\right) \quad (4.10)$$

where $T_i(k)$ is the temperature at iteration k, T_{0i} is the initial temperature for model parameter i, c_i is the parameter used to control the temperature schedule which helps tuning the algorithm for specific problems, and NM is the number of model parameters. c_i must be chosen such as

$$T_{fi} = T_{0i} exp(-m_i) \quad (4.11)$$

where the final iteration $k_i = exp\ n_i$ and T_{fi} is the final temperature (Ingber 1989; Ingber and Rosen 1992). Thus:

$$c_i = m_i exp(-n_i/NM) \quad (4.12)$$

CHAPTER 5. MHODE INVERSION (SYNTHETIC CASE)

Once implemented the new formulae of the field and its derivative in the MHODE inversion algorithm, for the case 2.5D and 2.x D, we now test the inversion based on these forward problems in a synthetic case.

5.1. Forward problem

First, we created a 3D polyhedral source-model (Tsoulis, 2012), the source being made of 199 vertices, with a 1 g/cm^3density (Figure 5.1). We calculate with the 3D formulae of Tsoulis the maps of the gravity field and its first order vertical derivative of the synthetic polyhedral source-model (Figure 5.2). These maps will be our observed data. From these we extract 7 profiles, 4 distributed along the x direction and the other 3 along the y direction (Figure 5.3).

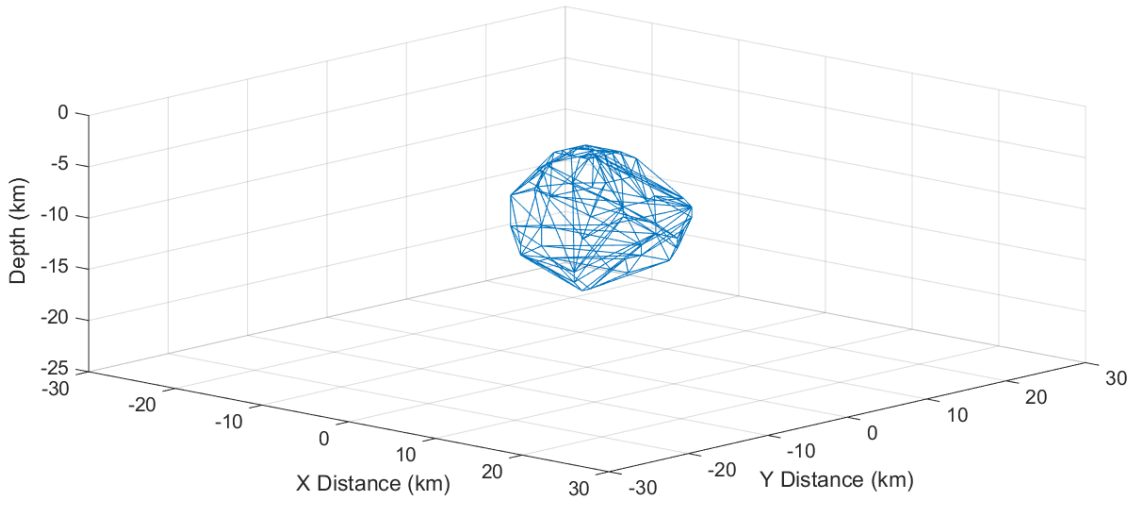

Figure 5.1 - 3D Geometric representation of the source model. The 3D model is a combination of 7 profiles, 4 profiles along the x direction and 3 profiles along y direction.

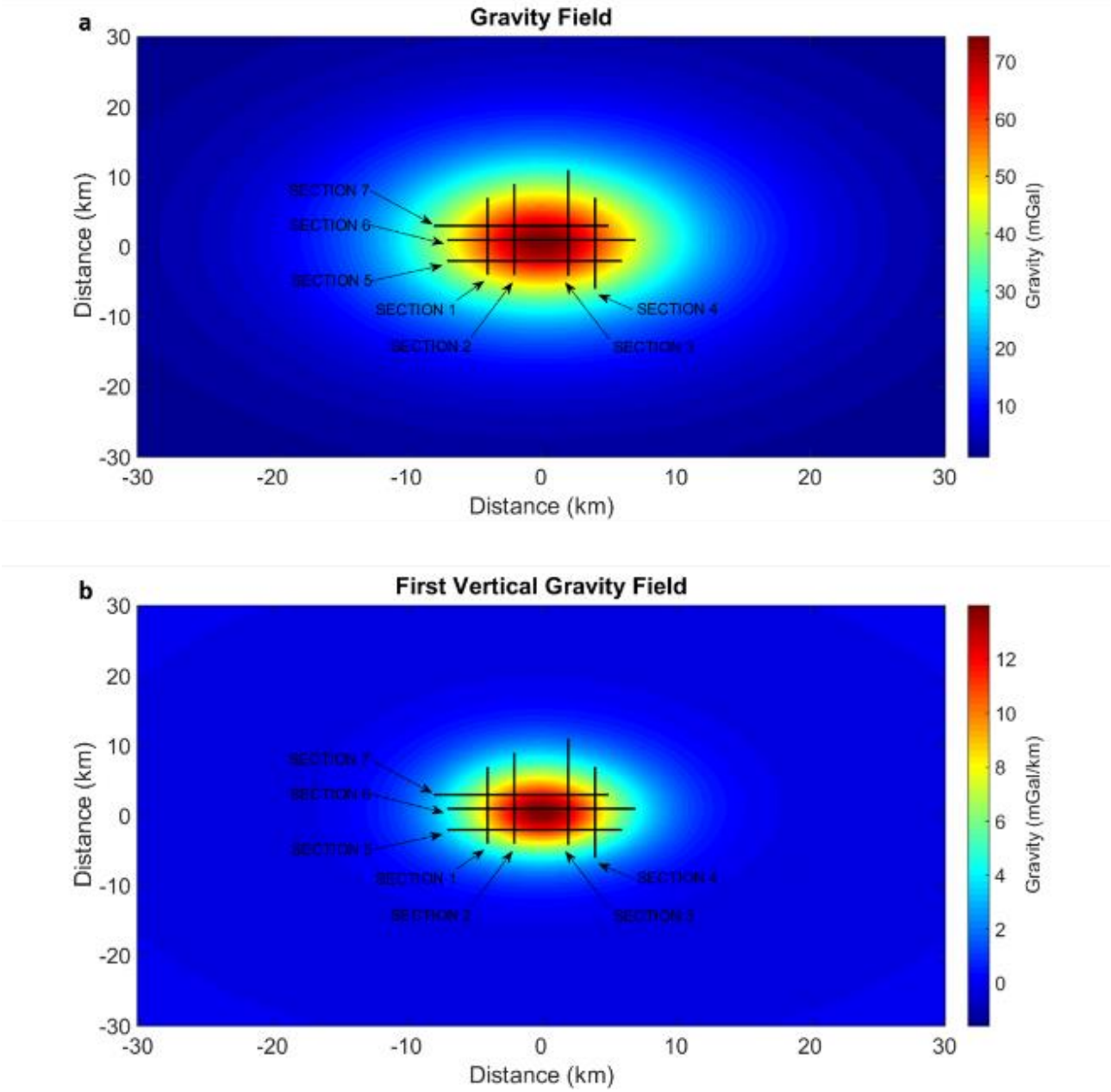

Figure 5.2 – a) Map of 3D gravity field with a plan view of the sections chosen; b) Map of 3D first order vertical derivative of the gravity field with a plan view of the sections chosen.

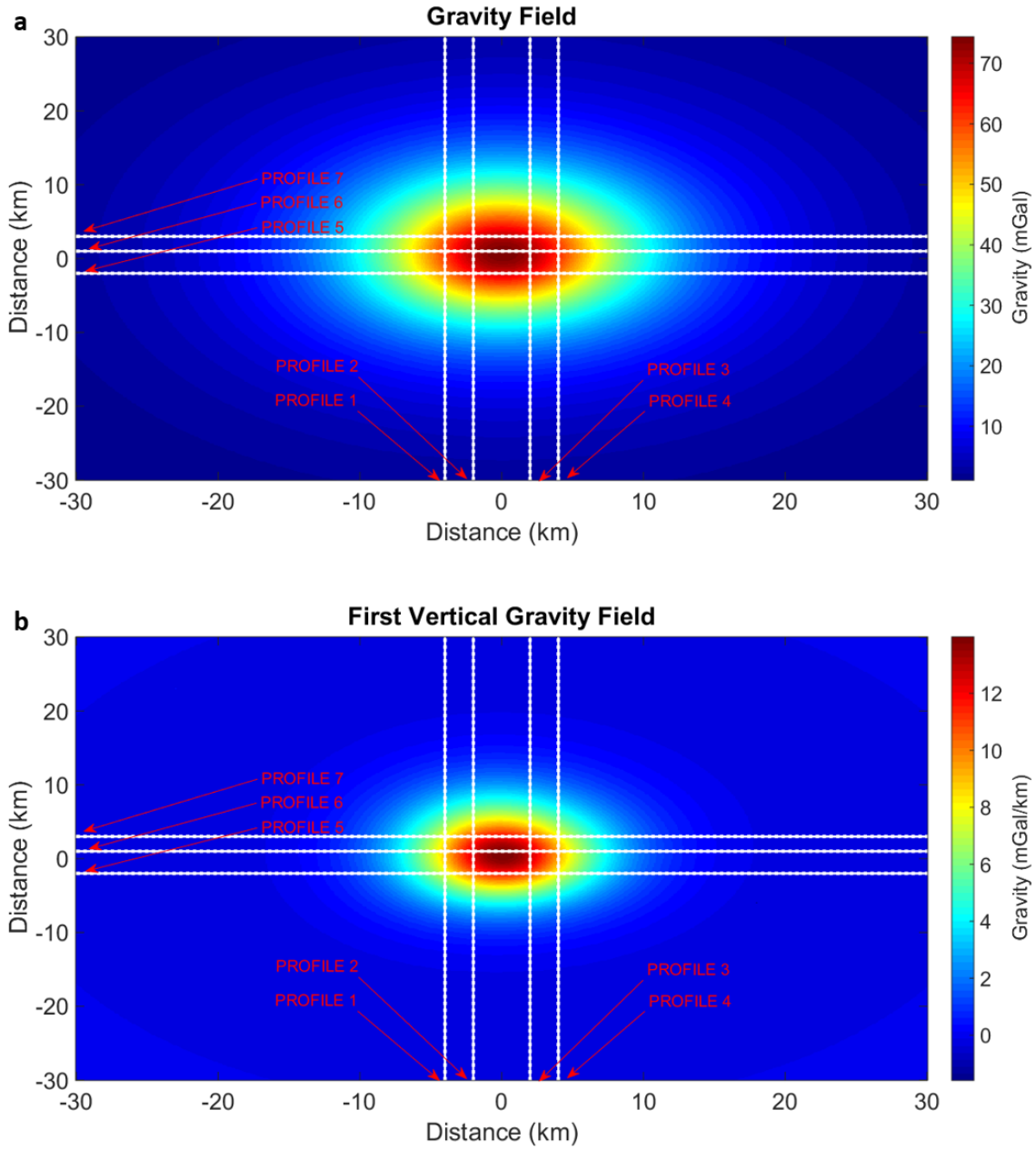

Figure 5.3 – a) Projections of the profiles chosen for the study of synthetic case on the map of 3D gravity field; b) Projections of the profiles chosen for the study of synthetic case on the map of 3D first order vertical derivative of the gravity field.

5.1.1 Forward problem for the 2.x D sections

Therefore, for each profile extracted we have the observed field and the first order vertical derivative of the field for a 3D source (Figures 5.4 – 5.10). When we calculate in a forward 2.x D, we assume that each profile model has a finite length of the strike direction, therefore for each profile we know the profile exact position with respect to the source along the strike direction.

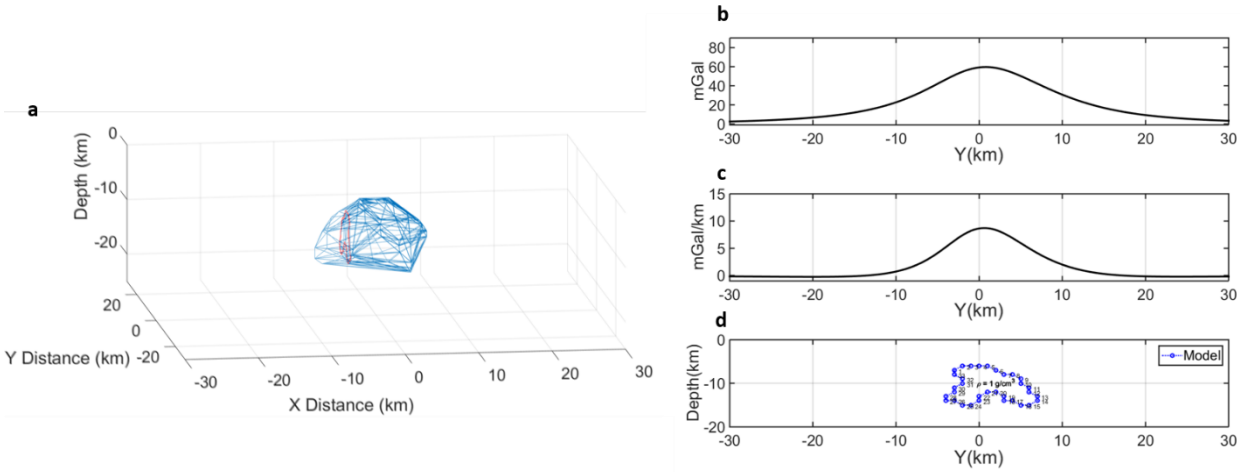

Figure 5.4 – The profile evidenced is the profile number 1, it develops on the y length and it has x = -4 km coordinate. a) 3D Representation of the section profile extracted from the 3D model. b) The observed gravity field anomaly for the profile. c) The observed first order derivative of the gravity field anomaly for the profile. d) Geometric representation of the section extracted from the 3D model, constituted by 33 vertices, with a density contrast of 1 g/cm^3.

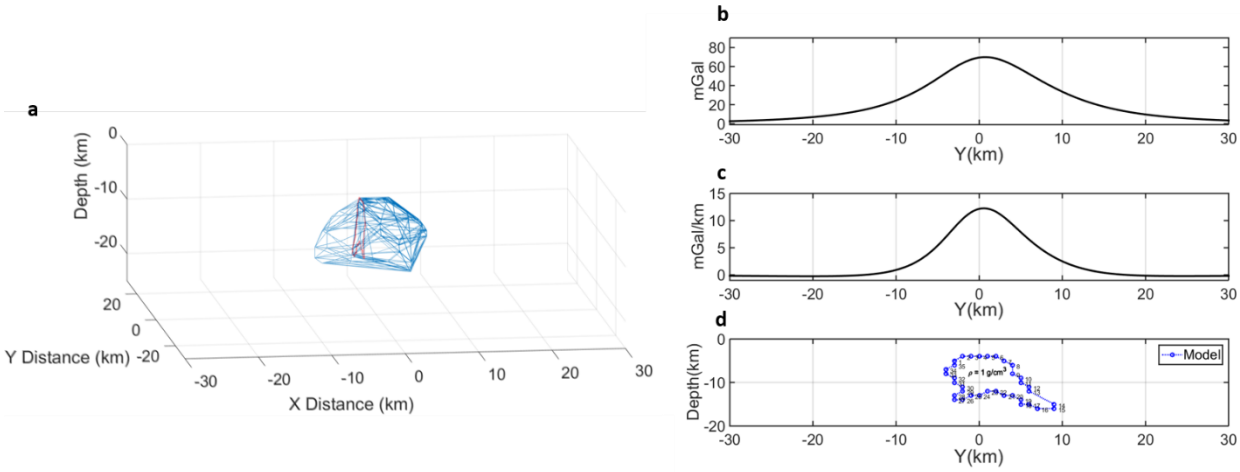

Figure 5.5 – The profile evidenced is the profile number 2, it develops on the y length and it has x = -2 km coordinate. a) 3D Representation of the section profile in the 3D model. b) The observed gravity field anomaly for the profile. c) The observed first order derivative of the gravity field anomaly for the profile. d) Geometric representation of the section extracted from the 3D model, constituted by 35 vertices, with a density contrast of 1 g/cm^3.

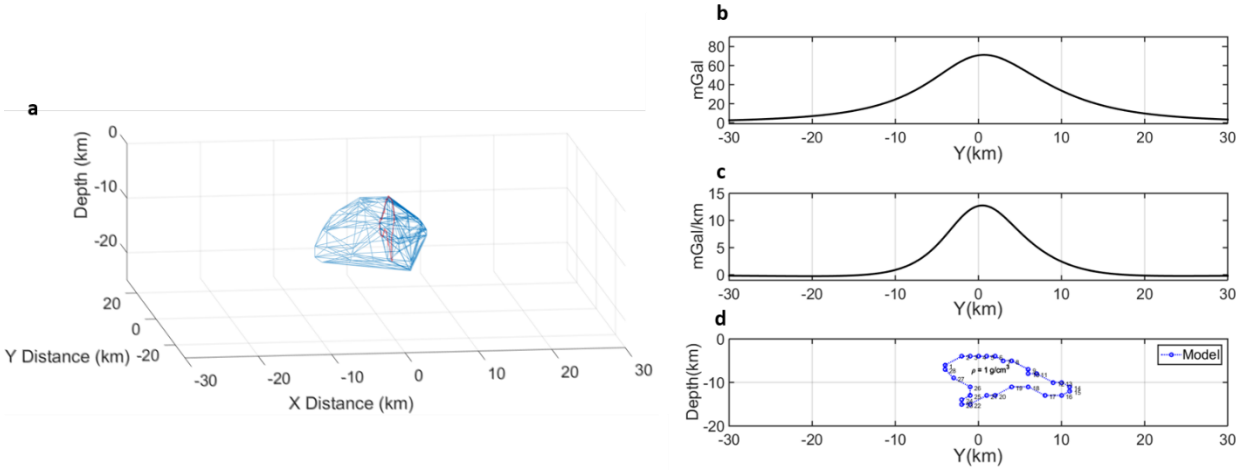

Figure 5.6 – The profile evidenced is the profile number 3, it develops on the y length and it has x = 2 km coordinate. a) 3D Representation of the section profile in the 3D model. b) The observed gravity field anomaly for the profile. c) The observed first order derivative of the gravity field anomaly for the profile. d) Geometric representation of the section extracted from the 3D model, constituted by 28 vertices, with a density contrast of 1 g/cm^3.

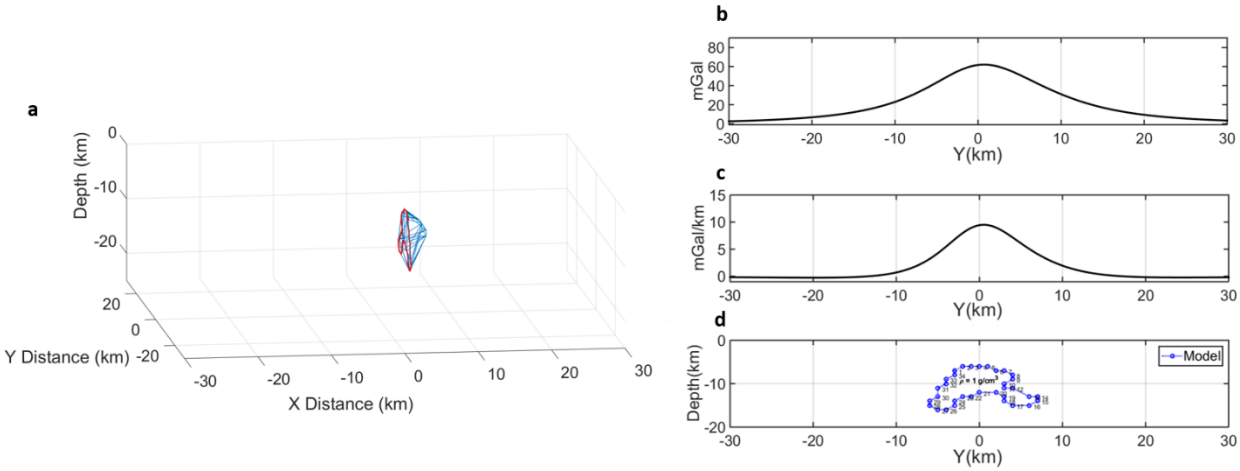

Figure 5.7 – The profile evidenced is the profile number 4, it develops on the y length and it has x = 4 km coordinate. a) 3D Representation of the section profile in the 3D model. b) The observed gravity field anomaly for the profile. c) The observed first order derivative of the gravity field anomaly for the profile. d) Geometric representation of the section extracted from the 3D model, constituted by 34 vertices, with a density contrast of 1 g/cm^3.

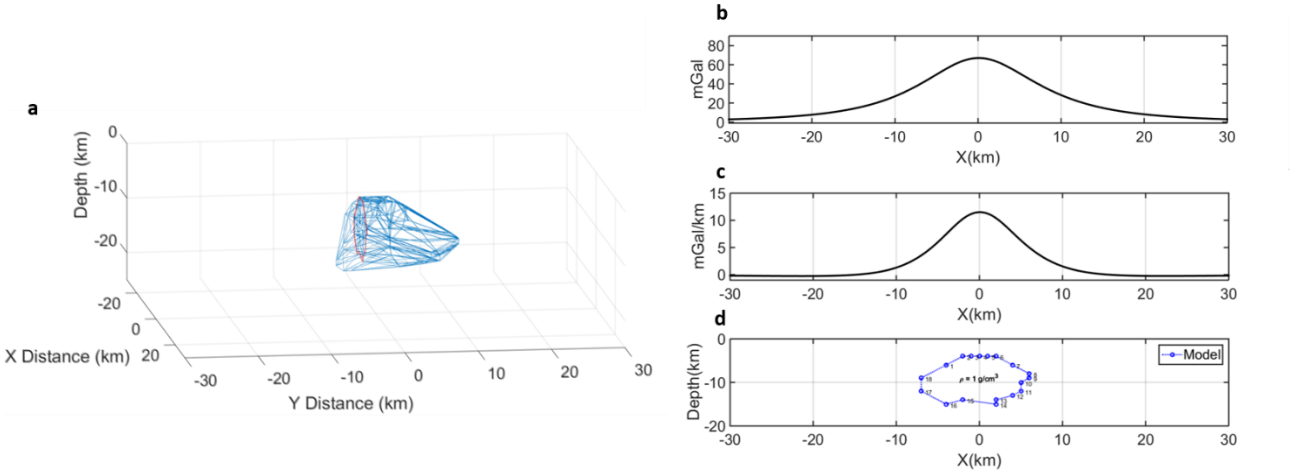

Figure 5.8 – The profile evidenced is the profile number 5, it develops on the x length and it has y = -2 km coordinate. a) 3D Representation of the section profile in the 3D model. b) The observed gravity field anomaly for the profile. c) The observed first order derivative of the gravity field anomaly for the profile. d) Geometric representation of the section extracted from the 3D model, constituted by 18 vertices, with a density contrast of 1 g/cm^3.

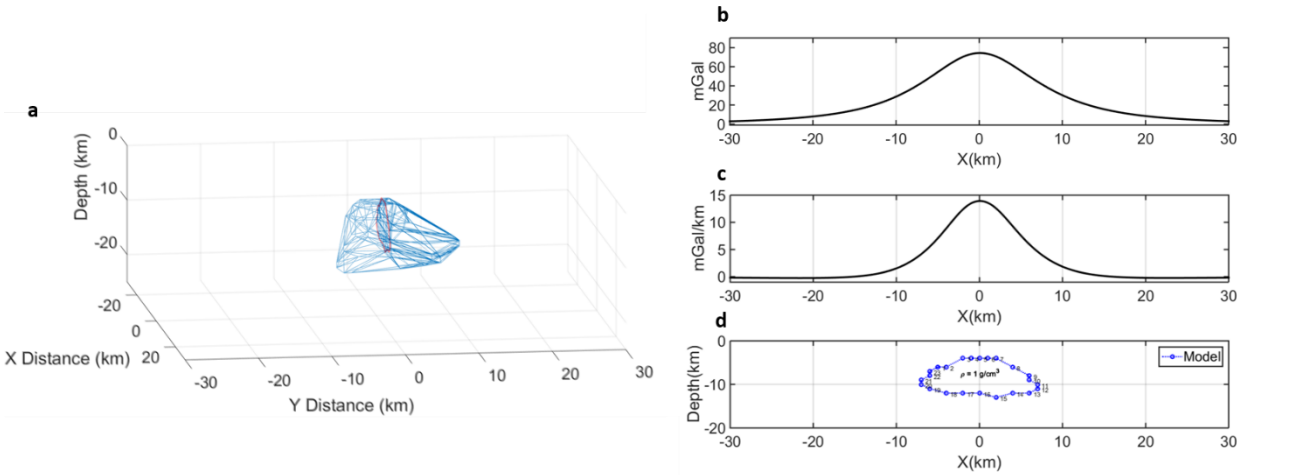

Figure 5.9 – The profile evidenced is the profile number 6, it develops on the x length and it has y = 1 km coordinate. a) 3D Representation of the section profile in the 3D model. b) The observed gravity field anomaly for the profile. c) The observed first order derivative of the gravity field anomaly for the profile. d) Geometric representation of the section extracted from the 3D model, constituted by 23 vertices, with a density contrast 1 g/cm^3.

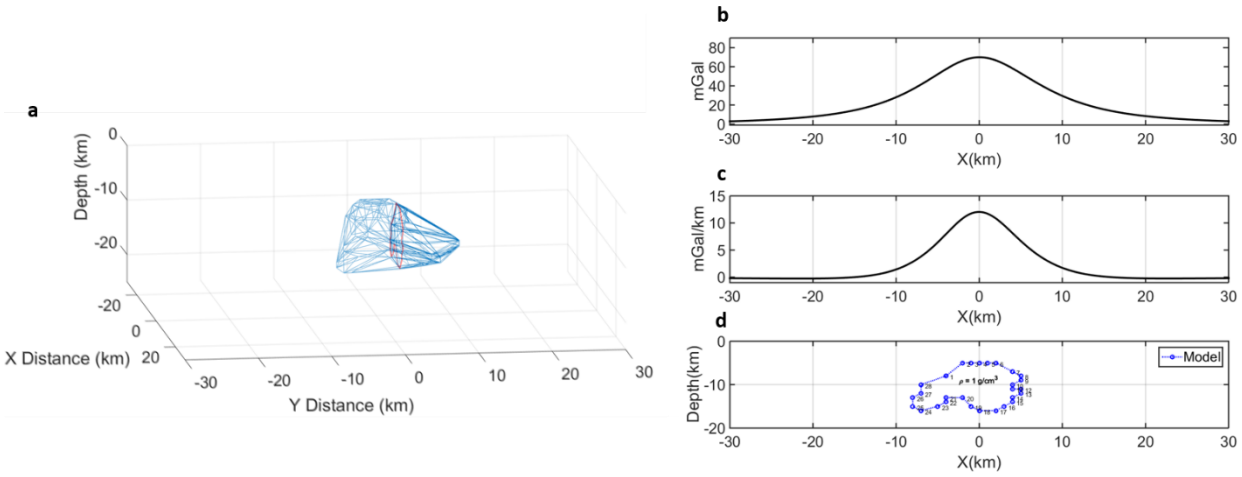

Figure 5.10 – The profile evidenced is the profile number 7, it develops on the x length and it has y = 3 km coordinate. a) 3D Representation of the section profile in the 3D model. b) The observed gravity field anomaly for the profile. c) The observed first order derivative of the gravity field anomaly for the profile. d) Geometric representation of the section extracted from the 3D model, constituted by 28 vertices, with a density contrast 1 g/cm^3.

It is important to notice that, choosing a profile that is farther from the source centre and closer to the source bound, the gravimetry anomaly intensity decreases.

5.1.2 Multiridge Analysis of a forward problem

Once we have the observed field and its derivatives for all profiles, we calculate the ridges of these for each profile thanks to the Analysis of Multiridges (see Chapter 2). The ridge along which we will calculate the scaling function represents the points where the horizontal derivative is equal to zero (Figures 5.11 – 5.17).

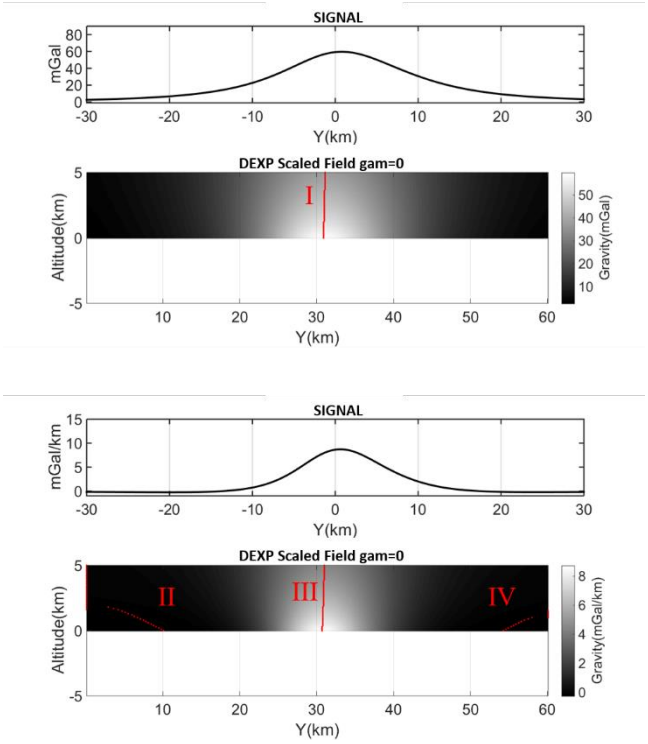

Figure 5.11 – for Profile 1: I is the ridge of the gravity field; II – III – IV are the ridges of the first order vertical derivative of the gravity field.

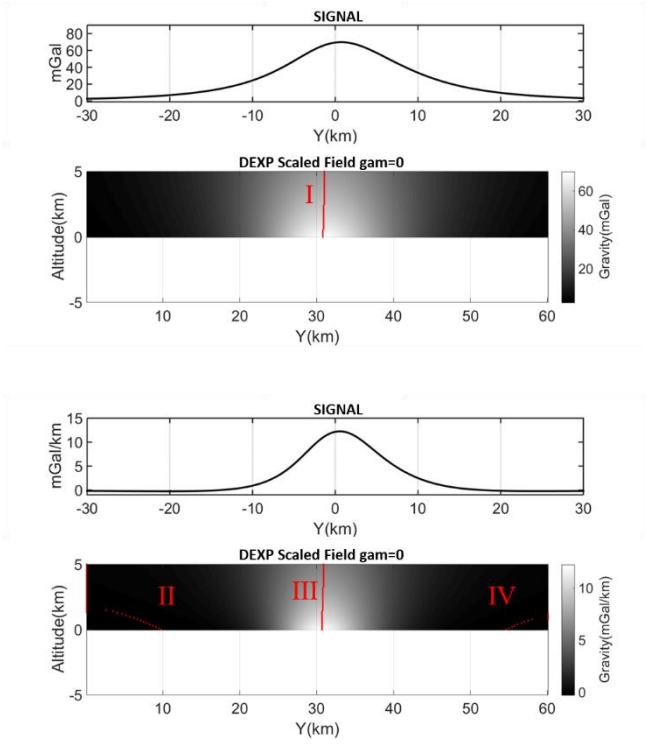

Figure 5.12 – for Profile 2: I is the ridge of the gravity field; II – III – IV are the ridges of the first order vertical derivative of the gravity field.

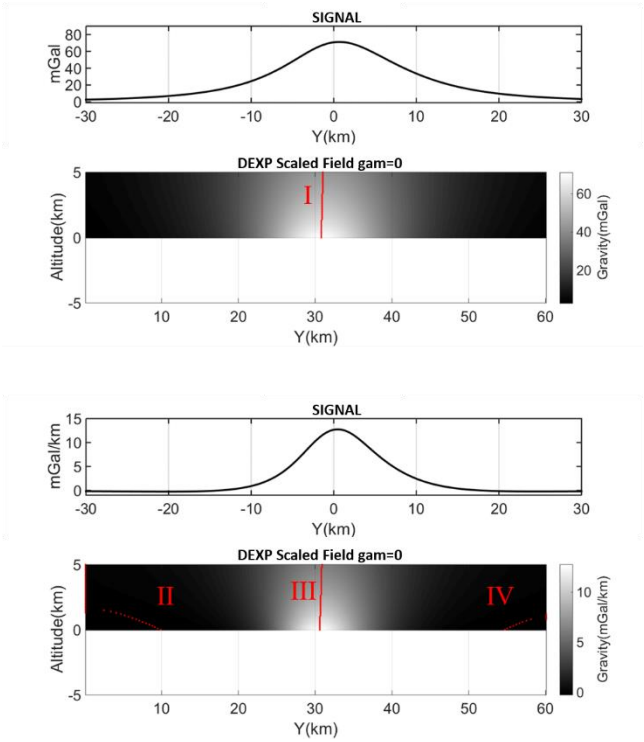

Figure 5.13 – for Profile 3: I is the ridge of the gravity field; II – III – IV are the ridges of the first order vertical derivative of the gravity field.

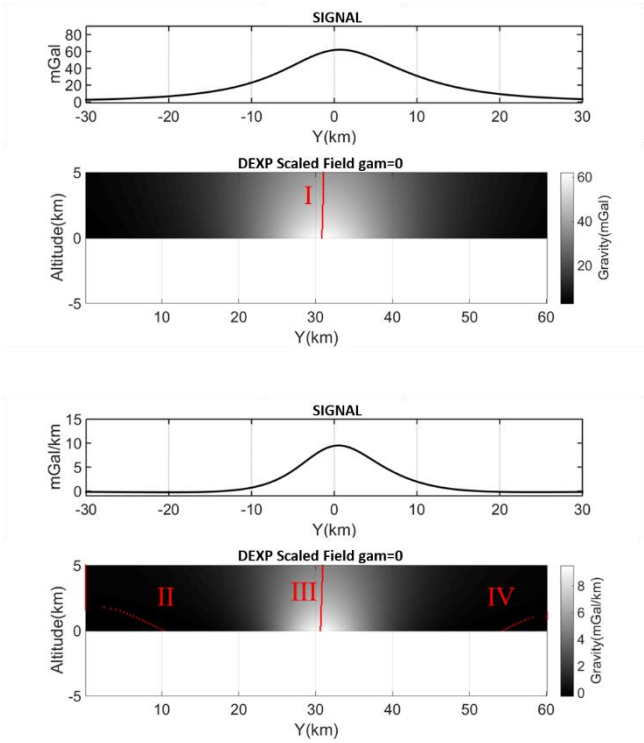

Figure 5.14 – for Profile 4: I is the ridge of the gravity field; II – III – IV are the ridges of the first order vertical derivative of the gravity field.

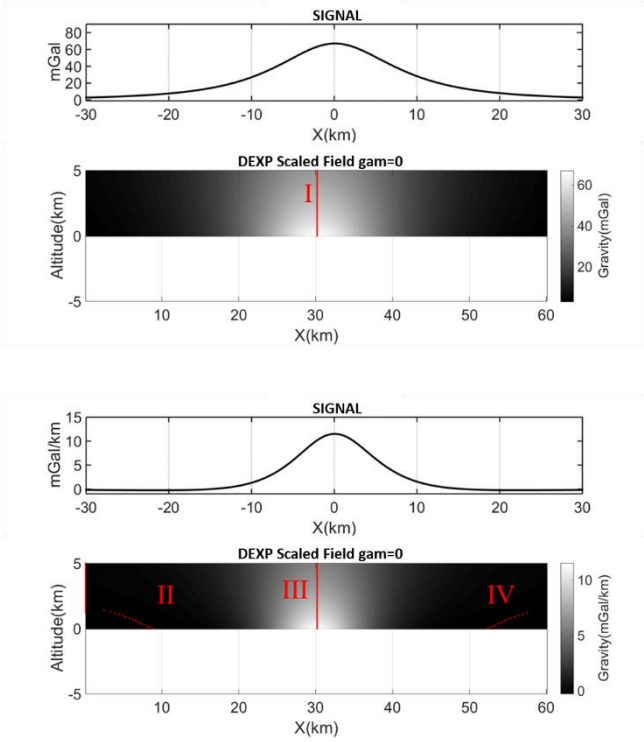

Figure 5.15 – for Profile 5: I is the ridge of the gravity field; II – III – IV are the ridges of the first order vertical derivative of the gravity field.

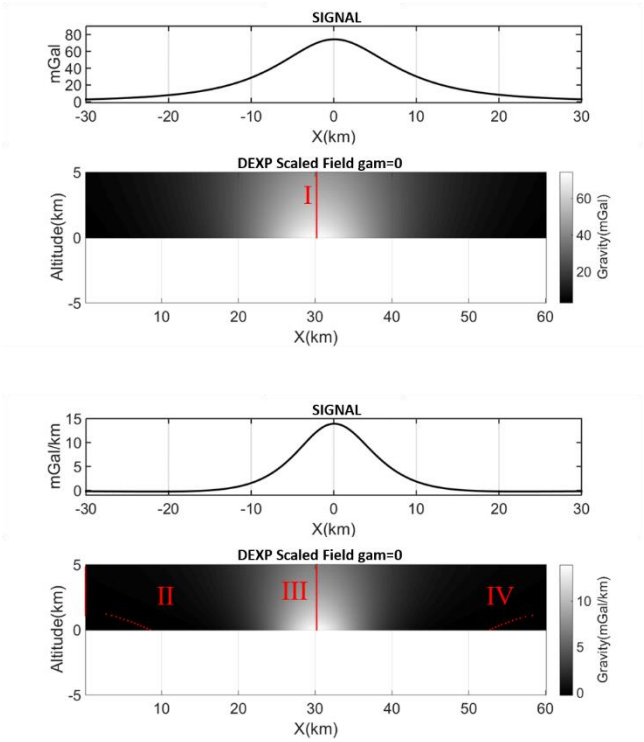

Figure 5.16 – for Profile 6: I is the ridge of the gravity field; II – III – IV are the ridges of the first order vertical derivative of the gravity field.

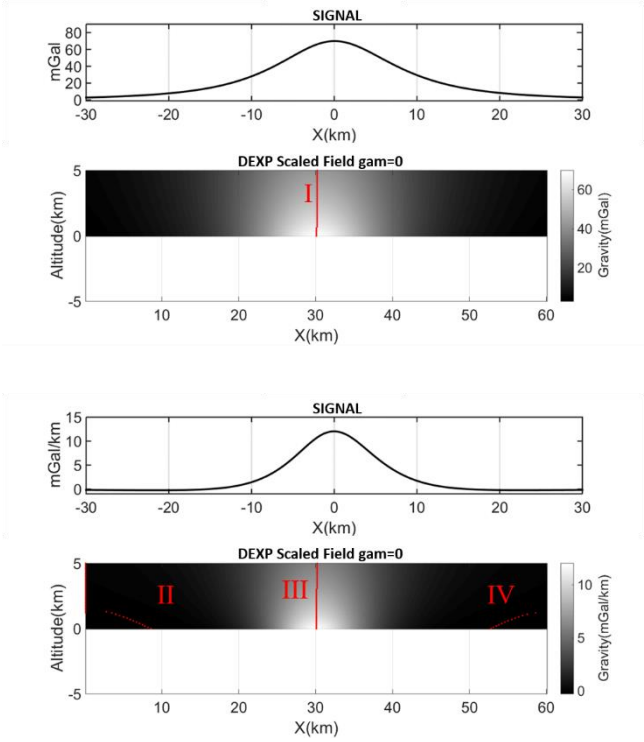

Figure 5.17 – for Profile 7: I is the ridge of the gravity field; II – III – IV are the ridges of the first order vertical derivative of the gravity field.

5.2 Inversion model

5.2.1 The scaling function for the 2.x D sections

The fundamental parameter of our type of inversion, as we said in the previous chapters, is the scaling function. It does not depend on the density but only on the geometric characteristics of the source (the coordinates of the vertices). We show in the next figures, from 5.18 to 5.24, the comparison between the scaling function observed (the scaling function calculated for the profiles extracted from 3D gravity map) and the scaling function calculated with VFSA algorithm:

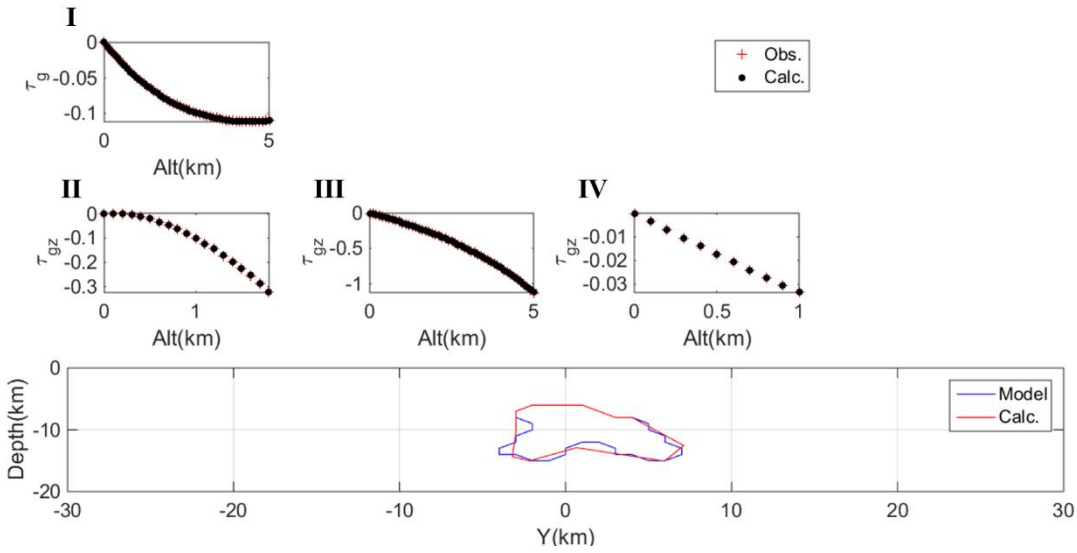

Figure 5.18 – Comparison between the observed scaling functions and calculated scaling functions, I: compare between scaling functions for the gravity field; II – III – IV: compare between scaling functions for the first order vertical derivative of the gravity field. Comparison between real model and calculated model for profile 1.

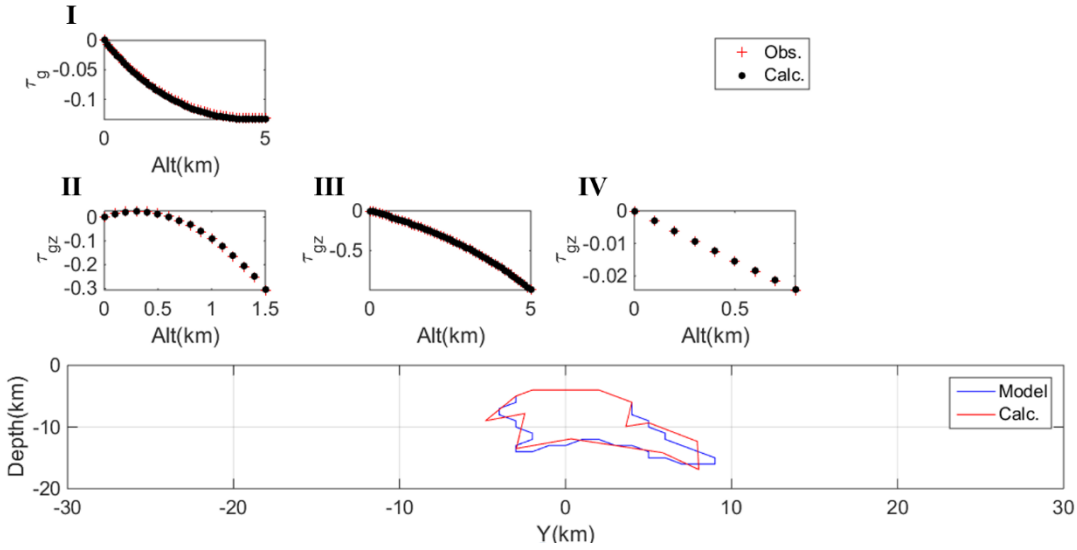

Figure 5.19 – Comparison between the observed scaling functions and calculated scaling functions, I: compare between scaling functions for the gravity field; II – III – IV: compare between scaling functions for the first order vertical derivative of the gravity field. Comparison between real model and calculated model for profile 2.

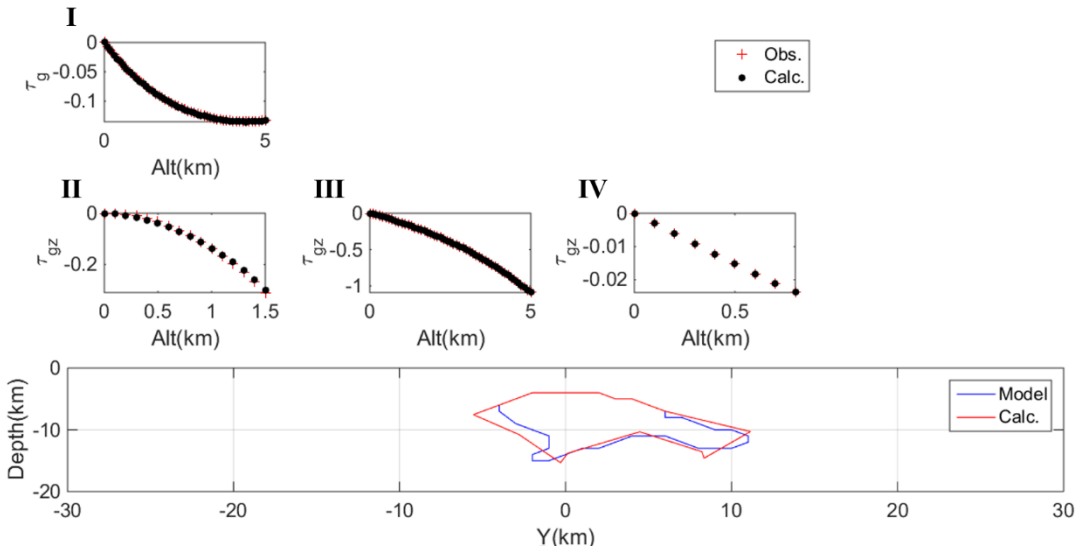

Figure 5.20 – Comparison between the observed scaling functions and calculated scaling functions, I: compare between scaling functions for the gravity field; II – III – IV: compare between scaling functions for the first order vertical derivative of the gravity field. Comparison between real model and calculated model for profile 3.

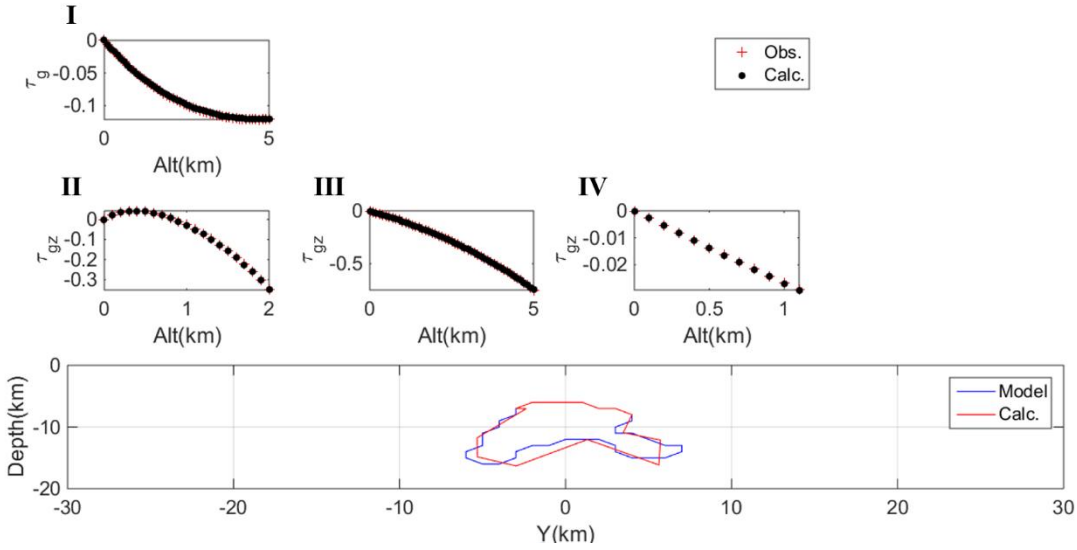

Figure 5.21 – Comparison between the observed scaling functions and calculated scaling functions, I: compare between scaling functions for the gravity field; II – III – IV: compare between scaling functions for the first order vertical derivative of the gravity field. Comparison between real model and calculated model for profile 4.

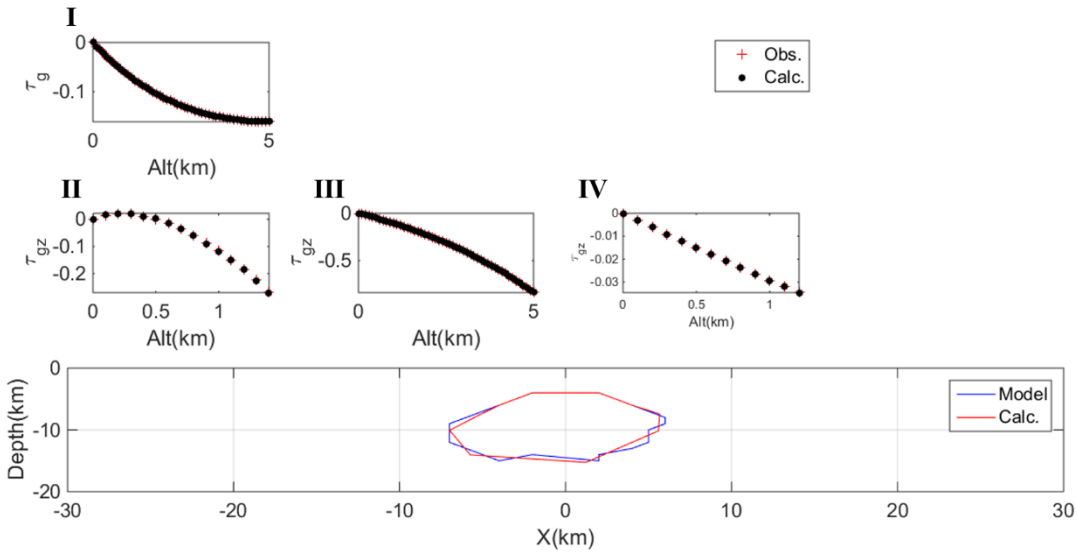

Figure 5.22 – Comparison between the observed scaling functions and calculated scaling functions, I: compare between scaling functions for the gravity field; II – III – IV: compare between scaling functions for the first order vertical derivative of the gravity field. Comparison between real model and calculated model for profile 5.

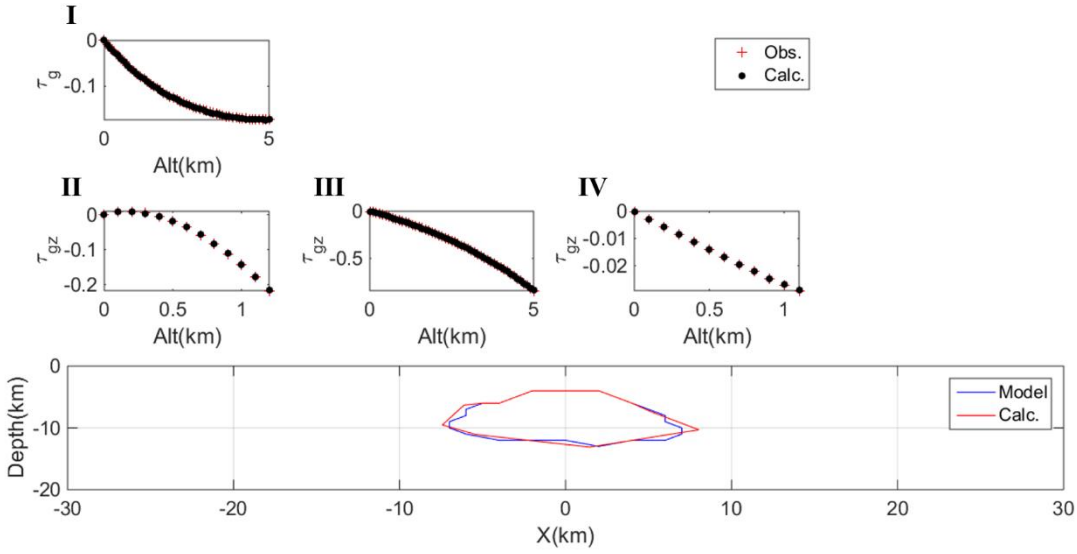

Figure 5.23 – Comparison between the observed scaling functions and calculated scaling functions, I: compare between scaling functions for the gravity field; II – III – IV: compare between scaling functions for the first order vertical derivative of the gravity field. Comparison between real model and calculated model for profile 6.

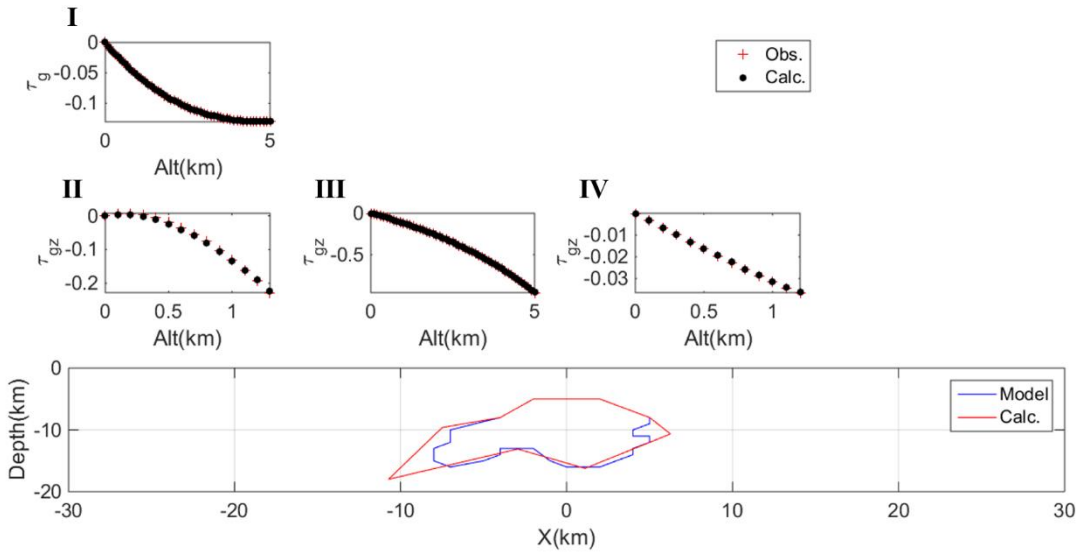

Figure 5.24 – Comparison between the observed scaling functions and calculated scaling functions, I: compare between scaling functions for the gravity field; II – III – IV: compare between scaling functions for the first order vertical derivative of the gravity field. Comparison between real model and calculated model for profile 7.

5.2.2 Geometric models obtained with 2.x D inversion

In the next figures (5.25 – 5.31) we will show the geometric models obtained with 2.x D inversion. To obtain these models by 2.x D MHODE inversion first, we put in the algorithm, if there are, some constraints. For example, we can assume that we know the vertices at the top of source coordinates through seismic information. Second, we assume a finite length for the strike direction; third, we choose a strategy to build the calculated model, and we let the algorithm free to calculate the final result, firstly inserting few vertices with the large range for bound along the coordinate *x* and *z*, and step by step, inversion by inversion. Then we take in to account the inversion result, but increase the number of vertices and reduce the width of the bounds, up to an optimal resolution for the geometrical problem (Chauhan, Fedi & Sen, 2018). During the MHODE inversion, the VFSA (Very Fast Simulated Annealing) inversion algorithm calculates the objective function (minimal error) for the quantity of the scaling function (see chapter 4), and solves the equations system that has only geometric unknowns, because the scaling function has the peculiarity of not depending on the density.

In the case of the model 1 we fixed 8 vertices to the top and for the sides and the bottom we inverted 6 vertices, leaving them free to move along *x* and *z* directions.

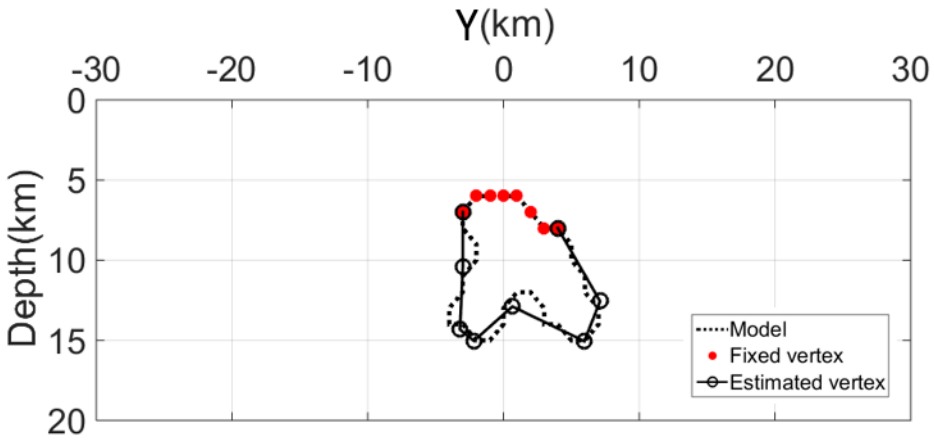

Figure 5.25 – Profile 1: comparison between the real model and the inverted model. The continue line represents the real model, while the dot line represents the inverted model. The red dots are fixed vertices, the black circles are the vertices free to move in the bounds along x and z coordinates. The y coordinate of the profile along the strike length is x = -4 km.

For the model 2 we fixed 8 vertices to the top and for the sides and the bottom we inverted 9 vertices, leaving them free to move along *x* and *z* directions.

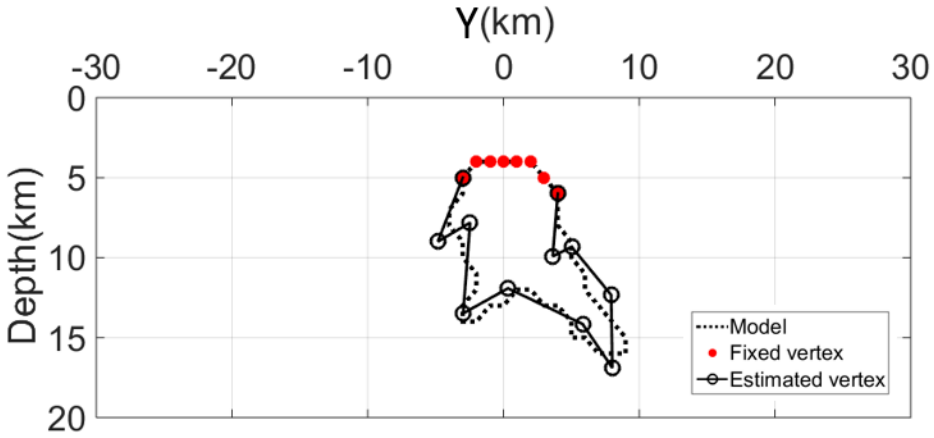

Figure 5.26 – Profile 2: comparison between the real model and the inverted model. The continue line represents the real model, while the dot line represents the inverted model. The red dots are fixed vertices, the black circles are the vertices free to move in the bounds along x and z coordinates. The y coordinate of the profile along the strike length is x = -2 km.

While in the case of the model 3 we fixed 9 vertices to the top and for the sides and the bottom we inverted 8 vertices leaving them free to move along *x* and *z* directions.

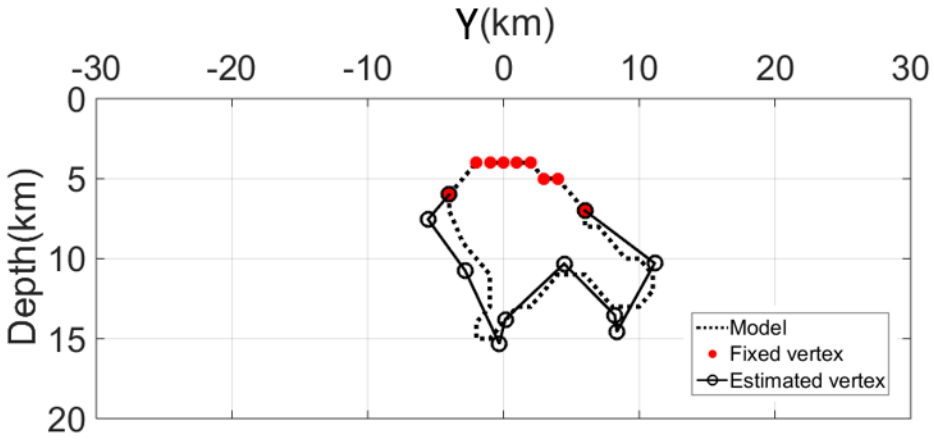

Figure 5.27 – Profile 3: comparison between the real model and the inverted model. The continue line represents the real model, while the dot line represents the inverted model. The red dots are fixed vertices, the black circles are the vertices free to move in the bounds along x and z coordinates. The y coordinate of the profile along the strike length is x = 2 km.

For the model 4 we fixed 8 vertices to the top and for the sides and the bottom we inverted 8 vertices, leaving them free to move along *x* and *z* directions

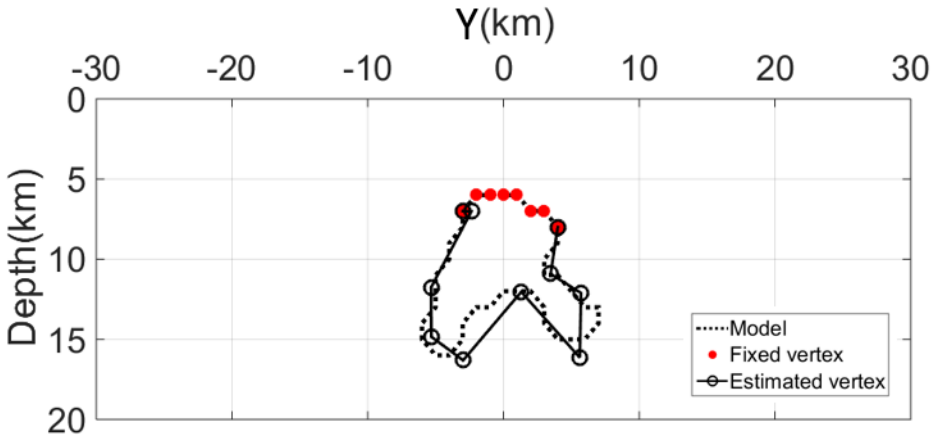

Figure 5.28 – Profile 4: comparison between the real model and the inverted model. The continue line represents the real model, while the dot line represents the inverted model. The red dots are fixed vertices, the black circles are the vertices free to move in the bounds along x and z coordinates. The y coordinate of the profile along the strike length is x = 4 km.

In the case of the model 5 we fixed 7 vertices to the top and for the sides and the bottom we inverted 6 vertices, leaving them free to move along *x* and *z* directions

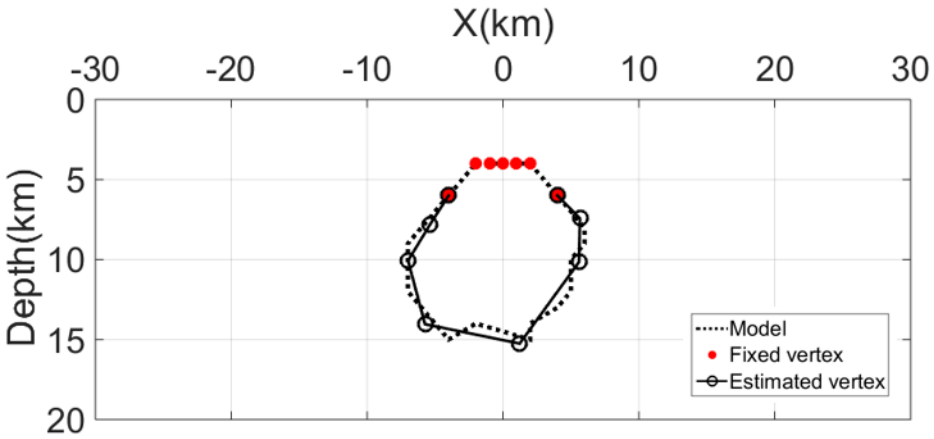

Figure 5.29 – Profile 5: comparison between the real model and the inverted model. The continue line represents the real model, while the dot line represents the inverted model. The red dots are fixed vertices, the black circles are the vertices free to move in the bounds along y and z coordinates. The x coordinate of the profile along the strike length is y = -2 km

.

For the model 6 we fixed 8 vertices to the top and for the sides and the bottom we inverted 6 vertices, leaving leaving them free to move along *x* and *z* directions

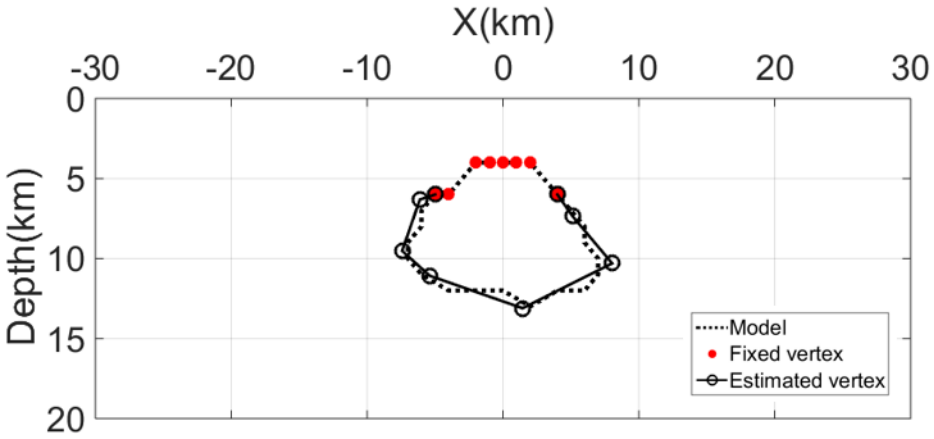

Figure 5.30 – Profile 6: comparison between the real model and the inverted model. The continue line represents the real model, while the dot line represents the inverted model. The red dots are fixed vertices, the black circles are the vertices free to move in the bounds along y and z coordinates. The x coordinate of the profile along the strike length is y = 1 km.

In the end for the model 7 we fixed 8 vertices to the top and for the sides and the bottom we inverted 5 vertices, leaving them free to move along *x* and *z* directions.

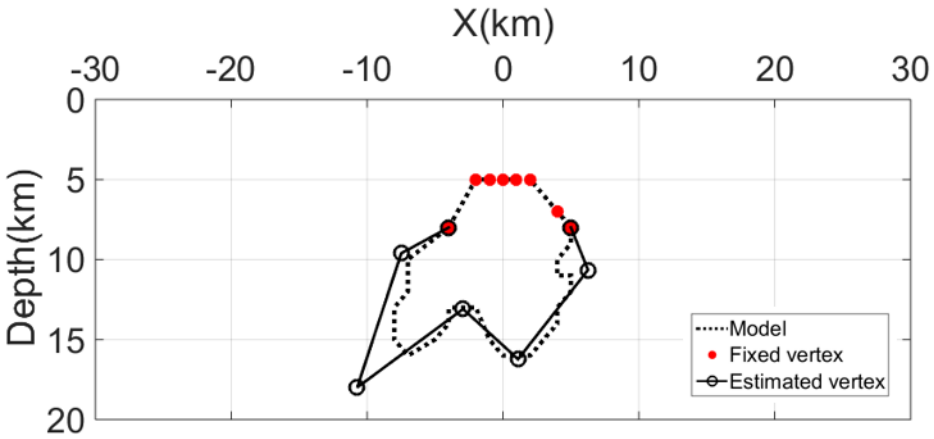

Figure 5.31 – Profile 7: comparison between the real model and the inverted model. The continue line represents the real model, while the dot line represents the inverted model. The red dots are fixed vertices, the black circles are the vertices free to move in the bounds along y and z coordinates. The x coordinate of the profile along the strike length is y = 3 km.

5.2.3 Estimated average density

Once we calculate by MHODE the unknown geometric coordinates, we can estimate the average density, obtained from the slope of the straight line that fits a distribution of points in a scatter plot (figure 5.32) between the observed field and the calculated field, (the last one with unit-density).

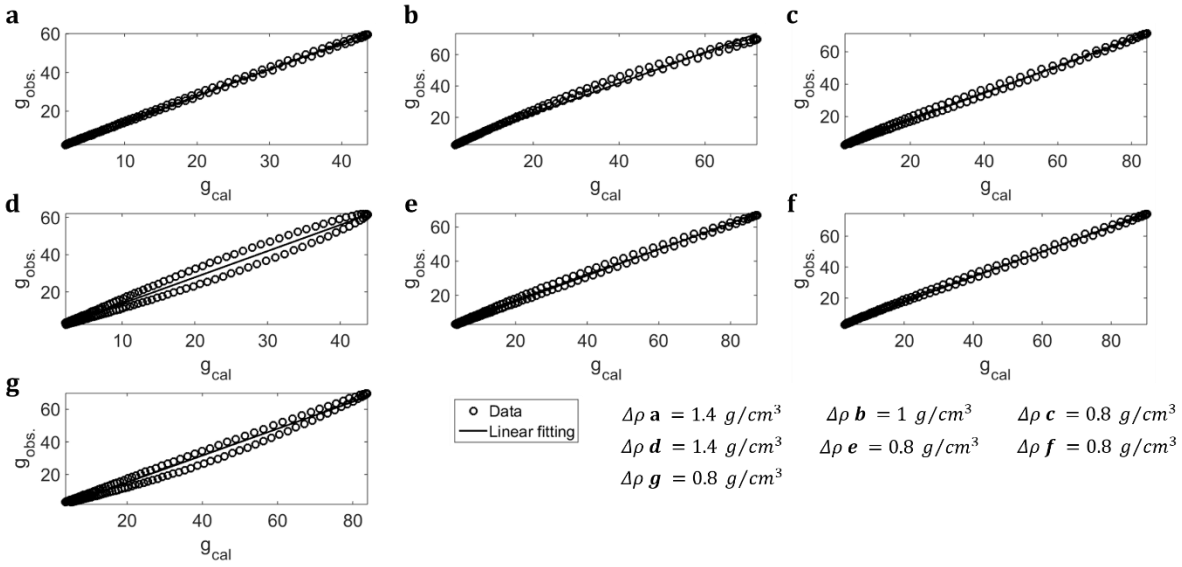

Figure 5.32 – Representation of the all values of estimated density for all profiles, obtained by the slope of the straight line that fits the distribution of points between the observed field and the calculated field, with unitary density for the last, in the scatter plots.

We may notice in figure 5.32 that the density estimated are somewhat different for the sections at the end of the body and in its central part. This difference is related to the approximation of the calculated model in 2.x D dimension. If we consider, for example, the section of the profile 1, this section will have a deeper top with respect to the middle section of profile 2. When we calculate the 2.x D model of the section of the profile 1, we consider all along the strike direction the same section, so in this case we are underestimating the real mass of the body, and the value of the estimated density is increased. We have the opposite situation for the section of profile 3, where we have an overestimation of the mass of the body source. Nevertheless, this difference is not a problem, because if we calculate the mean estimated density for the whole body, this will be equal 1 g/cm^3, which is the real value of the density of the synthetic body. And especially because these values will be used to form a reference model with a full 3D algorithm, which will finally establish the correct density distribution in the body.

5.2.4 Calculation of the field and of its derivative with the estimated average density

By the estimated density and source geometry, we may now calculate the field and its derivatives, and compare them with the observed field and derivative data (Figures 5.33 – 5.39)

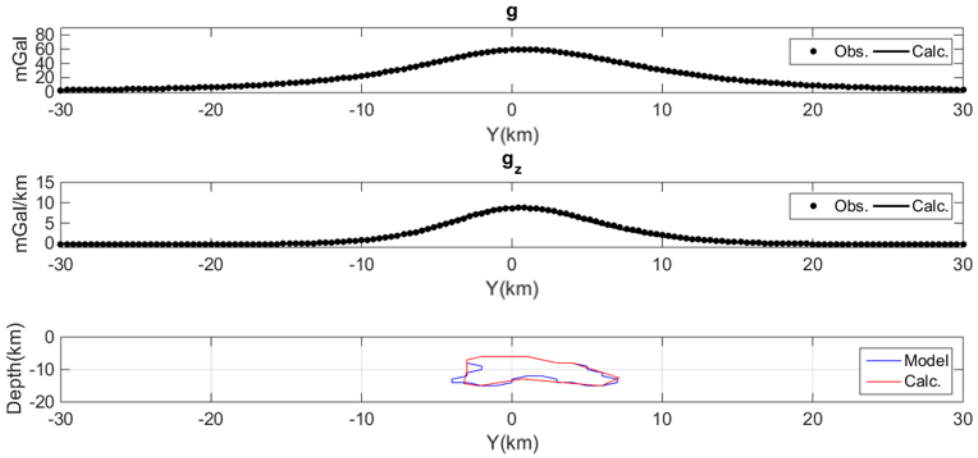

Figure 5.33 – Comparison between fields, first-order derivatives and between real model and calculated model for profile 1.

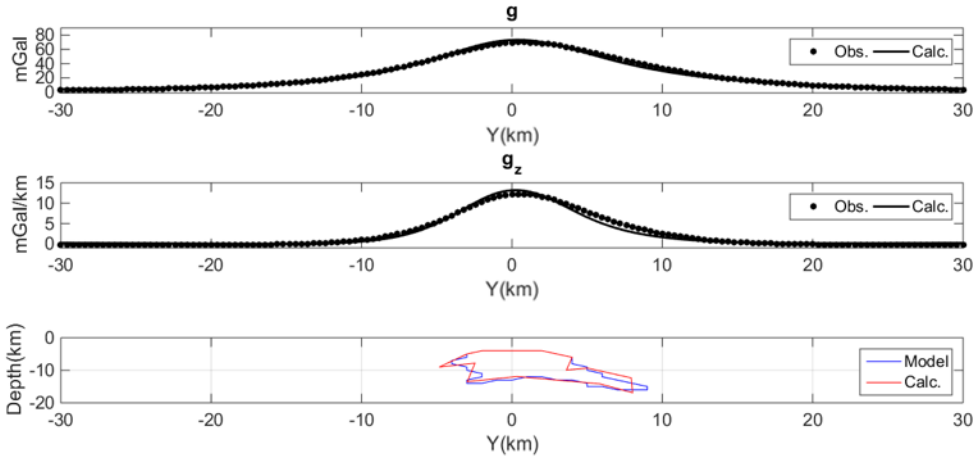

Figure 5.34 – Comparison between fields, first-order derivatives and between real model and calculated model for profile 2.

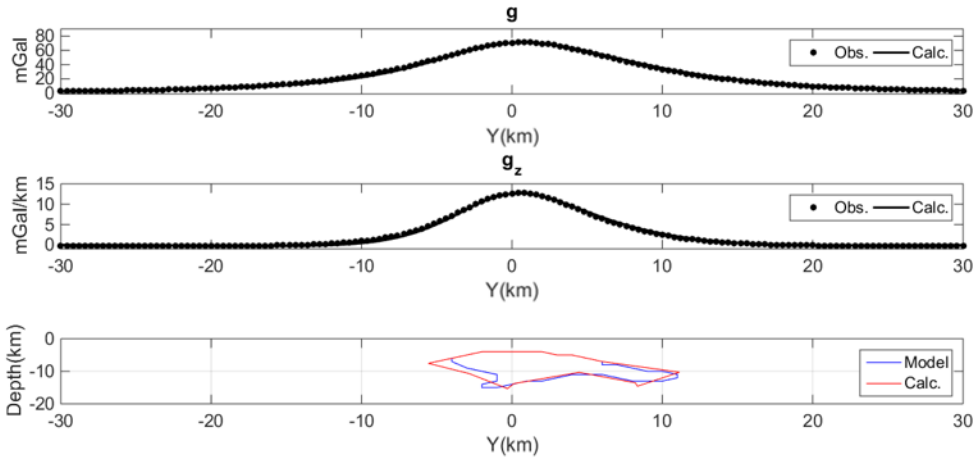

Figure 5.35 – Comparison between fields, first-order derivatives and between real model and calculated model for profile 3.

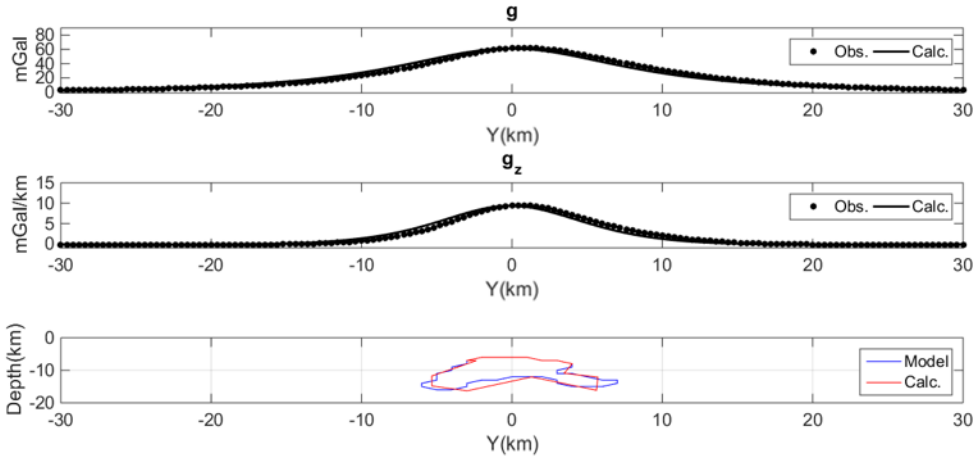

Figure 5.36 – Comparison between fields, first-order derivatives and between real model and calculated model for profile 4.

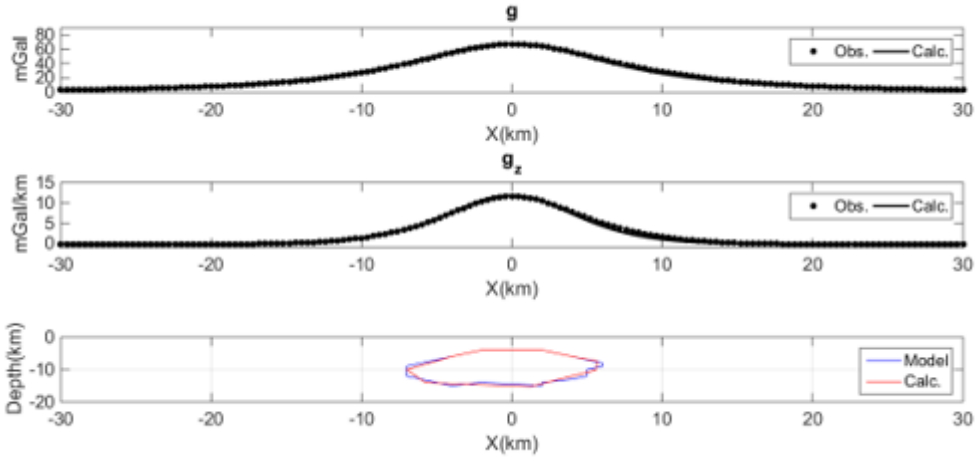

Figure 5.37 – Comparison between fields, first-order derivatives and between real model and calculated model for profile 5.

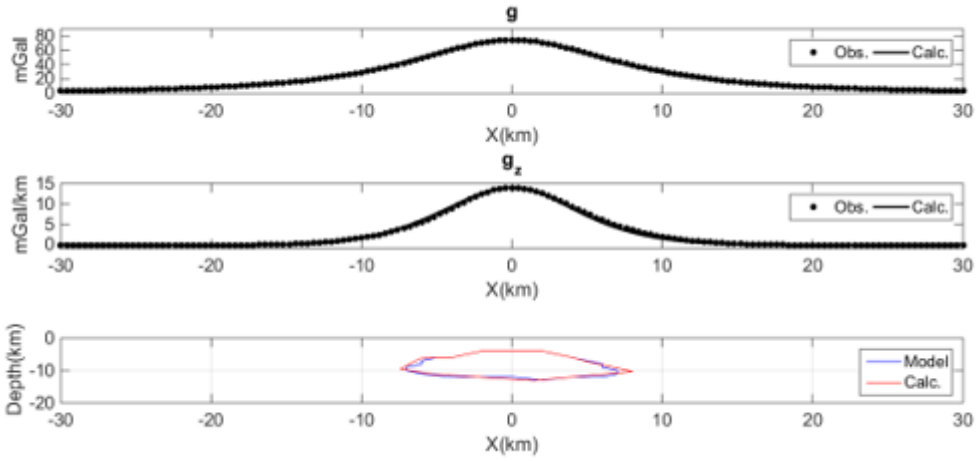

Figure 5.38 – Comparison between fields, first-order derivatives and between real model and calculated model for profile 6.

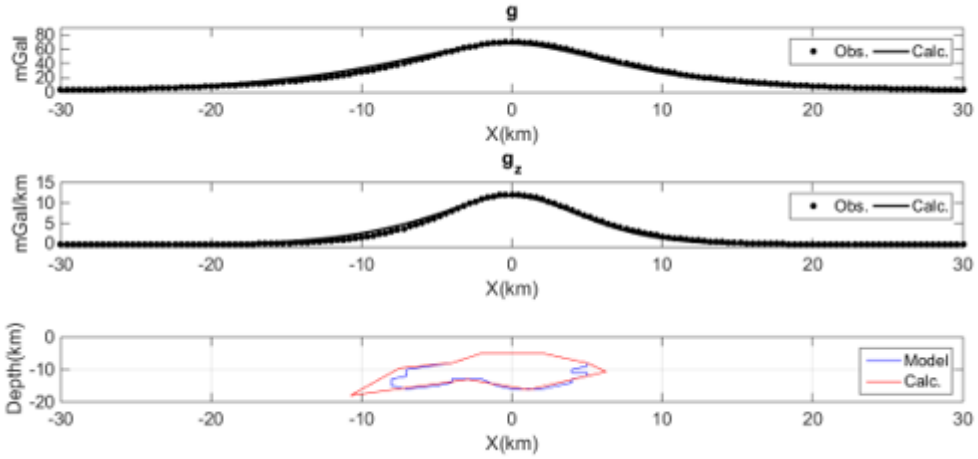

Figure 5.39 – Comparison between fields, first-order derivatives and between real model and calculated model for profile 7.

At the end, once obtained and interpreted the models from the 2.x D inversion, we can build density sections that constitute the starting model for a 3D inversion model.

5.2.5 3D inversion

According to (Ellis et al., 2013) we know that 3D inverse algorithm in Geosoft is represented by the equations that we will show in the next lines:

It is assumed that geophysical inverse problem is resolved with methods according to Tikhonov regularization (Tikhonov 1977). For the observed data $\boldsymbol{d_i^{obs}}, i = 1, N$, of a geophysical survey $\boldsymbol{G}$ on physical property model $\boldsymbol{m}$, we can write a simplified formulation of the geophysical problem:

$$Minimize\ \varphi_T[\boldsymbol{m}] = \varphi_D[\boldsymbol{m}] + \lambda\, \varphi_M[\boldsymbol{m}]\ with\ \lambda:\ \varphi_D = \varphi_D^* \tag{5.1}$$

$$\varphi_D[\boldsymbol{m}] = \sum_{i=1,N} \left(\frac{\boldsymbol{G_i}[\boldsymbol{m}] - \left(\boldsymbol{d_i^{obs}} - \boldsymbol{d_i^{trend}}\right)}{\delta \boldsymbol{d_i}} \right)^2 and\ \varphi_M[\boldsymbol{m}] = \boldsymbol{W}\left(\boldsymbol{m} - \boldsymbol{m^{ref}}\right) \tag{5.2}$$

where the equation (5.1) represents the minimization of the total objective function φ_T to find the model $\boldsymbol{m}$. The total objective function is the sum of the data objective function φ_D and the product between the regularization parameter λ and the model objective function, φ_M. The regularization parameter λ is used to maintain a suitable data misfit $\varphi_D = \varphi_D^*$.

The equation (5.2) represents the definitions of the data and model objective functions. We can choose it in different problems, depending on the auxiliary inputs (error assignment, trend removal, etc.).

To define the model objective function, it has chosen a least squares method misfit measure; $\boldsymbol{d_i^{trend}}$ is a possible trend that can be removed from the data, and $\delta \boldsymbol{d_i}$ is the error assigned to each data point.

The operator $\boldsymbol{W}$, contained in the model objective function φ_M, is applied to the difference between the inversion result, $\boldsymbol{m}$, and a reference model, $\boldsymbol{m^{ref}}$. $\boldsymbol{W}$ could be selected to be a simple L2 norm (smallest deviation models), or could include derivative operators (smooth models), or any other terms thought to be useful (focusing, depth weighting, etc.).

We now calculate a density model by a tool of Geosoft ®, VOXI. By VOXI we can take such 2.x D inverted sections and the mean density value for the body, which is 1 g/cm^3, as a starting

model. A least squares 3D inversion will lead us to form a final 3D density model (Figures 5.38 – 5.41).

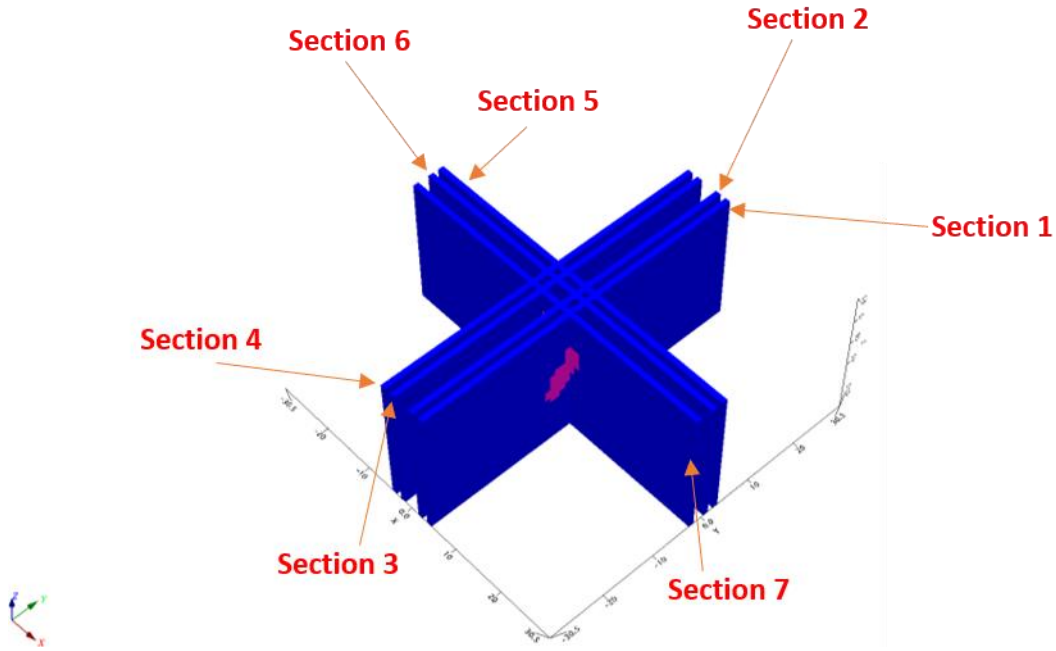

Figure 5.38 – The density sections calculated by inversion 2.x D MHODE are the starting model for the 3D inversion.

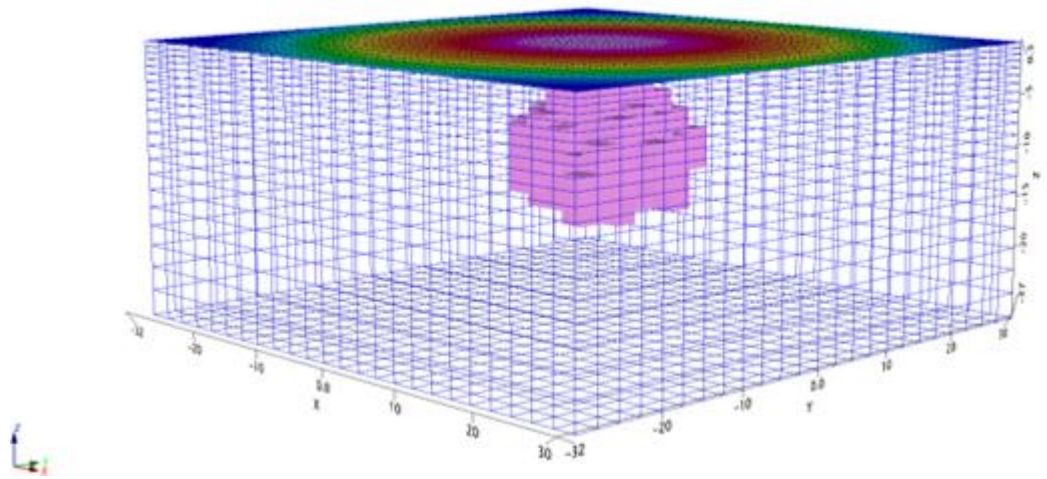

Figure 5.39 – The estimated 3D density model calculated by VOXI, a tool of Geosoft.

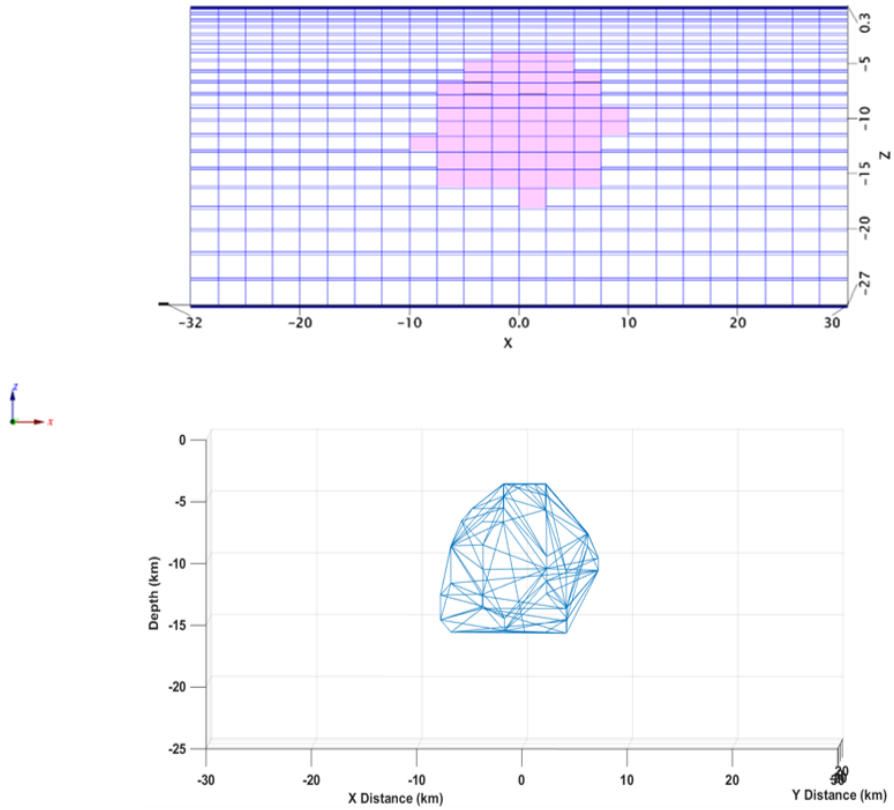

Figure 5.40 – Comparison along x direction between the 3D density model and the geometry model created by polyhedron at beginning of the synthetic case.

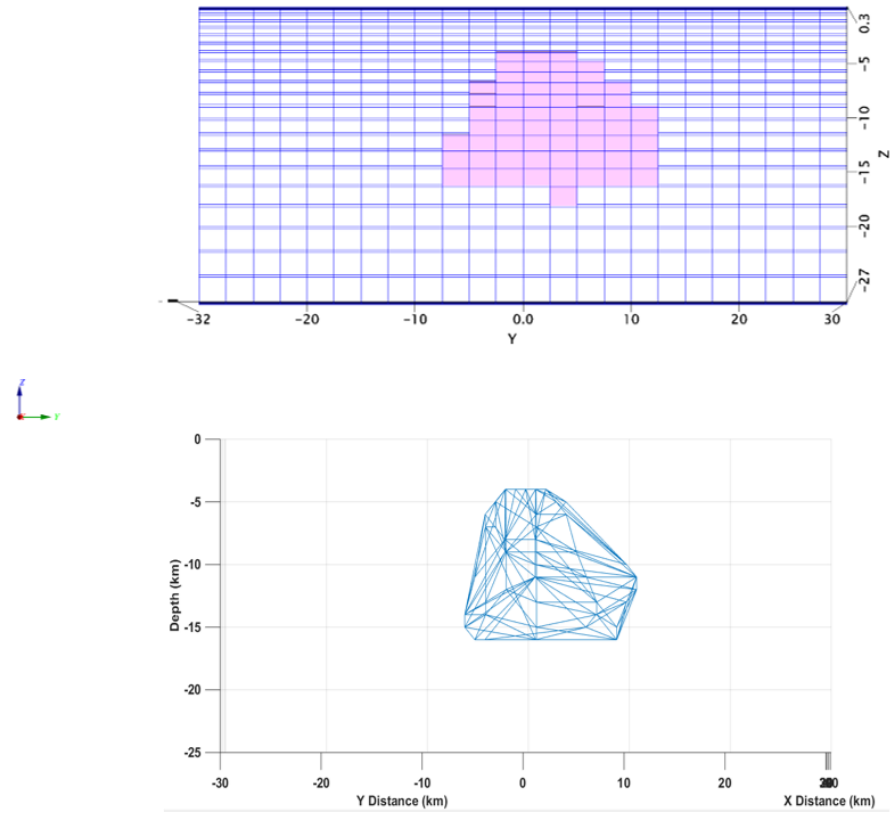

Figure 5.41 – Comparison along y direction between the real 3D density model and the geometry model created by polyhedron at beginning of the synthetic case.

CHAPTER 6. MHODE INVERSION (REAL CASE)

In this chapter we will discuss a real case. We will invert a dataset of gravity stations from the Nevada Test Site (USA) (Ponce, 1997). The data process that will take us to the definition of a 3D model of the Yucca Flat's basin consists in two phases: the first focus on the 2.x D inversion, where we will finally have the 2.x D density sections that will constitute the starting model for the 3d inversion. After this the phase two will start, and we will proceed to the 3D inversion in order to obtain the final 3D model of the basin.

6.1. Geology and gravity data of the survey area

The area where the survey of gravity data has been made concerns the NE corner of the Nevada Test Site, in the Basin and Range province: the Yucca Flat (Figure 6.1). Yucca Flat is a Tertiary alluvial basin that shows many characteristics typical of the Basin-and-Range structural and physiographic province in which it lies.

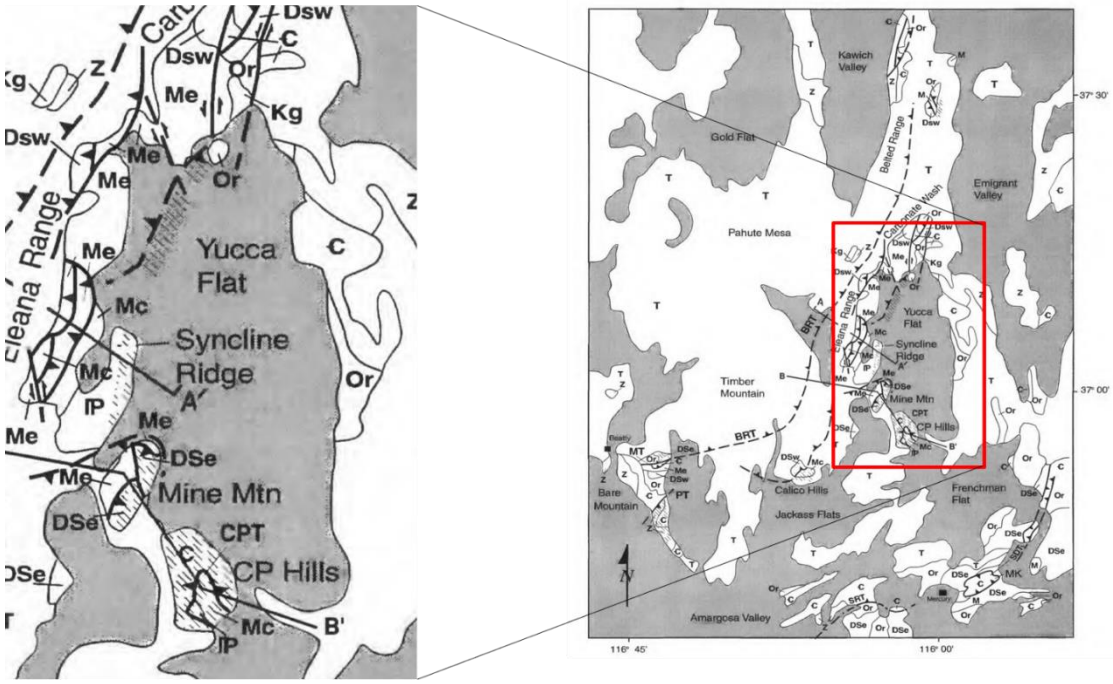

Figure 6.1 – Survey Area, Yucca Flat is situated in the North – East corner of the Nevada Test Site (modified from Cole et al., 1997).

The basin formed consequently to regional crustal extension, which was oriented generally East-West between about 9 Ma and the present. At the edges of the area the oldest rocks outcrop, which are upper Precambrian or paleozoic limestones, dolomites, quartzites, argillites, and siltstones, along with isolated late Mesozoic granodioritic intrusions. These rocks constitute what is the base, on which the volcanic rocks of the upper Miocene (mainly tuffs; e.g., Byers et al., 1976) and the quaternary clastic rocks (colluvial fans of the Tertiary and Quaternary sediments) were deposited (Figure 6.2).

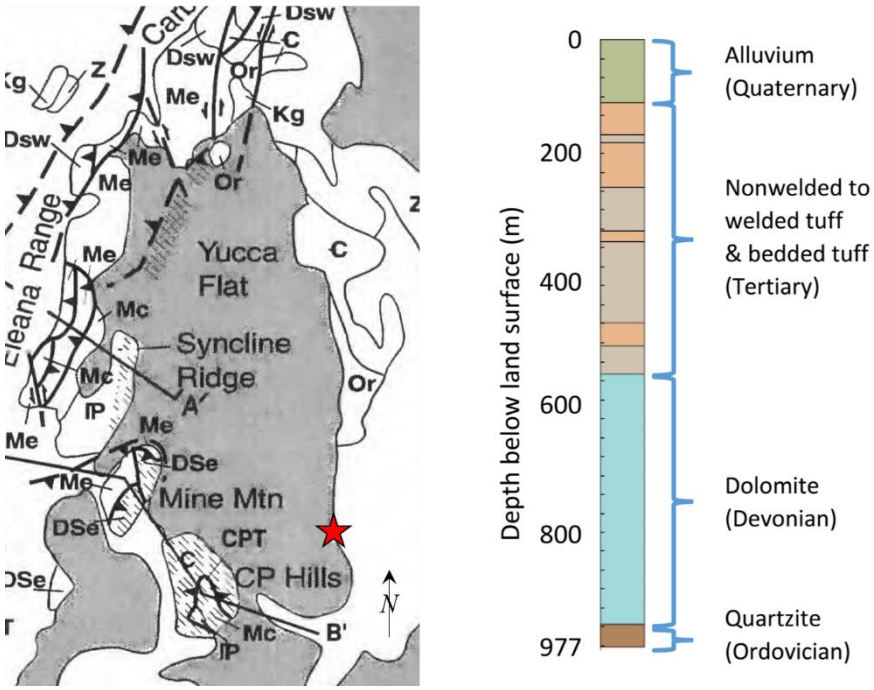

Figure 6.2 – In this figure is shown a representative well for the all area of Yucca Flat; modify from Florio (2020).

The information on the range of density of the rocks type in the Yucca Flat are shown in the Table 2:

Type of deposit	Range of density (g/cm^3)	Geology Period
Alluvium	1.9 – 2.1[A]	Quaternary
Nonwelded and welded tuffs	2.39 – 2.57[B]	Tertiary
Dolomite	2.51 – 2.72[C]	Devonian
Quartzite	2.6 – 2.8[A]	Ordovician

A = Snyder et al., 1983; B = Rautman et al., 1995; C = Ramspott et al., 1970.

Tectonically, the basin is dominated by NS trending normal faults such as the Carpetbag fault and the Yucca fault, formed by eastward extension and eastward dipping (Cole et al., 1997). The topography of the area between the North-Eastern and South-Western basin boundaries moderately slopes down with a difference of elevation of about 400 m (Figure 6.3).

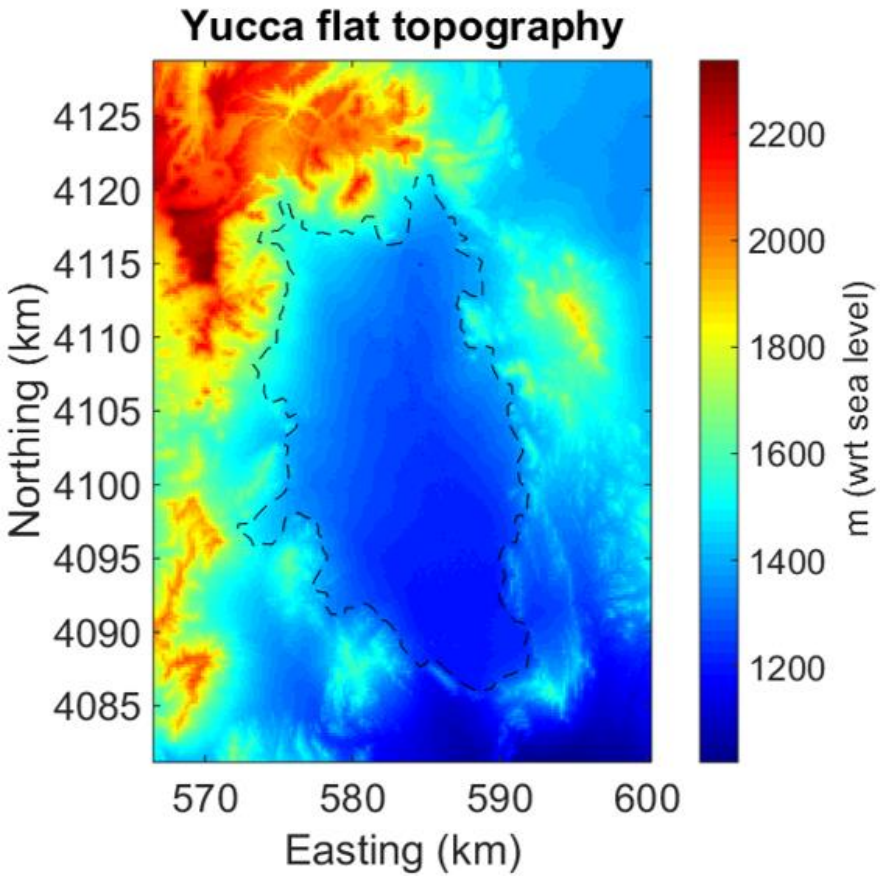

Figure 6.3 – Topography in the Yucca Flat Area.

Studies of the Yucca Flat are significant because this basin was one of four major sites of the underground nuclear-bomb test detonations on the Nevada Test Site since the late 1950's (U.S. Department of Energy, 1994; Laczniak and others, 1996) to 1995.

Although many of these test experiments were conducted in unsaturated rock above the water table, as many as 225 were detonated below the water table or sufficiently close that radioactive products were probably released directly into the ground water flow system (Laczniak and others, 1996). This aquifer system conveys substantial ground water from central Nevada toward the southwest in the Death Valley ground water flow system (Winograd and Thordarson, 1975; Dettinger, 1989). Thus, an understanding of the geologic framework of the carbonate aquifer is important to evaluating the potential consequences of contaminant migration in ground water.

So, the goal of researches in this zone is changed with the time, from the optimization of the depth of burial of the nuclear explosives (e.g., Healey, 1966), to find the optimal place for high-level nuclear waste storage (Healey et al., 1987), to support the modelling of the pathway of underground contaminants by constraining the basin configuration and identifying faults and other possible water conduits or barriers (Phelps et al., 1999).

Gravity data were taken from an existing dataset of gravity stations from the Nevada Test Site (Ponce, 1997). The total of stations in the basin are 642. Gravity data were reduced to complete Bouguer gravity anomalies (Plouff, 1977) with a reduction density of 2670 kg/m^3 by applying earth-tide, instrument drift, free-air, Bouguer, latitude, curvature, and terrain corrections. An isostatic correction, following the method and parameters used by Jachens and Griscom (1985), was applied to produce the final isostatic gravity anomaly. Assuming a sea level crustal thickness of 25 km based on seismic profiles, a crustal density above sea level of 2670 kg/m^3, and a mantle-crust density contrast of 400 kg/m^3, the correction removed the long-wavelength gravitational effect caused by isostatic compensation of topography (Phelps 2002).

The dataset of isostatic residual gravity anomaly (Figure 6.4) of the investigated area was used as the main data to model the contact between dense pre-Cenozoic rocks and less dense overlying Tertiary and Quaternary deposits.

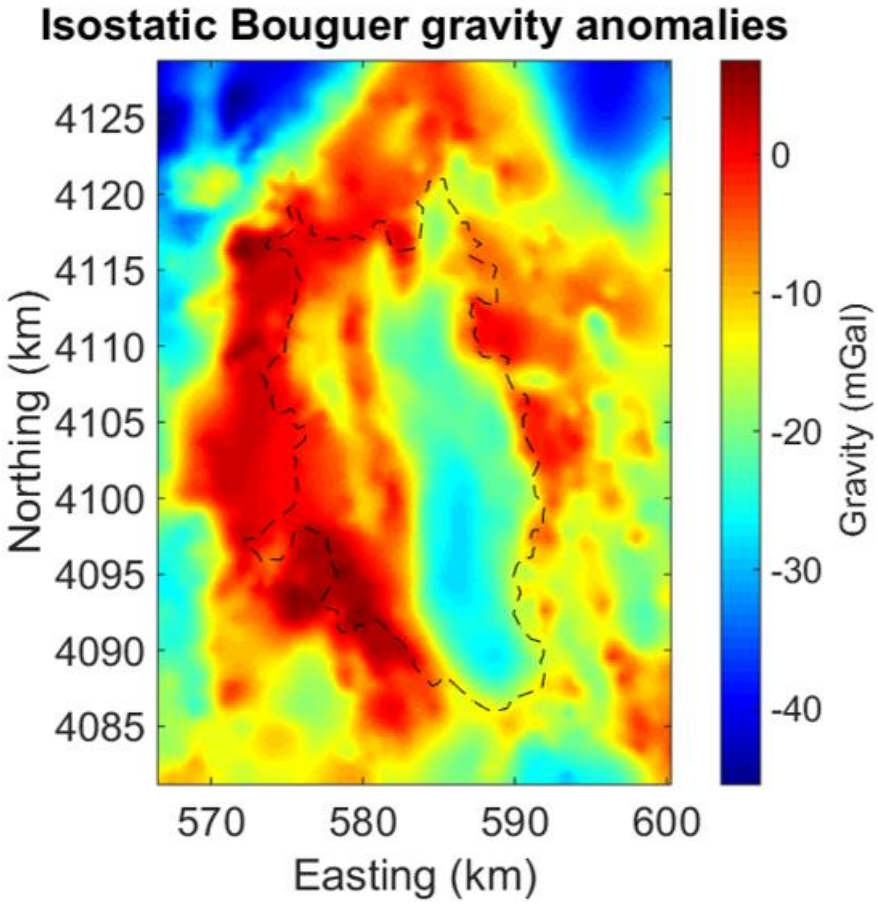

Figure 6.4 - Isostatic Bouguer gravity anomalies of the investigated area.

The negative gravity anomaly over Yucca Flat basin reaches –28 mGal, where the basin is known to be about 1.5 km deep (Phelps & Graham, 2002). The anomaly reaches its minimum in the Eastern area of the basin (in the figure the basin is represented with a black dotted line), and it presents an elongated maximum in the Western part of the basin. The anomaly approaches to zero along the boundaries of the Yucca Flat in all directions except for the Southern direction.

From the isostatic residual gravity anomaly map, we calculated numerically the vertical gradient of the gravity map (Figure 6.5). We will focus on this ahead, as we will use it for the 2.x D inversion.

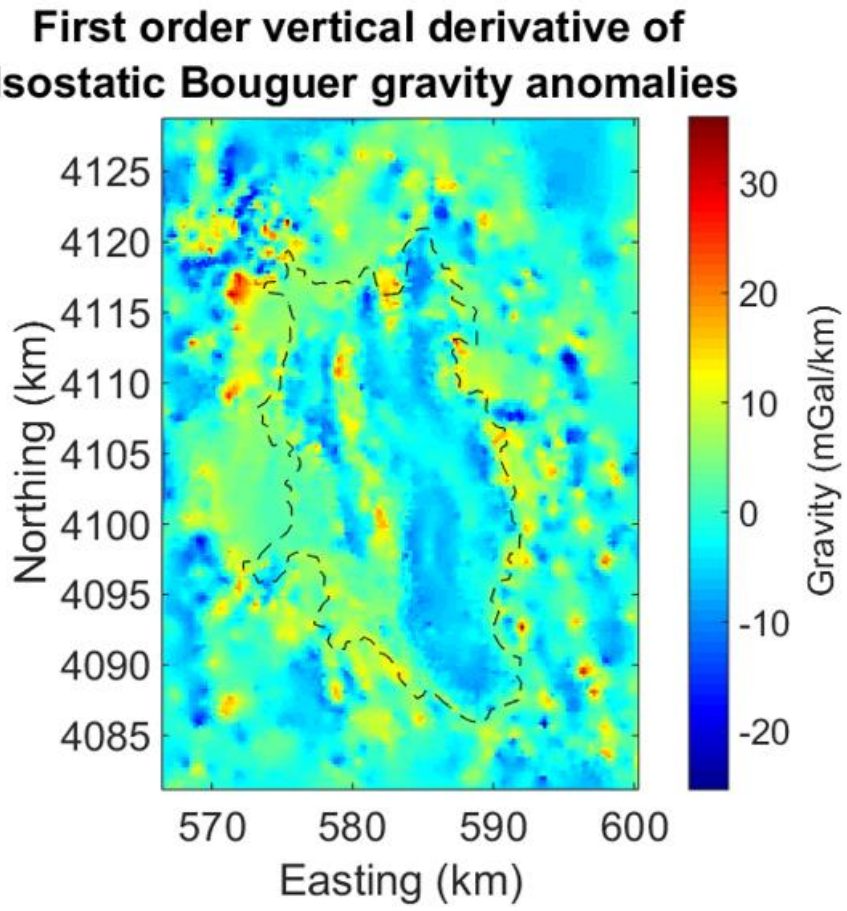

Figure 6.5 – First order vertical derivative of Isostatic Bouguer gravity anomalies of the investigated area.

6.2 2.x D inversion of the gravity data in Yucca Flat

The first phase of data processing is the 2.x D inversion of the gravity data. This phase is characterized by 5 steps:

- Extraction of the profiles from the gravity map
- Multiridge analysis of the profiles extracted
- VFSA inversion of the scaling functions observed and calculated of the ridges obtained
- Calculation of the geometry, the sides and the bottom, of the source
- Estimation of the density of the model inverted

As we said before, the observation of this anomaly allows us to assume in the interpretation phase that the gravity data can be interpreted with the contact surface between a pre-Cenozoic basement and a Tertiary and Quaternary basin.

The first step of the 2.x D inversion with MHODE method consists in the extraction of eight parallel profiles, oriented West – East, that pass on the minimum anomaly, (Figures 6.6 and 6.7). To calculate the field and its derivative, we assume that the investigated source has a finite strike length (North – South), with a length of 28 km. As a consequence, the northernmost point of the strike length has a coordinate of 4116.3N km and the southernmost point has a coordinate of 4088.3N km.

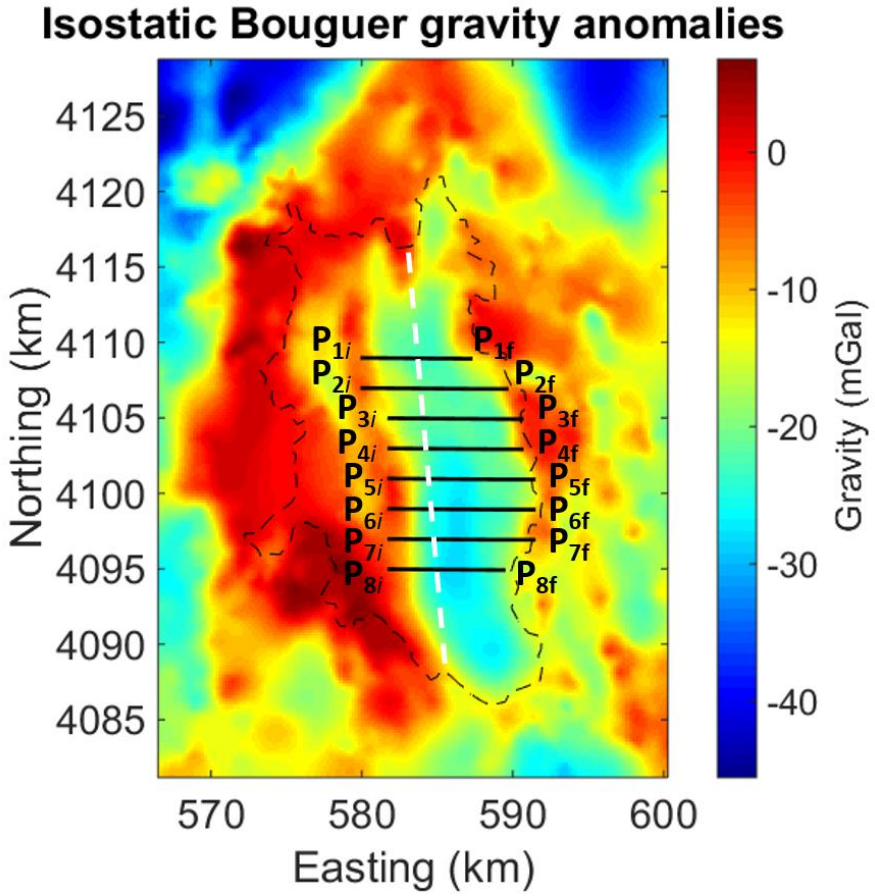

Figure 6.6 - Representation of the 8 parallel profiles West-East on the gravity field map of the Yucca Flat. The white dotted line represents the finite strike length.

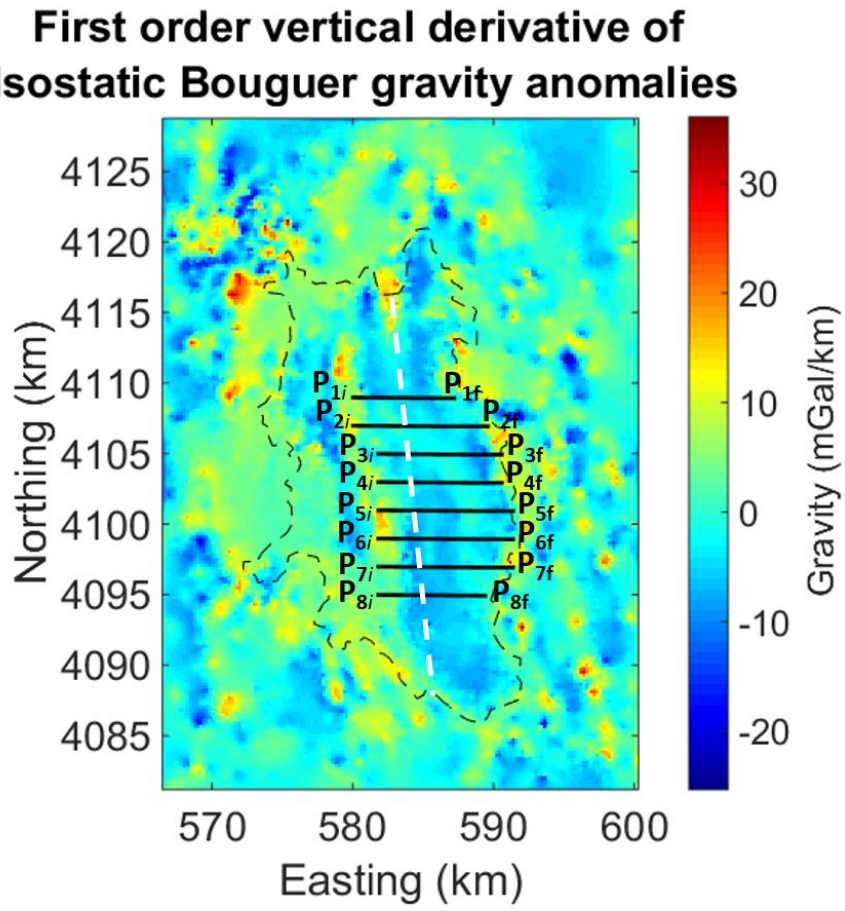

Figure 6.7 - Representation of the 8 parallel profiles West-East on the gravity gradient map of the Yucca Flat, the white dotted line represents the finite strike length.

The information on the localization of the profiles is contained in the Table 3:

Name of the profile	Initial position *xi* (km)	Final position *xf* (km)	Strike position *y* (km)
Profile 1	580	587.2	4109
Profile 2	580	589.6	4107
Profile 3	581.8	590.6	4105
Profile 4	581.8	590.6	4103
Profile 5	581.8	591.4	4101
Profile 6	581.8	591.4	4099
Profile 7	581.8	591.4	4097
Profile 8	581.8	589.4	4095

The figures (6.8 – 6.15) show the gravity field and its derivative for all eight profiles, separated with a step of 2 km along the strike direction from North to South.

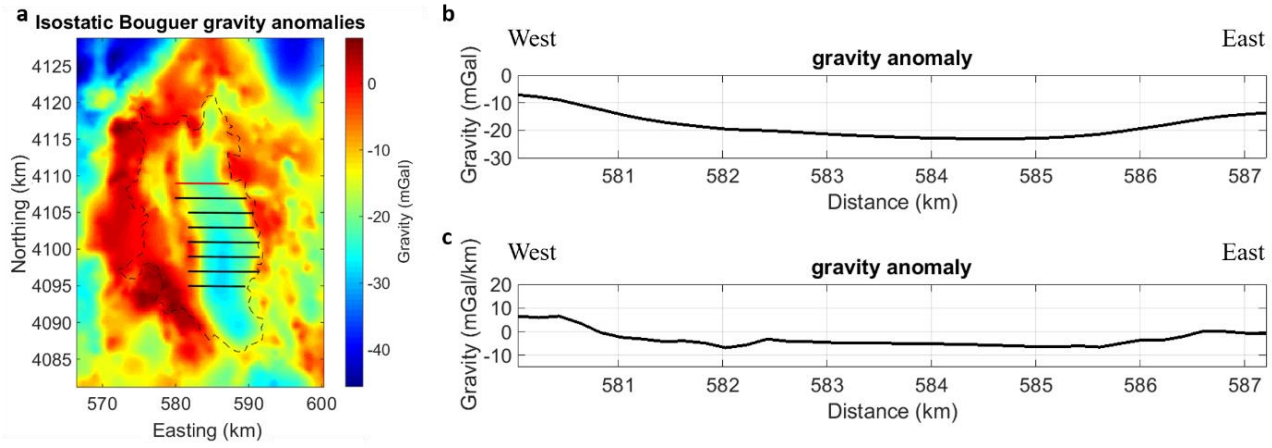

Figure 6.8 - a: Track of profile 1 on the gravity map (red solid line); b: gravity field along profile 1; c: first order vertical derivative of the gravity field along profile 1.

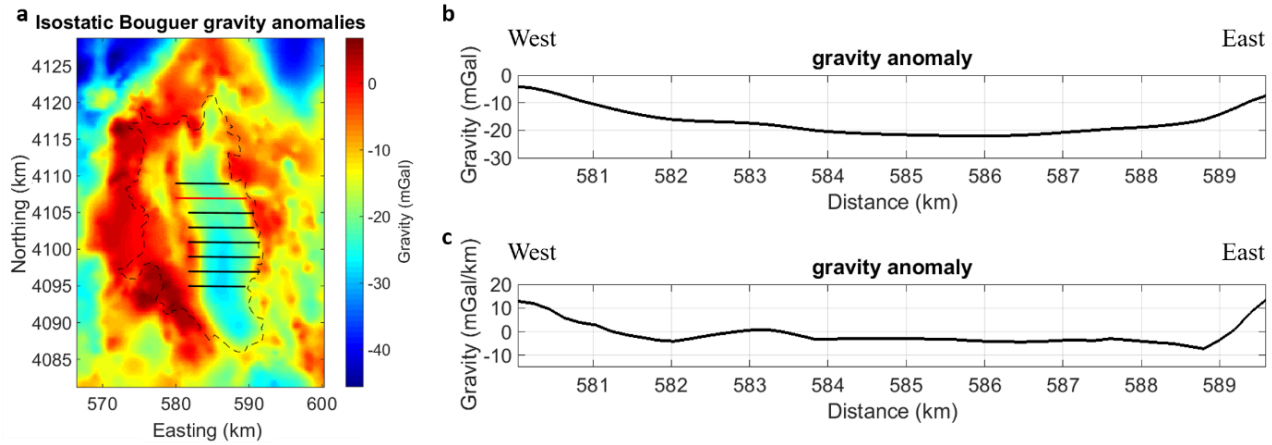

Figure 6.9 - a: Track of profile 2 on the gravity map (red solid line); b: gravity field along profile 1; c: first order vertical derivative of the gravity field along profile 2.

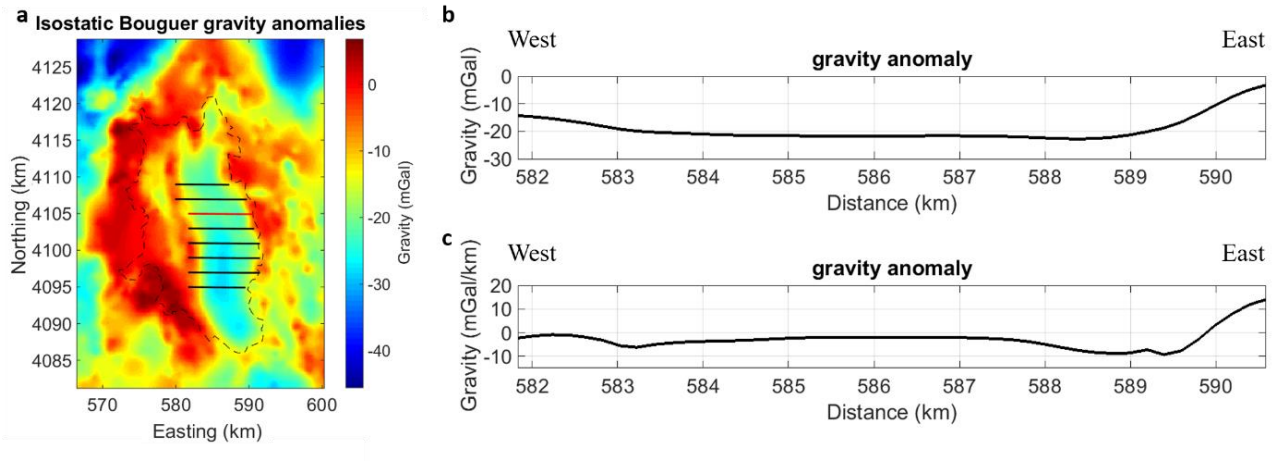

Figure 6.10 - a: Track of profile 3 on the gravity map (red solid line); b: gravity field along profile 1; c: first order vertical derivative of the gravity field along profile 3.

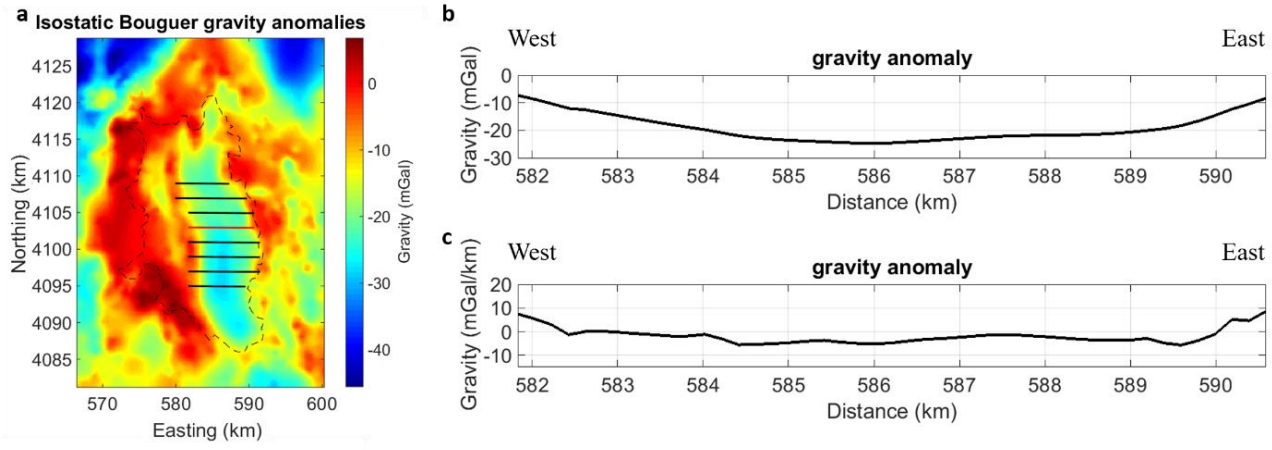

Figure 6.11 - a: Track of profile 4 on the gravity map (red solid line); b: gravity field along profile 1; c: first order vertical derivative of the gravity field along profile 4.

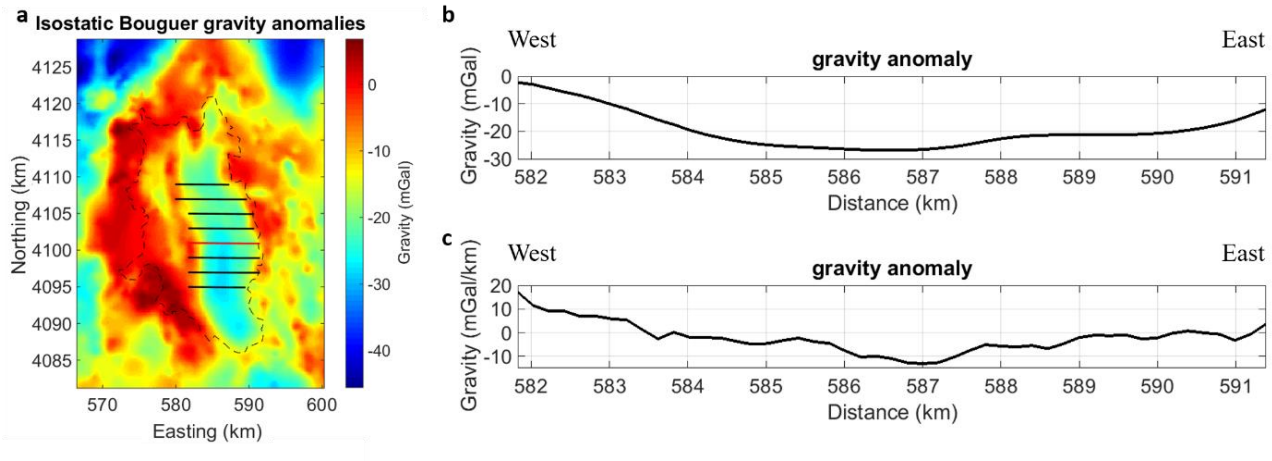

Figure 6.12 - a: Track of profile 5 on the gravity map (red solid line); b: gravity field along profile 1; c: first order vertical derivative of the gravity field along profile 5.

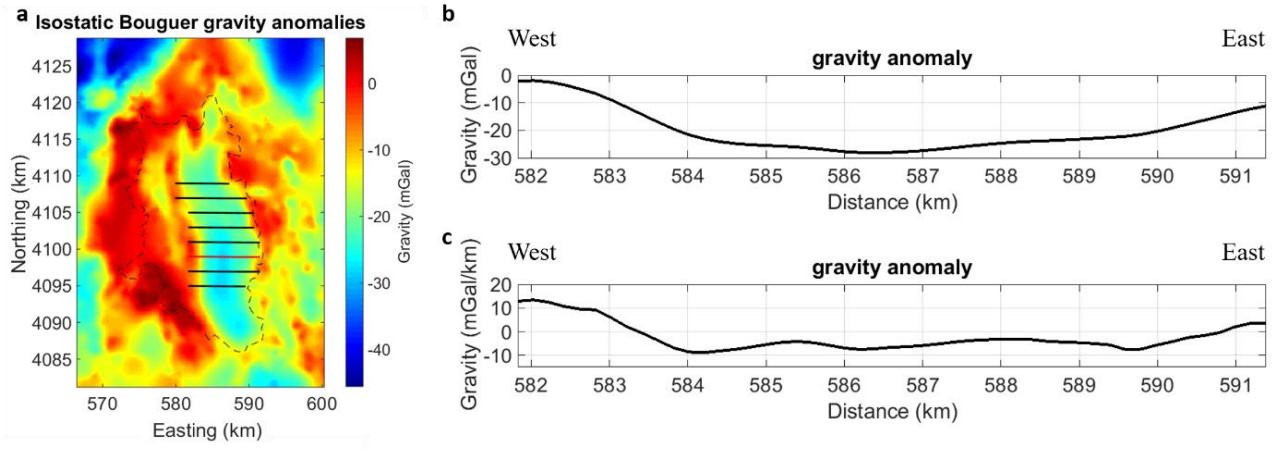

Figure 6.13 - a: Track of profile 6 on the gravity map (red solid line); b: gravity field along profile 1; c: first order vertical derivative of the gravity field along profile 6.

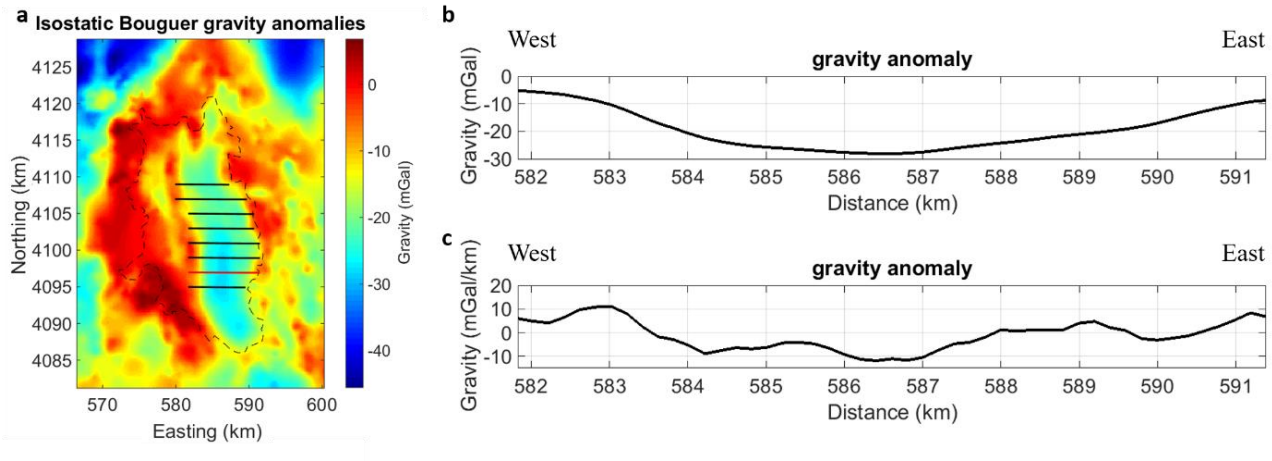

Figure 6.14 - a: Track of profile 7 on the gravity map (red solid line); b: gravity field along profile 1; c: first order vertical derivative of the gravity field along profile 7.

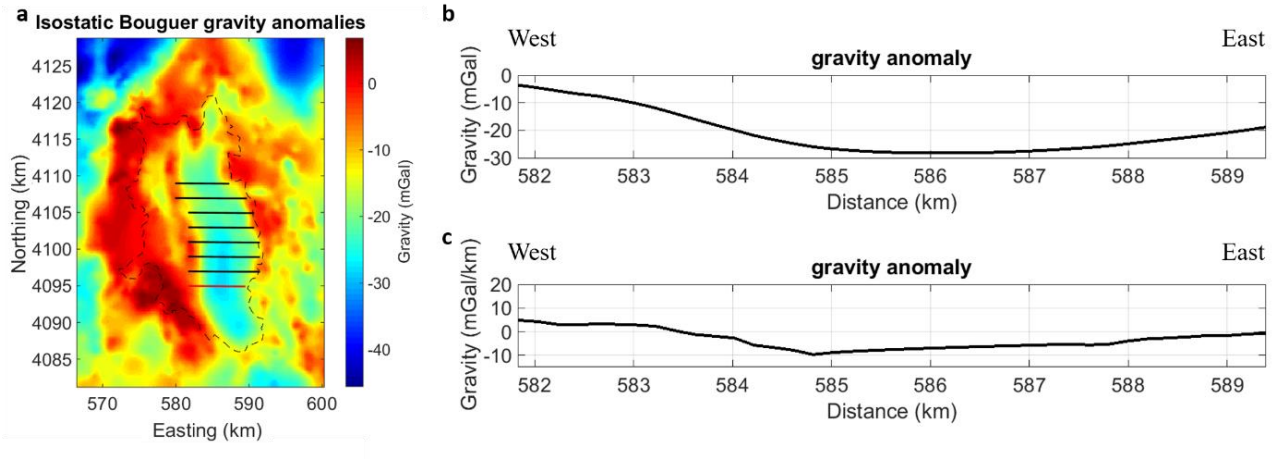

Figure 6.15 - a: Track of profile 8 on the gravity map (red solid line); b: gravity field along profile 1; c: first order vertical derivative of the gravity field along profile 8.

For all the eight profiles, we performed the multiridge analysis (Figures 6.16 – 6.23) by upward continuing the gravity field up to 1.5 km altitude and the first order vertical derivative of the gravity field up to 5 km altitude.

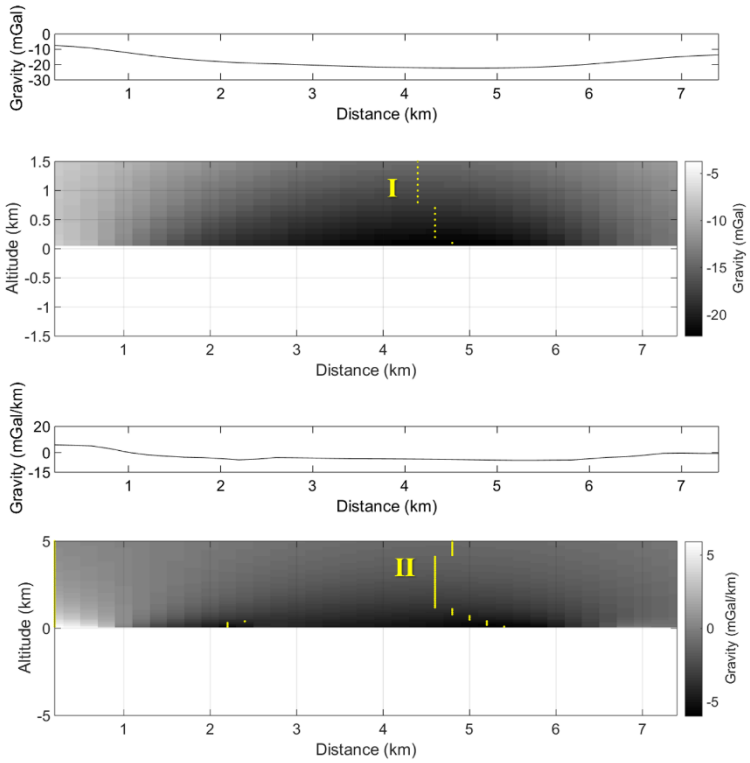

Figure 6.16 – gravity field along profile 1 (a) ridge along the profile (b, yellow dots) superposed to the upward continued field; first order vertical derivative of the gravity field along profile 1 (c) and ridge along the profile (d, yellow dots) superposed to the upward continued field.

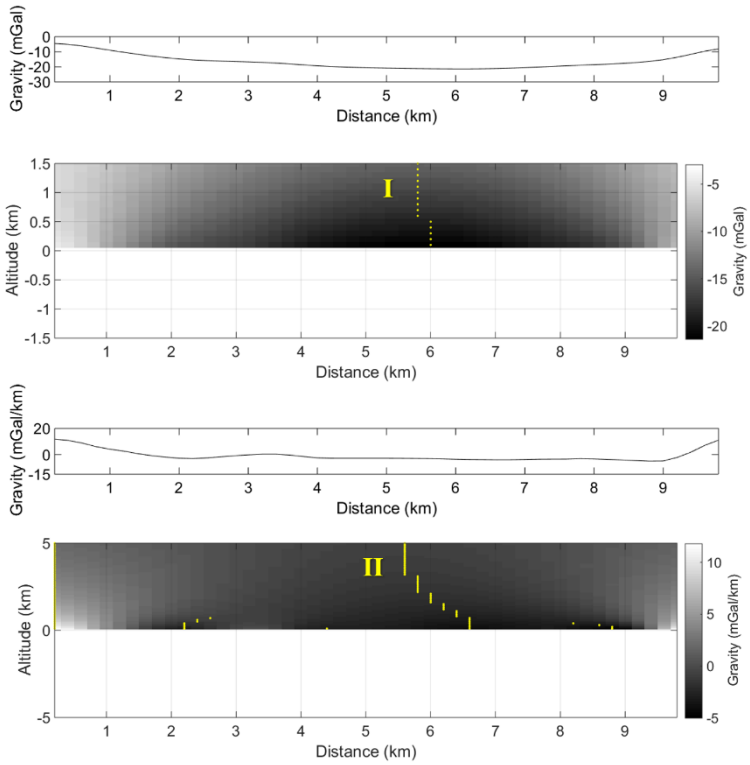

Figure 6.17 – gravity field along profile 2 (a) ridge along the profile (b, yellow dots) superposed to the upward continued field; first order vertical derivative of the gravity field along profile 2 (c) and ridge along the profile (d, yellow dots) superposed to the upward continued field.

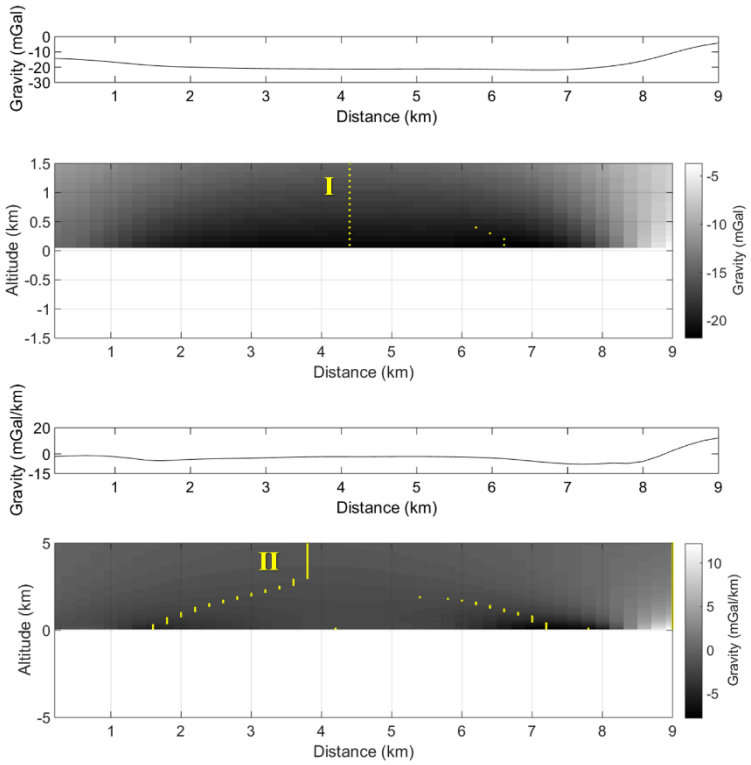

Figure 6.18 – gravity field along profile 3 (a) ridge along the profile (b, yellow dots) superposed to the upward continued field; first order vertical derivative of the gravity field along profile 3 (c) and ridge along the profile (d, yellow dots) superposed to the upward continued field.

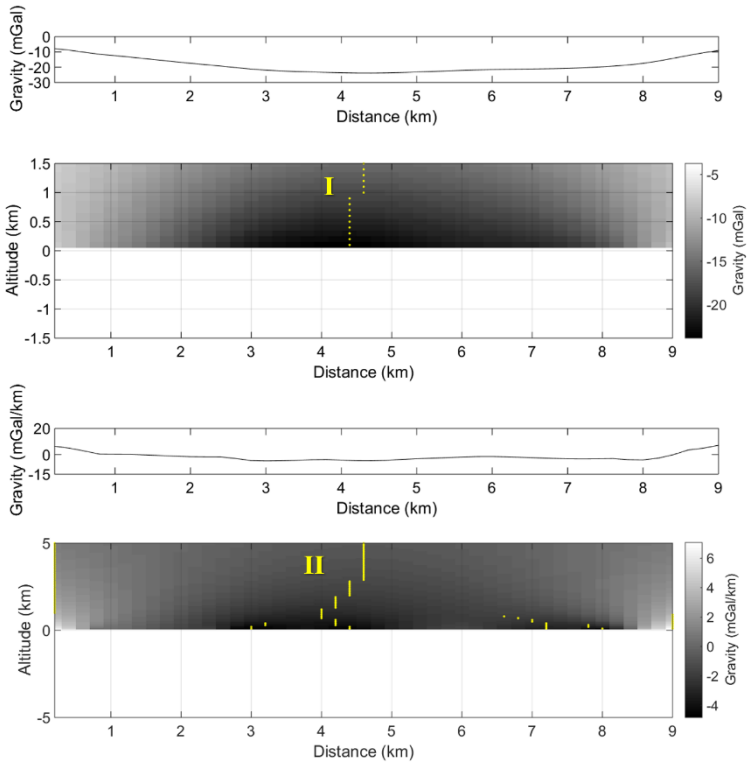

Figure 6.19 – gravity field along profile 4 (a) ridge along the profile (b, yellow dots) superposed to the upward continued field; first order vertical derivative of the gravity field along profile 4 (c) and ridge along the profile (d, yellow dots) superposed to the upward continued field.

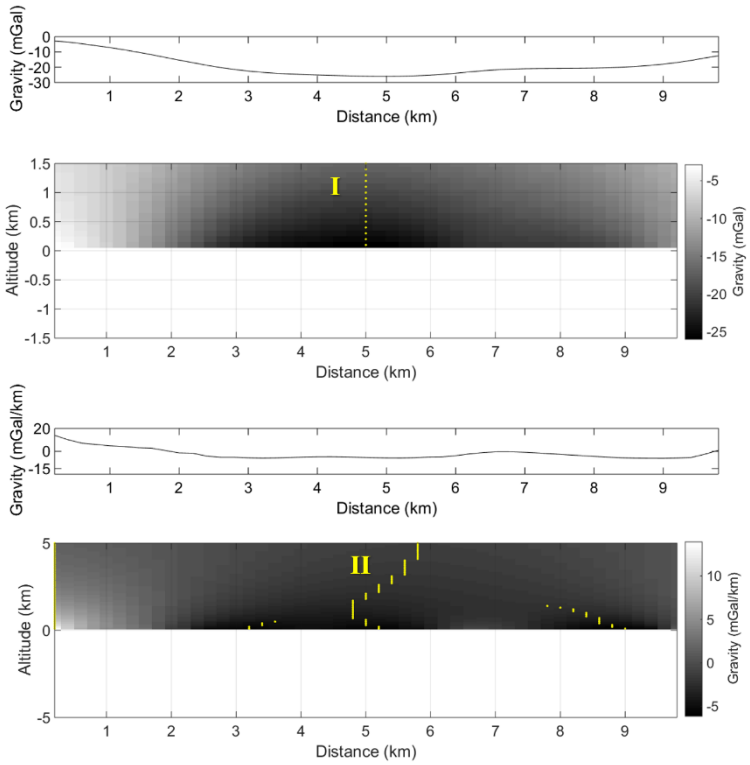

Figure 6.20 – gravity field along profile 5 (a) ridge along the profile (b, yellow dots) superposed to the upward continued field; first order vertical derivative of the gravity field along profile 5 (c) and ridge along the profile (d, yellow dots) superposed to the upward continued field.

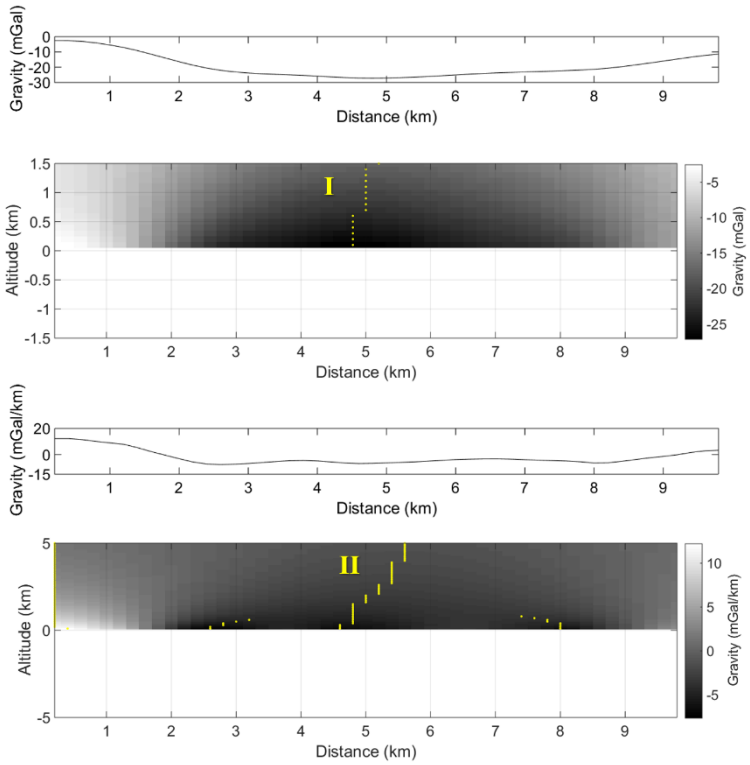

Figure 6.21 – gravity field along profile 6 (a) ridge along the profile (b, yellow dots) superposed to the upward continued field; first order vertical derivative of the gravity field along profile 6 (c) and ridge along the profile (d, yellow dots) superposed to the upward continued field.

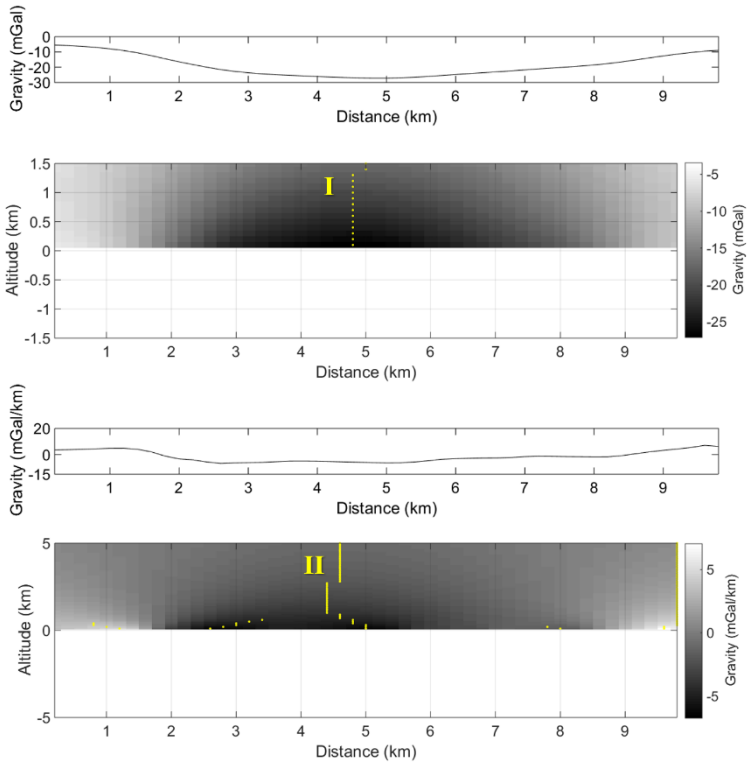

Figure 6.22 – gravity field along profile 7 (a) ridge along the profile (b, yellow dots) superposed to the upward continued field; first order vertical derivative of the gravity field along profile 7 (c) and ridge along the profile (d, yellow dots) superposed to the upward continued field.

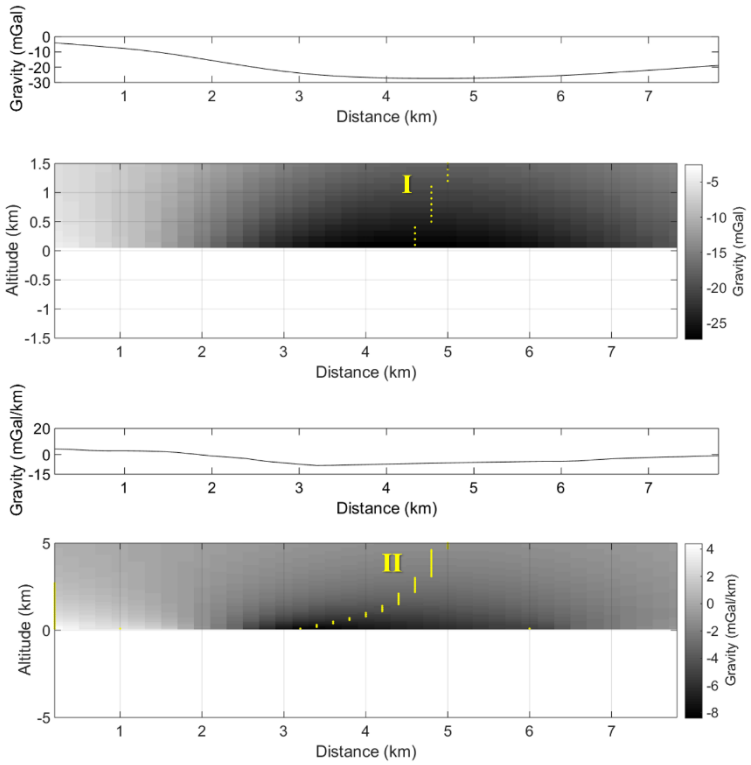

Figure 6.23 – gravity field along profile 8 (a) ridge along the profile (b, yellow dots) superposed to the upward continued field; first order vertical derivative of the gravity field along profile 8 (c) and ridge along the profile (d, yellow dots) superposed to the upward continued field.

We have then used the VFSA inversion algorithm to calculate the best model with the minimal misfit error between the observed scaling function and the scaling function of the calculated model (Figure 6.24).

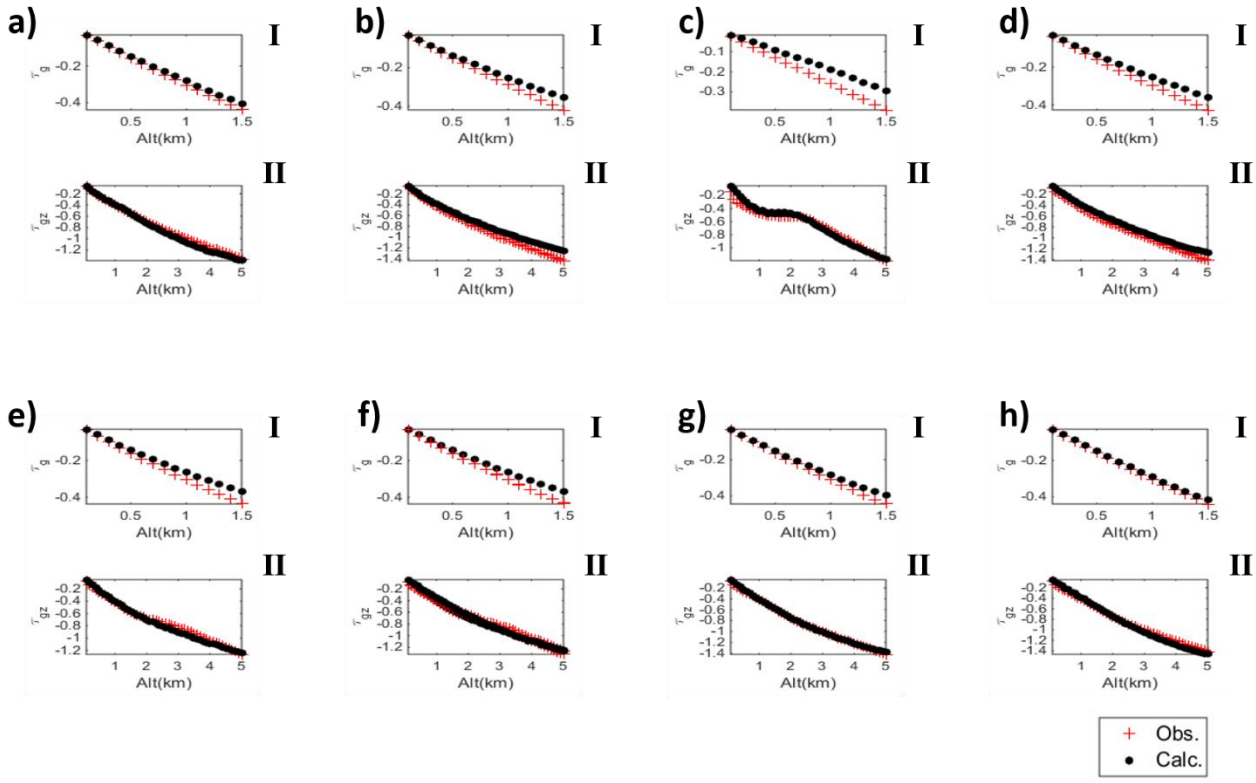

Figure 6.24 – Comparison between the observed and calculated scaling functions. a): Scaling functions of the profile 1; b): Scaling functions of the profile 2; c): Scaling functions of the profile 3; d): Scaling functions of the profile 4; e): Scaling functions of the profile 5; f): Scaling functions of the profile 6; g): Scaling functions of the profile 7; h): Scaling functions of the profile 8;

For each model obtained through the VFSA inversion, the density values are estimated by the slope of the straight line that fits the points in a scatter plot between the observed gravity field and calculated gravity field with unitary density. (Figure 6.25).

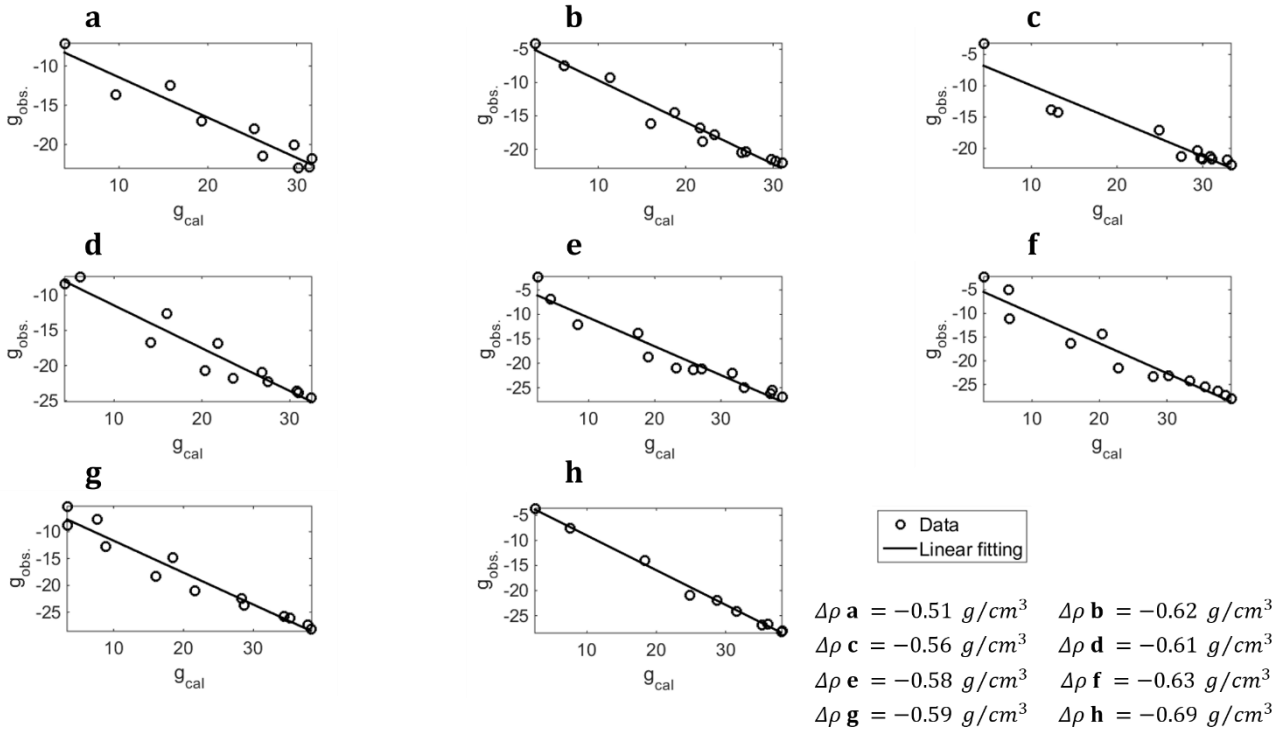

Figure 6.25 – Estimated density by MHODE method, the density values are estimated by the slope of the straight line that fits the points in each scatter plot between the observed gravity field and calculated gravity field with unitary density. a) scatterplot between the fields for profile 1; b) scatterplot between the fields for profile 2; c) scatterplot between the fields for profile 3; d) scatterplot between the fields for profile 4; e) scatterplot between the fields for profile 5; f) scatterplot between the fields for profile 6; g) scatterplot between the fields for profile 7; h) scatterplot between the fields for profile 8.

From the figure above, we may observe a substantial agreement of the estimated density for all the sections. Differences could depend on the 2.x D assumption (mentioned in the paragraph 5.2.3), because in the 2.x D case we are assuming that the modelled section does not vary along the strike direction. Obviously, for real data, differences may also be effective, reflecting the real distribution of the density. In any case, as for the synthetic case, we remind all the evaluations to the final 3D model.

Finally, we show in the following figures (6.26 – 6.33) the 2.x D models obtained with the respective density contrasts, and the comparison between the calculated field and its 1st order derivative vs. the observed field and 1st order derivative. In 2.x D model the position of each vertex along x coordinate and z coordinate, obtained with the inversion of the scaling functions by the

VFSA algorithm, constitutes the 2.x D model inverted that represents the limit of the sides and the bottom of the source processed.

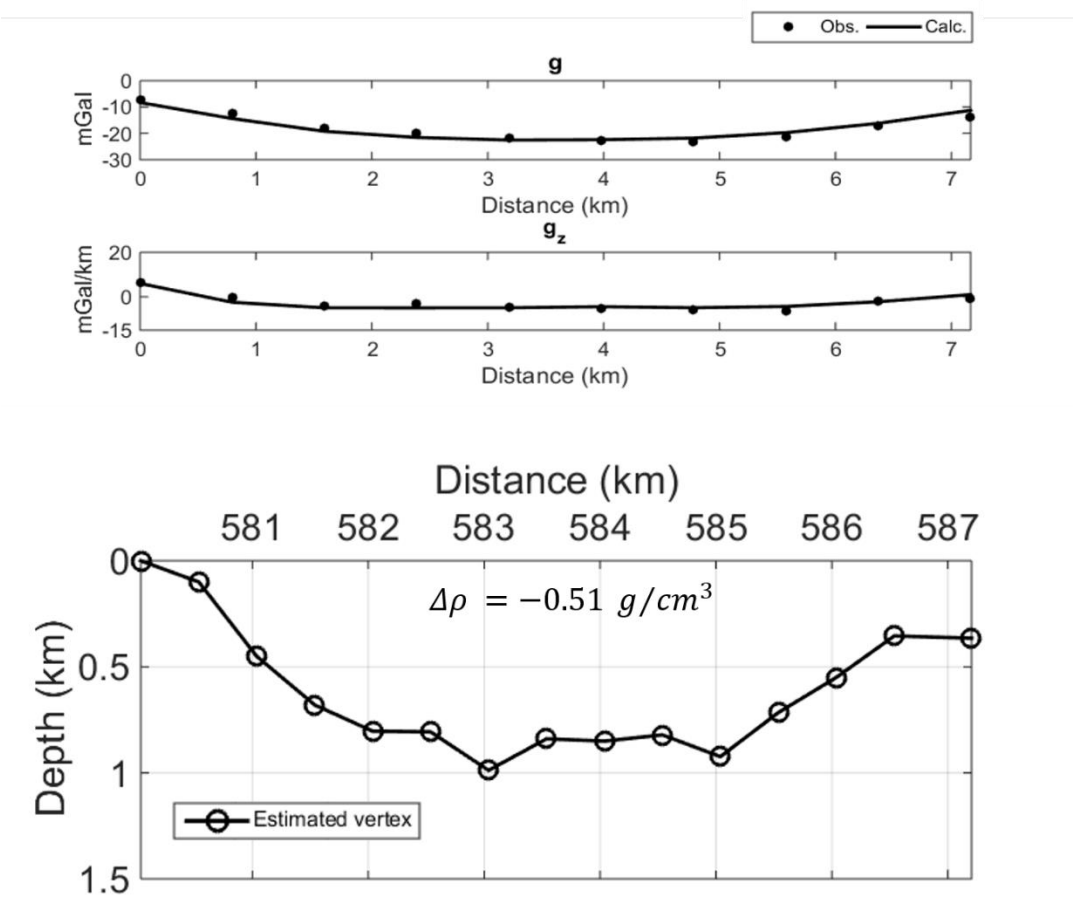

Figure 6.26 – Estimated model for profile 1. Top: observed (solid line) and calculated gravity field (dot); middle: observed (solid line) and calculated (dot) first order vertical derivative: Bottom: 2.x D inverted model: black circles indicate the vertices free to move along the depth.

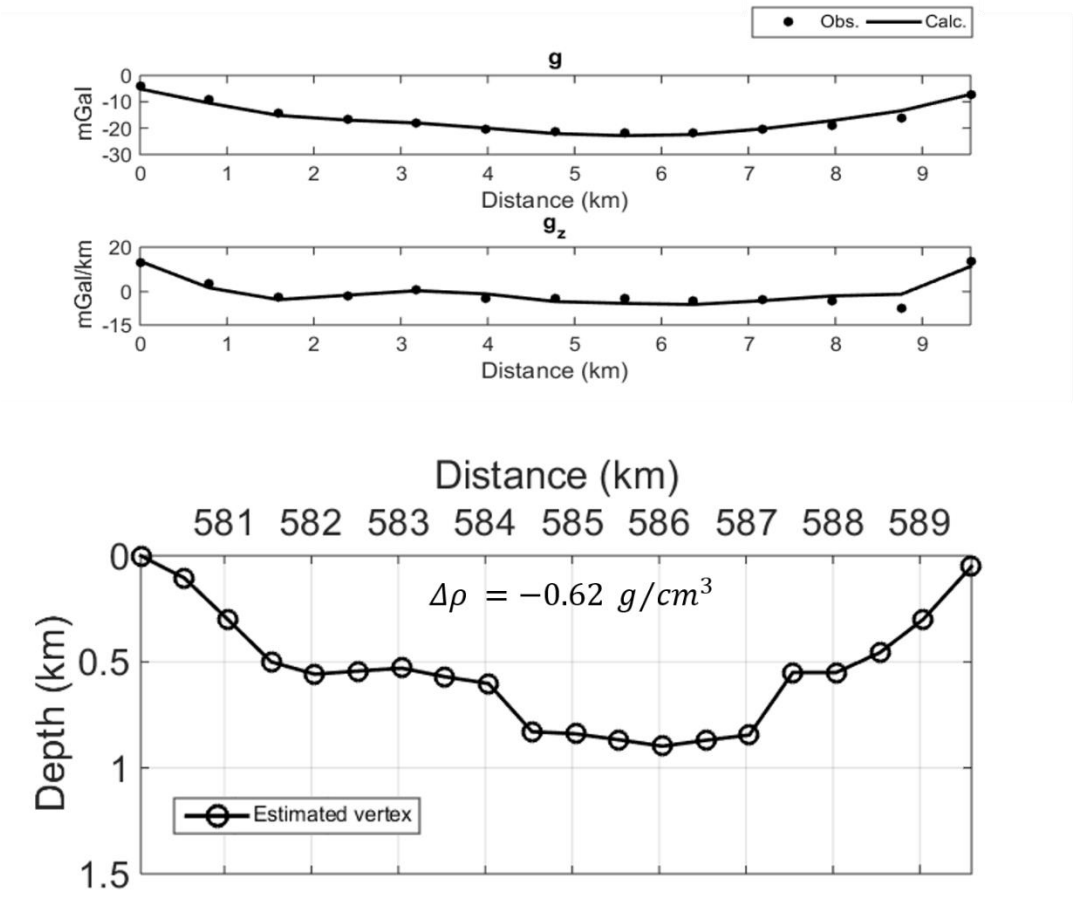

Figure 6.27 – Estimated model for profile 2. Top: observed (solid line) and calculated gravity field (dot); middle: observed (solid line) and calculated (dot) first order vertical derivative: Bottom: 2.x D inverted model: black circles indicate the vertices free to move along the depth.

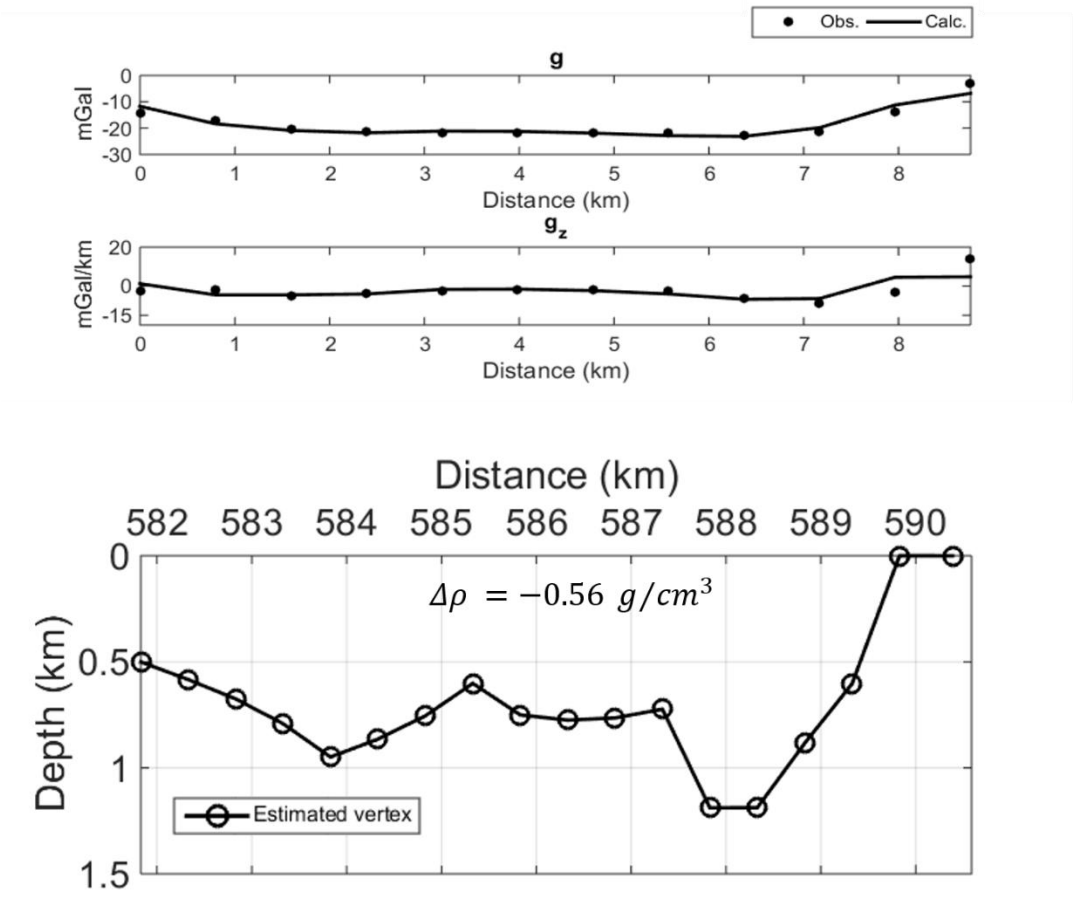

Figure 6.28 – Estimated model for profile 3. Top: observed (solid line) and calculated gravity field (dot); middle: observed (solid line) and calculated (dot) first order vertical derivative: Bottom: 2.x D inverted model: black circles indicate the vertices free to move along the depth.

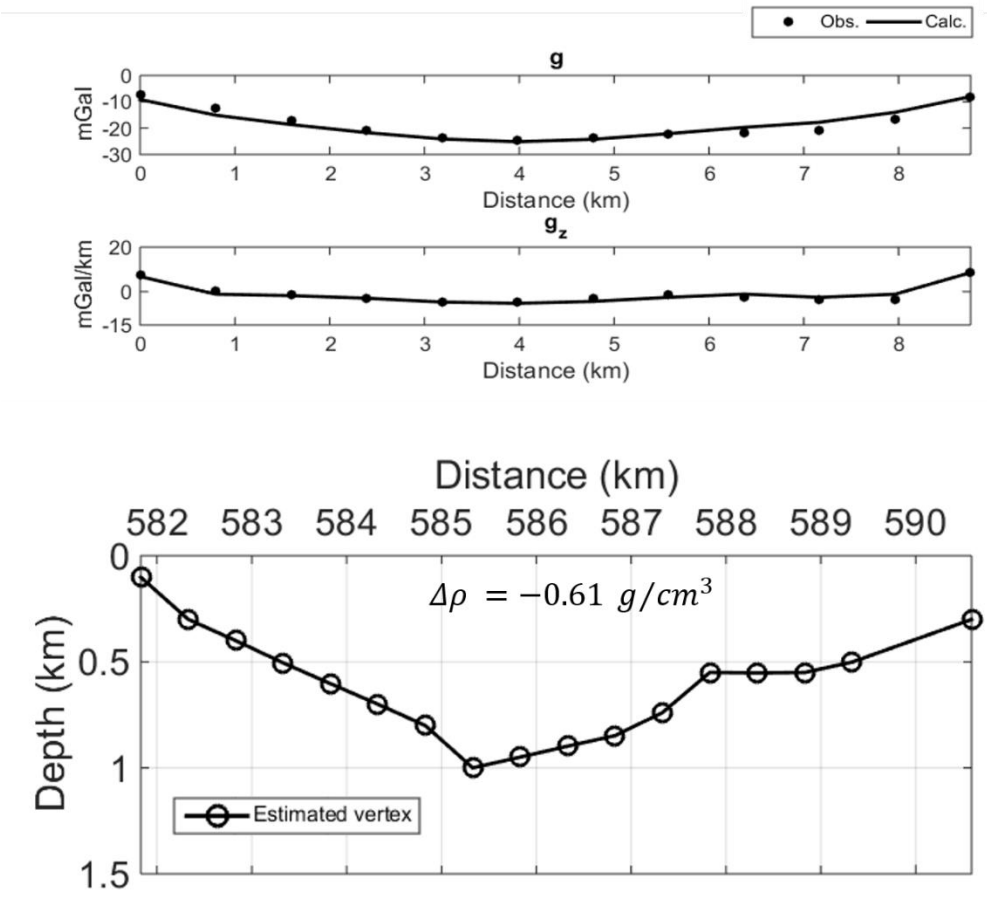

Figure 6.29 – Estimated model for profile 4. Top: observed (solid line) and calculated gravity field (dot); middle: observed (solid line) and calculated (dot) first order vertical derivative: Bottom: 2.x D inverted model: black circles indicate the vertices free to move along the depth.

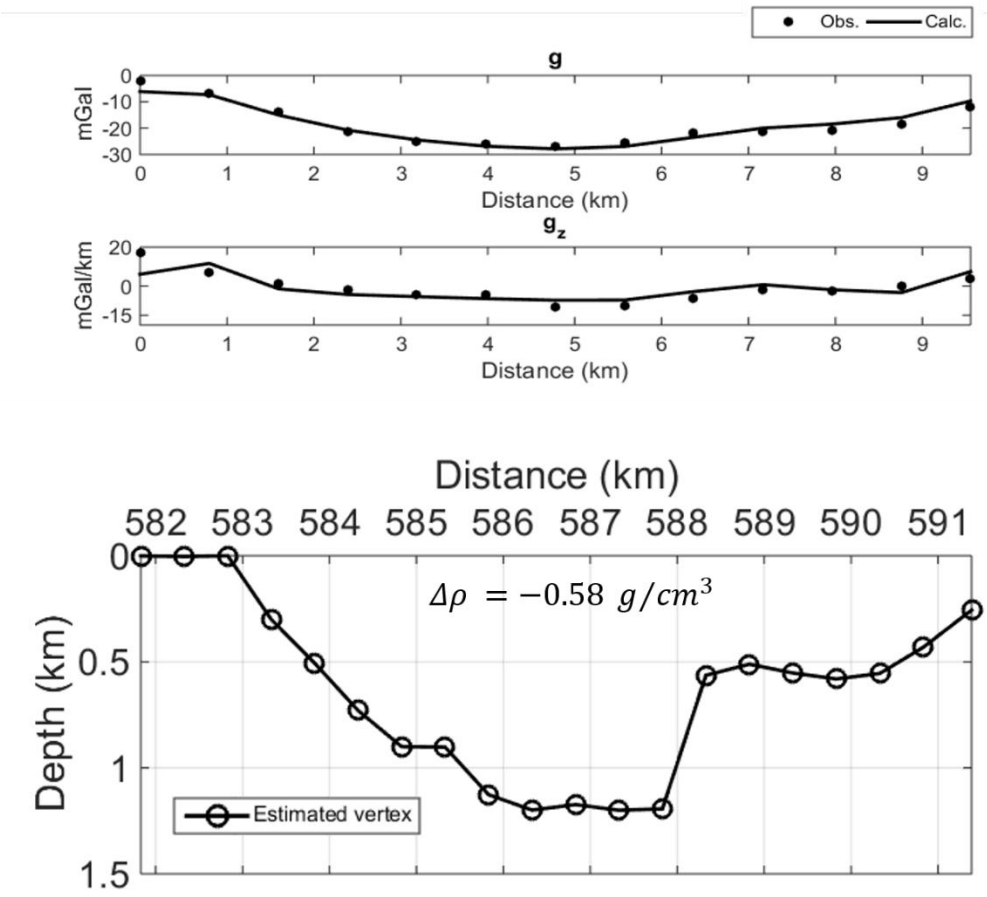

Figure 6.30 – Estimated model for profile 5. Top: observed (solid line) and calculated gravity field (dot); middle: observed (solid line) and calculated (dot) first order vertical derivative: Bottom: 2.x D inverted model: black circles indicate the vertices free to move along the depth.

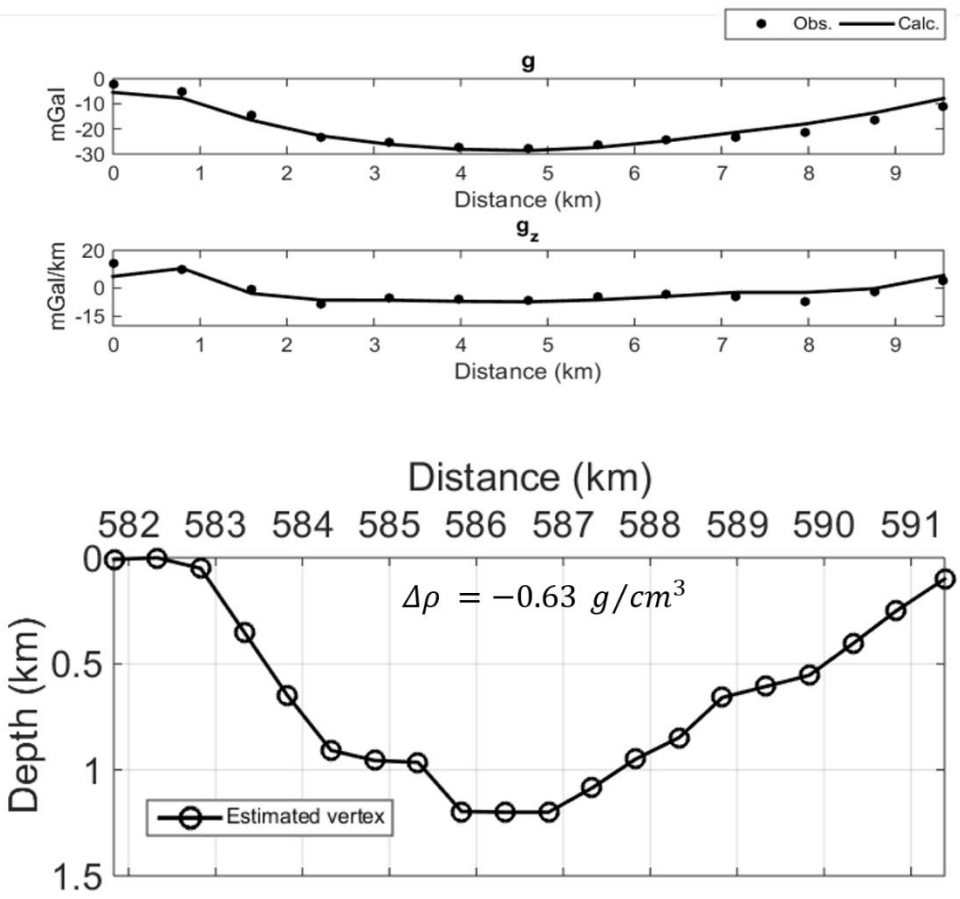

Figure 6.31 – Estimated model for profile 6. Top: observed (solid line) and calculated gravity field (dot); middle: observed (solid line) and calculated (dot) first order vertical derivative: Bottom: 2.x D inverted model: black circles indicate the vertices free to move along the depth.

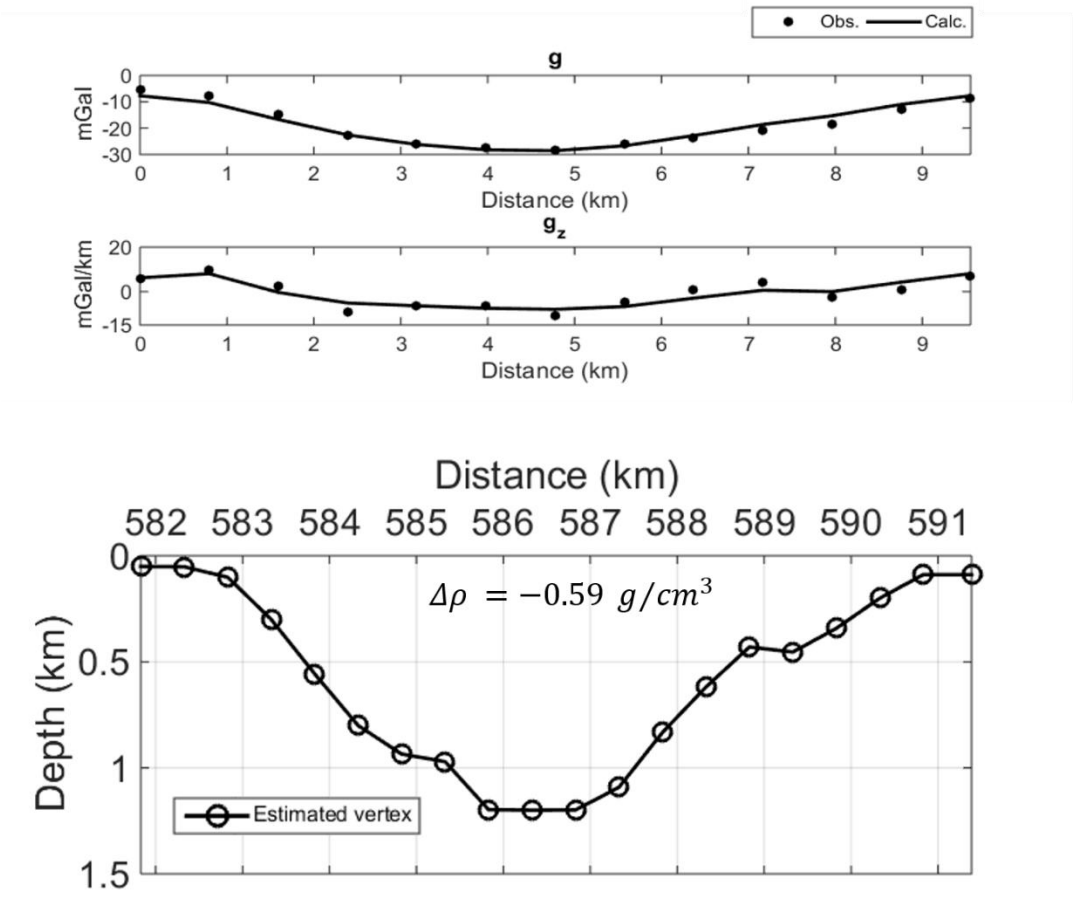

Figure 6.32 – Estimated model for profile7. Top: observed (solid line) and calculated gravity field (dot); middle: observed (solid line) and calculated (dot) first order vertical derivative: Bottom: 2.x D inverted model: black circles indicate the vertices free to move along the depth.

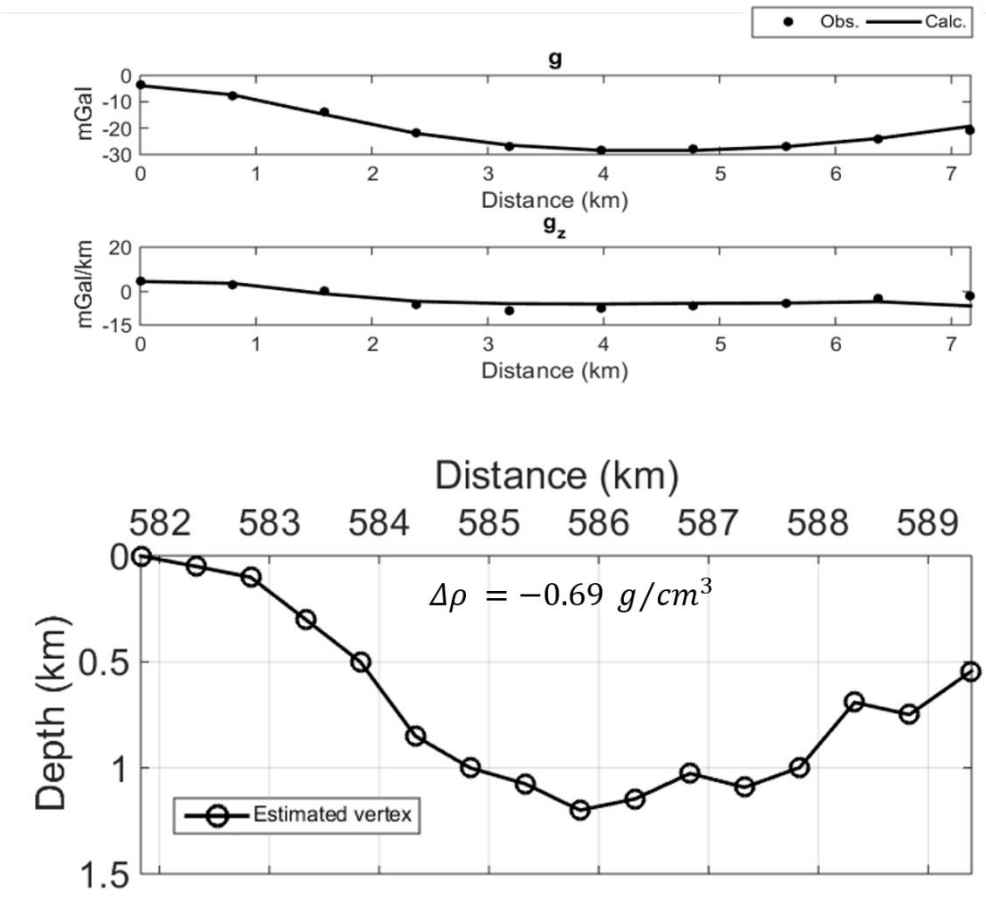

Figure 6.33 – Estimated model for profile 8. Top: observed (solid line) and calculated gravity field (dot); middle: observed (solid line) and calculated (dot) first order vertical derivative: Bottom: 2.x D inverted model: black circles indicate the vertices free to move along the depth.

After having estimated the eight inverted 2.x D models, we may now pass to the second phase of the data processing, aimed to obtain a 3D density model of the area investigated.

6.3 3D inversion of the gravity data in Yucca Flat

The second phase of data processing concerns in the following steps:

- Construction of the mesh-grid in the VOXI tool
- Obtaining the starting model for the 3D inversion by the 2.x D density sections
- 3D inversion and elaboration of the 3D model density
- Producing a depth map of the thickness of the basin and a density contrast vs the depth

Utilizing the VOXI algorithm of the Oasis montaj Geosoft Software, we can build the 3D density model by constrained inversion of the gravity data. The first thing to do is to create a mesh grid constituted by some number of cells; the cells represent the resolution of the model. In the mesh we assume a 0.4 km step along the *x* direction (West – East direction in our real case) and a 0.8 km step along the *y* direction (North – South direction in our real case). Along the *z* direction, the step was 0.05 km with a max depth of 4.3 km.

The second step focuses on assigning a starting model to the 3D inversion, which is the main constraint to invert the gravity data (Figure 6.34). Our constraints are the above illustrated sections and the mean estimated value of density -0.6 g/cm^3, (see paragraph 5.2.3).

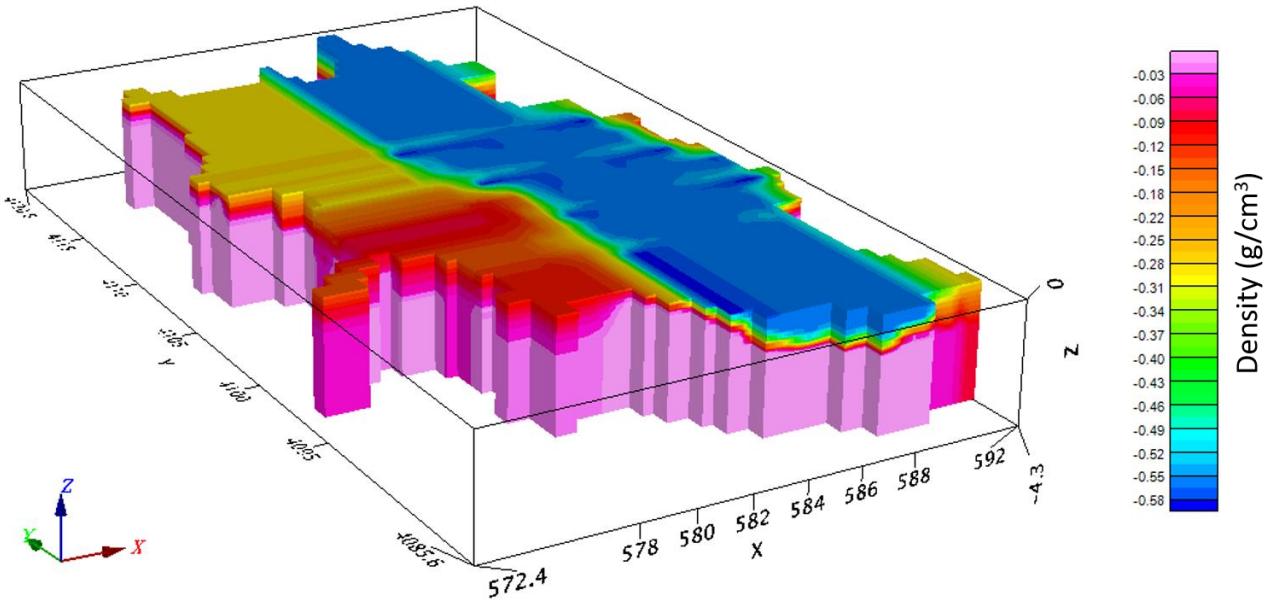

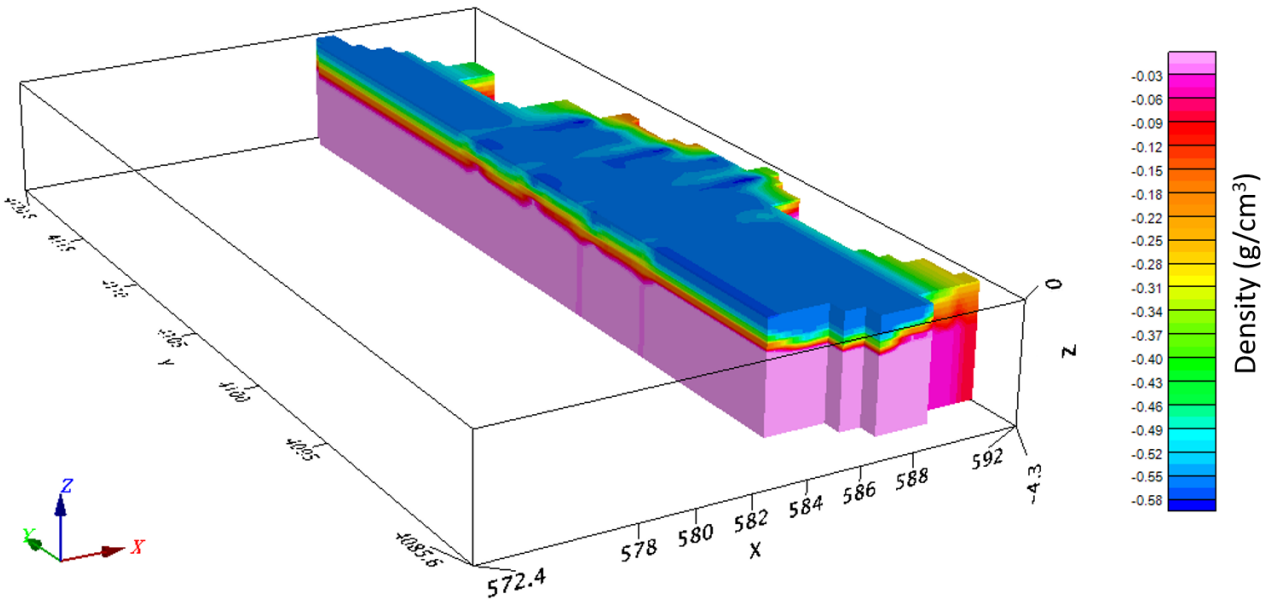

Figure 6.34 – The starting model of the 3D inversion (a); the starting model of the 3D inversion sectioned at x = 584.3 km to observe the bottom of the 2.x D density sections interpolated (b).

In the Eastern zone the density values range from -0.6 to 0 g/cm^3, estimated by the MHODE inversion, are prolonged to North and South, while the Western zone is assigned densities ranging from -0.28 to 0 g/cm^3; in this part of the area we don't have density values constrained to the 2.x D density sections, this range is calculated from the interpolation algorithm during the calculation of the voxel of the starting model. The starting model is the second constraint that we assigned to 3D model. After this we start with the third step of the processing 3D, calculating the 3D inversion and the result of that is represented in Figure 6.35.

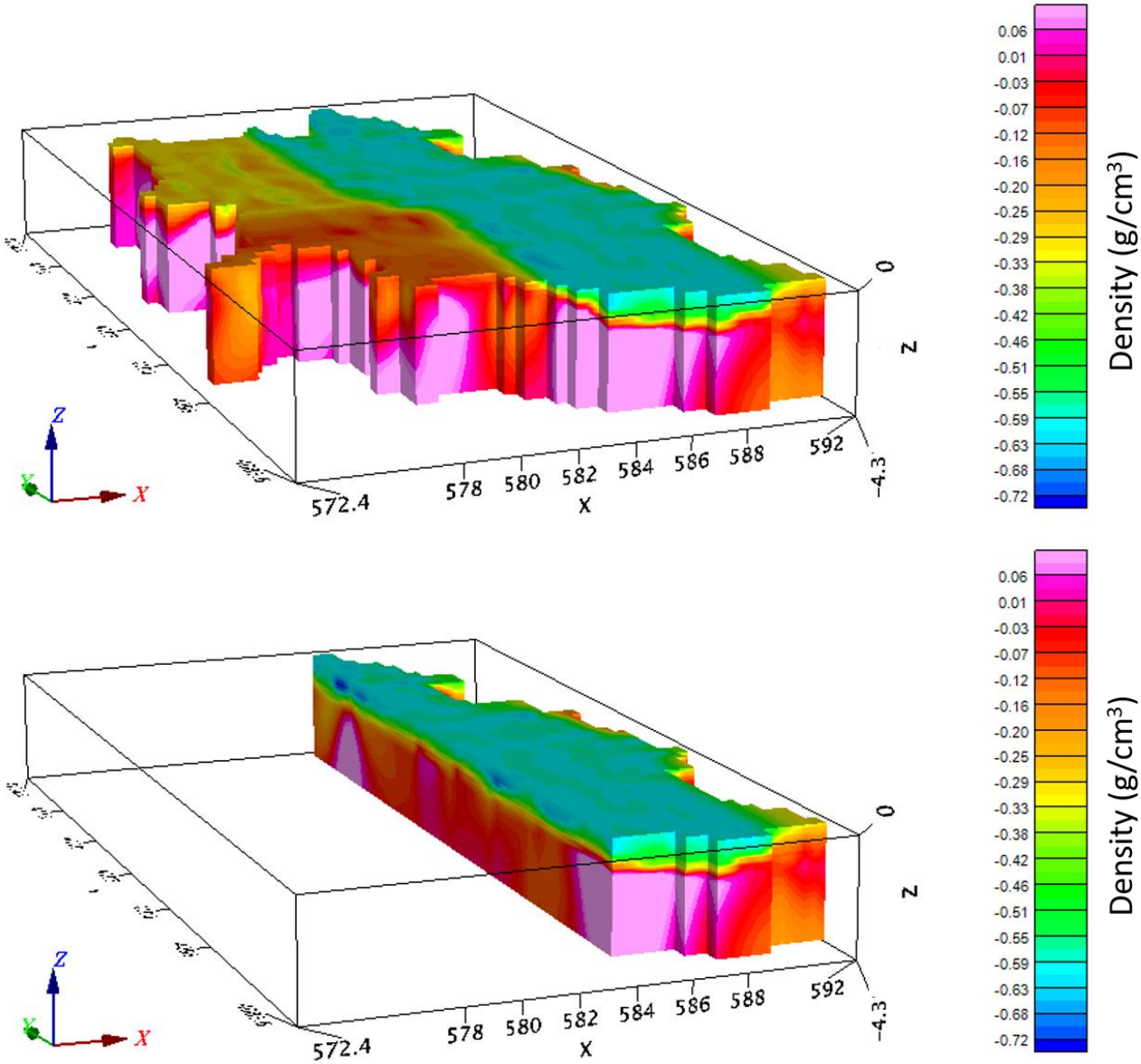

Figure 6.35 – The 3D density model estimated with VOXI inversion (a); The 3D density model estimated with VOXI inversion sectioned at x = 584.3 km to observe the possible contact surface between a basin (less dense) and a basement (more dense) (b).

In figure 6.35a we can see the 3D density model estimated by VOXI inversion. The density contrast changes from -0.76 g/cm^3 to 0 g/cm^3, while in the figure 6.35b we can observe the inner part of the 3D density model and suppose a contact surface between the material less dense and more dense.

In figure 6.36 we show the predicted field by the 3D density model, the observed field and their misfit, showing that our model allows to reproduce very well the measurements.

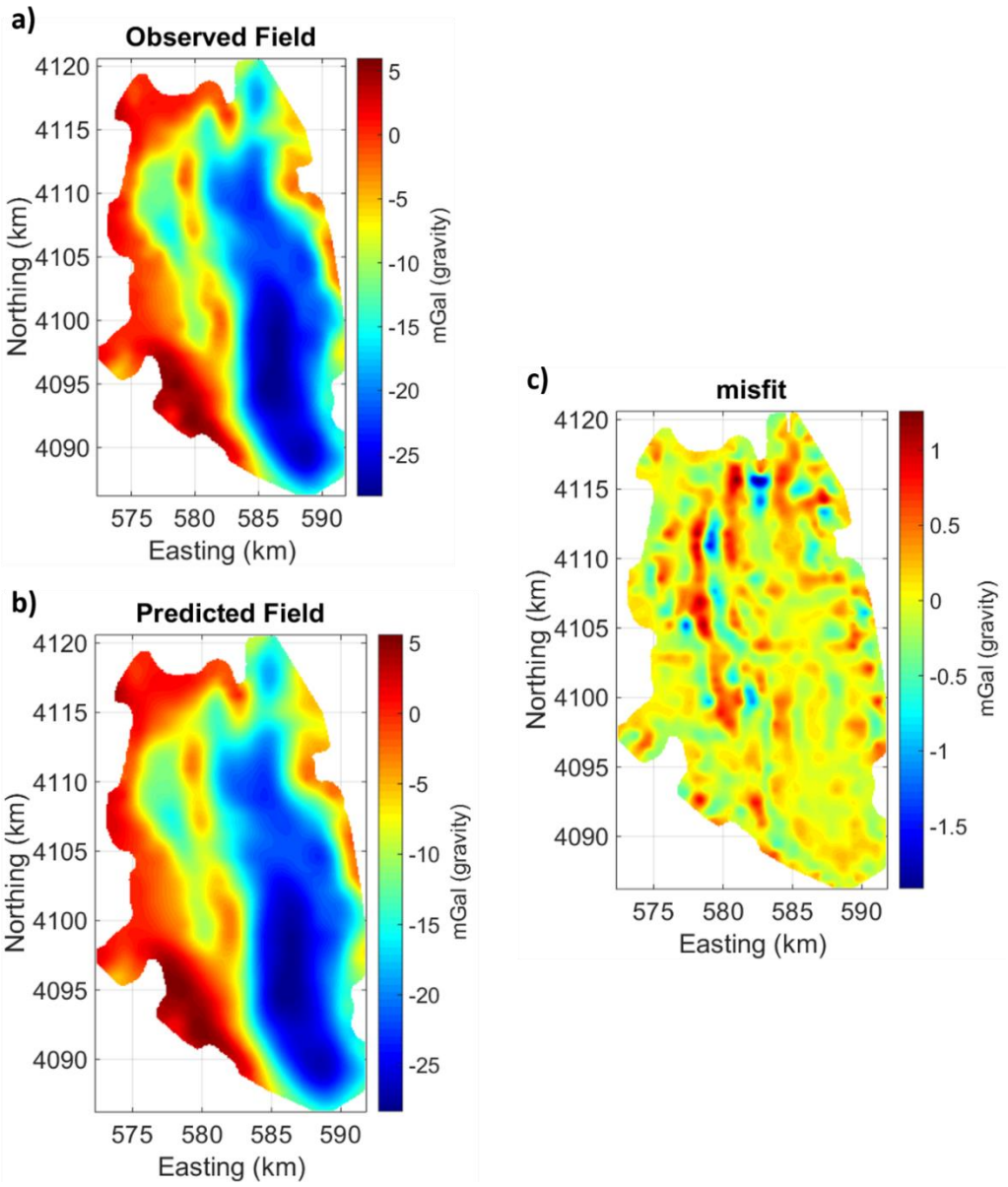

Figure 6.36 – a) Observed gravity field; b) Gravity field generated by 3D VOXI inversion; c) Difference between the observed data and the data predicted by the 3D inversion algorithm.

In fact, the misfit amplitude is 2.7 mGal while that of the gravity data in the Yucca flat basin is 33 mGal. The misfit presents positive anomalies in the South-Eastern zone where we have the most important anomaly in the predicted field, while in the North West zone it is possible to see alternated positive – negative areas, finally in the Western zone we have in the residual map well correlated maximums residuals.

The interface corresponding to a density contrast near to zero can be considered the bottom of the basin. In Figure 6.37 we show the thickness of the basin calculated with respect this interface.

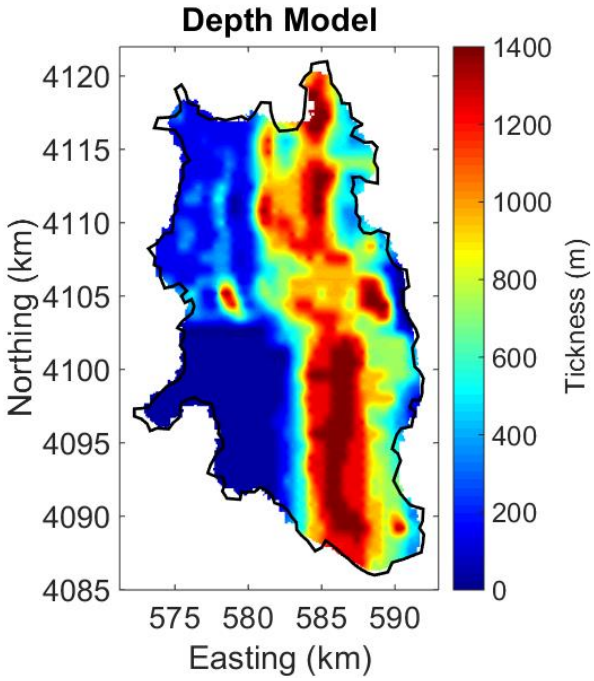

Figure 6.37 –The thickness map of the 3D density model inverted from the gravity dataset of Yucca Flat (Nevada).

The figure shows in the Western zone a shallow depth for the basin, excepted for the area at km 4105N – 580E. By contrast, in the Eastern zone we have the extreme basin deepening, around 1400 meters, interspersed by some more shallow zones.

It is also interesting to calculate the behaviour of the density contrast (Figure 6.38) vs. depth. To see this, we choose the area corresponding to the maximum depth in the 3D model and extracted there the vertical profile of density. To compare it to the results from other studies (see later figure 6.41), we show it positive because referred to the hosting pre-Tertiary basement rocks instead than to the sediments of the basin.

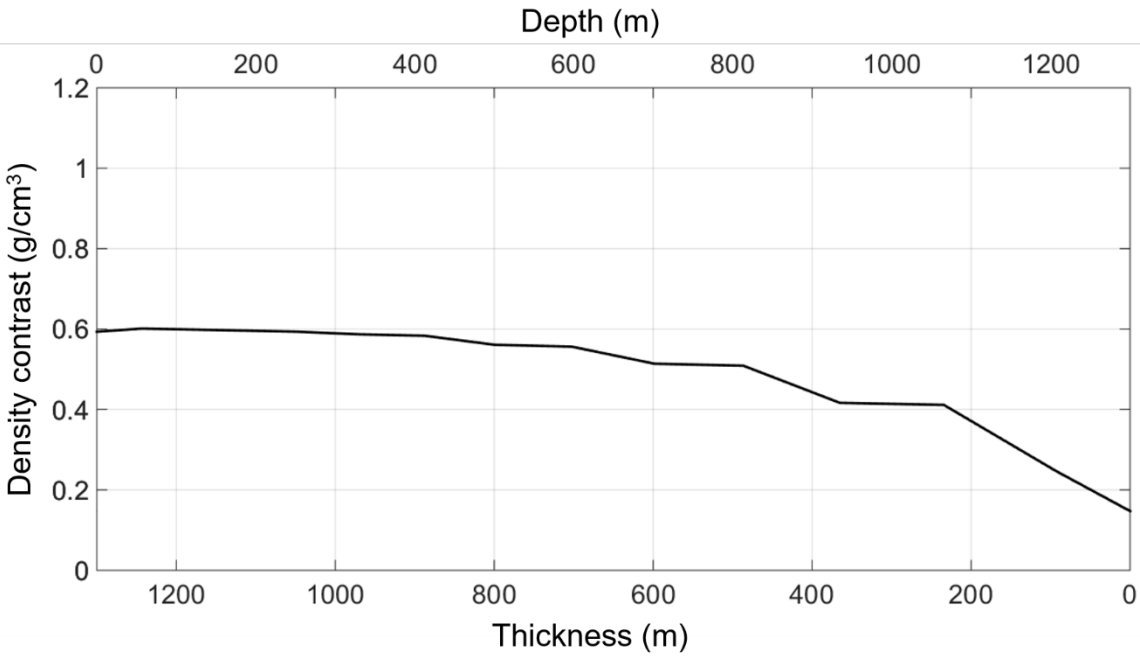

Figure 6.38 – Density contrast vs depth estimated in the investigated area.

As expected, the density contrast model ranges from 0.6 g/cm^3, for the shallowest layer, to around 0 g/cm^3 for the deepest layer. In particular, it is rather constant until a 500 m depth, and decreases slowly to 0.4 g/cm^3 down to 300 m depth, while we see a sharp decrease from 300 m to 1300 m where it goes to around zero.

6.4 Comparison between the calculated 3D model with other basement models and a possible interpretation on the contact surface basin – basement in the Yucca Flat

So far, other researchers worked on the gravity data in the area of Yucca Flat to estimate the pre-Tertiary basement morphology. Ferguson et al. (1988) inverted the data using both the Cordell-Henderson method (Cordell and Henderson, 1968) and the Parker-Oldenburg approach (Oldenburg, 1974), obtaining very similar results from these different techniques. Phelps et al. (1999) used the method of Jachens and Moring (1990), which includes a procedure to estimate and remove the gravity effect generated by density variations in the basement. In 2020, Florio calculated the top of the basement with the *ITerative RESCaling* (ITRESC) *Method for Basement Morphology Modelling* (Florio, 2018).

The models calculated by Florio (2020) and Ferguson et al. (1988), show a good agreement with the density 3D model (this study), estimating a maximum thickness of about 1200 m for one and about 1100 for the other and displaying similar basement features, only in the South West zone where the our model is more shallow respect this models . The basement model by Phelps et al. (1999) (Figure 6.40d) in the North East zone is in very similar to the 3D density model, while in South East zone the surface of interaction basement – sedimentary basin is more depth (around 2500 m).

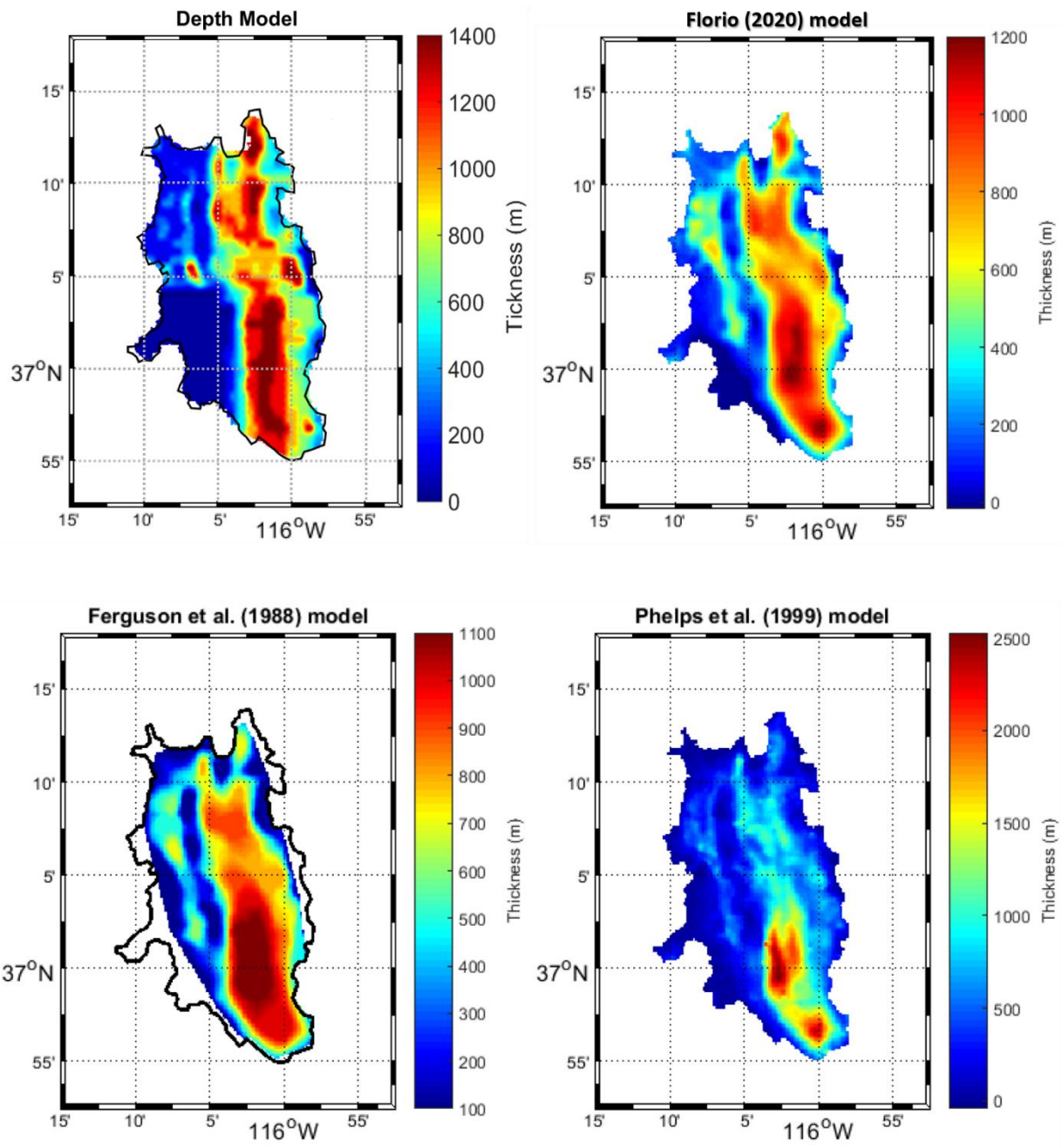

Figure 6.40 – a) Depth model calculated with 3D inversion algorithm; b) Yucca Flat basement model as computed by Florio (2019); c) Yucca Flat basement model, as computed by Ferguson et al. (1988). d) Yucca Flat basement model, as computed by Phelps et al. (1999).

In the study of the function density contrast for all the models (Figure 6.41) Ferguson et al., 1988 estimated a constant density contrast of 0.7 g/cm^3 between the filling sediments and the basement rocks. In the study of Phelps et al. (1999) the density contrast decreases linearly with the depth; this function attributes a density contrast of 0.91 g/cm^3 at the surface and very low values at depth. Finally, Florio (2020) estimated a function density contrast represented into eight straight segments, starting from a value around 1 g/cm^3 near the surface and assumed a constant value of 0.45 g/cm^3 at major depth.

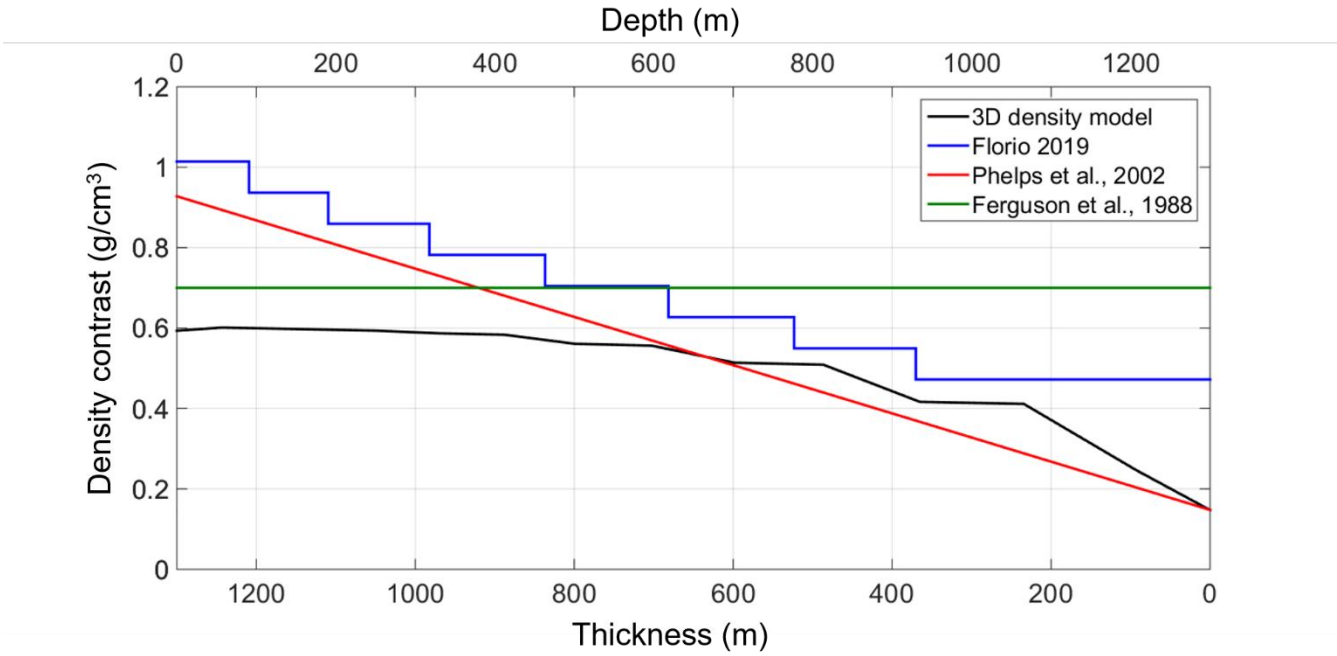

Figure 6.41 - Comparison of the estimated density contrast function with other methods.

Trying to interpret our results from a geological point of view, we now start to analyse the estimated 3D density model (Figure 6.35). We may see that the range between the maximum and the minimum of the density contrast is about 0.7 g/cm^3, which may be justified by the density contrast between an alluvial deposit and a dolomitic - quartzitic basement interred at a greater depth.

On the other hand, studying the behaviour of the density contrast (Figure 6.38) we may assume that the density contrast values in the first 400 metres may be associated to the presence of alluvial deposits, while in the next 400 metres, we may refer to tuff deposits. This contrast decreases drastically and down to the basin bottom, where we intercept the Palaeozoic basement, is around zero.

Finally, if we look at the depth map (Figure 6.37), reporting the basin thickness in all the area, we may attribute to the South-Western area of the basin a basement depth shallower than the South-Eastern area, even though we did not succeed in signing a constrain on the Western area depths. In the North-Western area the thickness behaves as the South-Western area, but we may see a quite shallow depth for the basin, except for an area, located at 4105N km and 580E km, where we notice a local deepening.

CHAPTER 7. MODEL UNCERTAINTY FOR THE SCALING FUNCTION INVERSION OF POTENTIAL FIELDS

Non-uniqueness in potential field inversion is a critical issue, which is sometimes expressed in terms of source ambiguity. Fedi et al., (2005) explained different kinds of source ambiguity which are distinguishable based on their characteristics: for instance, discretization of the continuous field creates a sampling ambiguity, because the spatial distribution of the measurements does not adequately represent the field. Other type of ambiguities, like algebraic and error ambiguities, may occur due to subjective discretization of the source volume and to experimental/instrumental errors. There is also an inherent ambiguity derived from the Green's third identity (e.g., Blakely, 1996; Parker, 1977). The presence of all these ambiguities demands an appropriate a priori information in the inversion. For instance, Barbosa et al. (2002) showed how prior geological information can lead to a unique solution by imposing: a) that the estimated density distribution does not depend on *z* and is confined to a horizontal slab of known position (Smith's theorem, Smith, 1961); b) the estimated source has a known and homogeneous density and is compact. Besides all these kind of ambiguities, inverse problems are instable, and regularization is needed, which worsens further the ambiguity (e.g., Li and Oldenburg, 1996; Zhdanov, 2002; Pilkington, 1997; Paoletti et al., 2013).

In this work, we face the non-uniqueness assuming that the depth to top of the source is sufficiently well known: this important assumption is realistic for compact bodies such as salt-domes, whose depth to the top may be reliably mapped by seismic data. The overall shape of the source is instead not well defined by seismics and, in this case, gravity modeling may help the investigation of the source. It is also realistic for many sedimentary basins, whose top often coincide with the measurement surface.

We will model the gravity source using Talwani's 2D formula (Talwani et al., 1959). The same formula will be used to model the scaling function, which is the derivate of the logarithmic field vs. logarithmic altitude (Fedi, 2007). In order to estimate the source parameters, which are the coordinates of the vertices of the polygonal Talwani's source and the density contrast, we will use global optimization techniques for solving two different problems:

a) the gravity problem, solving for vertex coordinates and density;

b) the MHODE inversion (Fedi et al., 2015; Chauhan & Fedi, 2015; Chauhan et al., 2018), based on the scaling function, solving for the vertex coordinates only and then obtaining the average

density contrast using the found geometrical model. This method was already applied to a synthetic 2D salt dome model and to two real cases: the gravity data of Mors salt dome, Denmark, and Gadavari basin, India (Chauhan, Fedi and Sen, 2018).

It is really interesting to compare the inversions of the scaling function and gravity. This because of one main property of the scaling function: it depends on the geometrical features of the source, but it does not depend on the density. So, with the scaling function inversion, the density is estimated after the shape and depth of the source have been inverted, while with the gravity inversion the density is one of the unknowns. In this way, the two approaches will both lead to a model of the source geometry and density, but we expect that the respective uncertainty will be different. The study of the model uncertainty so becomes the main goal of this work.

In the following sections we will first describe the MHODE method and the global optimization inversion used for inverting both the scaling function and gravity, the very fast simulated-annealing algorithm (VFSA; Ingber 1989; Sen and Stoffa 1995). We will then study the uncertainty of the geometrical source parameters and of the density of the estimates from both the kinds of inversion for noise-free data and noisy synthetic data; finally, the uncertainty analysis will be made for the real cases of the Mors Salt Dome (Denmark) and the Decorah basin, Iowa (USA).

7.1 Methodology

In this section, we introduce the forward calculation and inversion approach of either the gravity or the scaling function problems. The assumed model for synthetic and for real case interpretation is that of complex structures, which can be straightforward modelled with the polygonal approximation of the Talwani's 2D formula. In fact, the field of any homogeneous 2D sources can be approximated by that of a polygon of q sides (e.g., Talwani Blakely, 1996):

$$g_i = 2\gamma\rho \sum_{q=1}^{Q} \frac{\beta_q}{1+\alpha_q^2}\left[\log\frac{r_{q+1}}{r_q} - \alpha_q(\theta_{q+1}-\theta_q)\right] \qquad (7.1)$$

where g_i is the gravity field calculated at each observation point, i=1,..., L; ρ is the density contrast, γ is the gravitational constant, x_q and z_q are the coordinates of the vertices of the polygon

and $(\bar{x}_i, \bar{z}_i), i = 1, \ldots, L$ are the coordinates of the measurement points. Other quantities of Equation (7.1) are:

$$\alpha_q = \frac{x_{q+1} - x_q}{z_{q+1} - z_q}, \quad \beta_q = \left(x_q - \bar{x}_i\right) - \alpha_q\left(z_q - \bar{z}_i\right)$$

$$r_q = \left[\left(x_q - \bar{x}_i\right)^2 + \left(z_q - \bar{z}_i\right)^2\right]^{\frac{1}{2}}$$

$$r_{q+1} = \left[\left(x_{q+1} - \bar{x}_i\right)^2 + \left(z_{q+1} - \bar{z}_i\right)^2\right]^{1/2}$$

$$\theta_q = \tan^{-1}\left(\frac{z_q - \bar{z}_i}{x_q - \bar{x}_i}\right), \qquad \theta_{q+1} = \tan^{-1}\left(\frac{z_{q+1} - \bar{z}_i}{x_{q+1} - \bar{x}_i}\right)$$

Now a system of equation can be formed at points $(\bar{x}_i, \bar{z}_i), i = 1, \ldots, L$ along the profile as follows:

$$\begin{bmatrix} g\left(\rho, \bar{x}_1, \bar{z}_1, x_1, .., x_q, z_1, .., z_q\right) = g(\bar{x}_1, \bar{z}_1) \\ \ldots \qquad\qquad\qquad\qquad\qquad\qquad \ldots \\ g\left(\rho, \bar{x}_i, \bar{z}_i, x_1, .., x_q, z_1, .., z_q\right) = g(\bar{x}_i, \bar{z}_i) \\ \ldots \qquad\qquad\qquad\qquad\qquad\qquad \ldots \\ g\left(\rho, \bar{x}_L, \bar{z}_L, x_1, .., x_q, z_1, .., z_q\right) = g(\bar{x}_L, \bar{z}_L) \end{bmatrix} \qquad (7.2)$$

where the vertex coordinates $\{x_q, z_q\}$ and the density contrast ρ are the unknown quantities.

The scaling function, τ, can be calculated directly from the potential field f by a simple mathematical expression (Fedi, 2007; Chauhan et al., 2018):

$$\tau = \frac{\partial \log(f)}{\partial \log(z)} = \frac{1}{f}\frac{\partial \mathrm{f}}{\partial \mathrm{z}} z \qquad (7.3).$$

For ideal sources, i.e., whose fields are homogeneous, the scaling function assumes an easy form:

$$\tau = \frac{nz}{z - z_0} \qquad (7.4).$$

where z is the altitude, n is the degree of homogeneity and z_0 is the depth to the source. The strength of τ is that it does not depend on density and that it is dimensionless. The dependency of

τ on the altitude z candidates it to be studied as a multiscale function. It has been in fact studied along the ridges (i.e., the lines formed by the zeros of the field derivatives at different altitudes) in the 3D space (Fedi, 2007).

The scaling function, however, is not only important for homogenous functions, but may be used also to study inhomogeneous fields, i.e. fields whose homogeneity degree varies in the space. Fedi et al. (2015) made a detailed explanation of its extension to inhomogeneous fields and described how to form an inverse problem for the scaling function, that allows us not to involve the density among the unknown parameters. Further studies generalized the scaling function approach (Chauhan & Fedi, 2015; Chauhan et al., 2017 (a; b); Chauhan et al., 2018) for inversion of the fields of sources having irregular shapes and also extended the formula (Equation 7.3) for the scaling function relative to high-order derivatives:

$$\tau_p = \frac{\partial \log(f_p)}{\partial \log(z)} = \frac{1}{f_p}\frac{\partial f_p}{\partial z} z \qquad (7.5)$$

where p is the order of differentiation of the field f. See Chauhan et al. (2018) for further details on Talwani's formulas updated for p=1 and p=2. Since, the gravity field calculated by Equation (7.1) is due to multi-point sources, hence an inhomogeneous field, we can form a system of equation for the scaling function by using Talwani's formula:

$$\begin{bmatrix} \tau_T(\bar{x}_1, \bar{z}_1, x_1, .., x_q, z_1, .., z_q) = \tau(\bar{x}_1, \bar{z}_1) \\ \dots \qquad\qquad\qquad\qquad \dots \\ \tau_T(\bar{x}_i, \bar{z}_i, x_1, .., x_q, z_1, .., z_q) = \tau(\bar{x}_i, \bar{z}_i) \\ \dots \qquad\qquad\qquad\qquad \dots \\ \tau_T(\bar{x}_L, \bar{z}_L, x_1, .., x_q, z_1, .., z_q) = \tau(\bar{x}_L, \bar{z}_L) \end{bmatrix} \qquad (7.6)$$

where $(\bar{x}_i, \bar{z}_i), i = 1, \dots, L$, are the coordinates of points along the ridges where the scaling function is estimated and τ_T is the theoretical scaling function that is calculated by using Equations (7.1) and (7.3). It is worth noting again that the system in Equation (7.6) is only function of the geometrical source parameters and it is independent on the density.

We will now find the solutions of the equation systems (7.2) and (7.6) by using the global optimization technique Very Fast Simulated Annealing (VFSA; Ingber 1989; Sen and Stoffa 1995). Both the problems represented by the systems are non-linear vs. the coordinates of the vertices and the degree of non-linearity depends on the number of vertices of the polygon, as each vertex

adds two unknowns to search for. The gravity problem (Equation 7.2) is however linearly related to density, as a further unknown.

7.2 Inversion of gravity and the scaling function

For optimizing the system of equations (7.2) and (7.6) we used the Very Fast Simulated Annealing (VFSA) algorithm. Since, the scaling function does not depend on density (Equations 7.3-7.5), the goal is to estimate the geometrical parameters of the causative source; in the gravity inversion (Equation 7.2) however the density is an unknown quantity as well.

In the next section we will explore the possibilities of getting a reliable model through gravity and scaling function inversion. Due to the main ambiguity of both the problems, a priori information is needed. In this paper we will consider source geometries typical of salt domes and sedimentary basins. In the case of salt domes, we will take the opportunity to borrow the information on the depth to top from seismic data and will search to define the rest of the main source geometry (typically poorly defined by seismic) with the scaling function and gravity field inversion. In the case of sedimentary basins, the problem is simpler since the source *x*-position is easily established along the profile and the depth to the top is often known, as coincident with the measurement surface. We will therefore try to analyze the unknown uncertainties of the estimated vertices at the flanks and at the bottom of the source. Regarding the density it will be estimated for the gravity inversion as that of one of the parameters; in the case of the scaling function inversion it will be estimated instead as that deriving from the density estimates computed for the Talwani's model vertices.

First of all, we define the data vector as d^{obs} and define the following error function:

$$E = \sum (d^{obs} - d^{pre})^2, \qquad (7.7)$$

where d^{pre} is the predicted data vector.

Now we use the VFSA algorithm in order to minimize the error function (Equation 7.7) for both the scaling function and gravity inversion. VFSA is an efficient method to find optimal model parameters in highly non-linear problems, at less computational cost compared to algorithms based on Monte Carlo or grid search (Roy et al., 2005, Sen and Stoffa, 2013). The method was proposed by the Ingber (1989), as an advanced version of *simulated annealing* (SA), whose concept lies in to

the thermodynamic according to the different cooling states of a molten material (Sen and Stoffa, 2013). The energy E_i (for the i^{th} state) can be defined by the Gibbs probability density function P (or Boltzmann pdf) as:

$$P(E_i) = \frac{\exp\left(-\frac{E_i}{KT}\right)}{\sum_{j \in S} \exp\left(-\frac{E_j}{KT}\right)} = \frac{1}{Z(T)} \exp\left(-\frac{E_i}{KT}\right) \quad , \qquad (7.8)$$

where K is the Boltzmann's constant, T is the temperature, S is the set of all the possible configurations and $Z(T)$ is the partition function:

$$Z(T) = \sum_{j \in S} \exp\left(-\frac{E_j}{KT}\right) \quad , \qquad (7.9)$$

Since we are interested to search for the unknown model parameters given in Equation 7.2 and 7.6, the random selection of the model in each iteration is a state of the process. The algorithm draws the model randomly from the Cauchy-like distribution and the shape of the distribution is regulated by the temperature T. In order to achieve the global minimum of E, the process should approach the equilibrium state slowly rather cooling down rapidly which eventually can lead to the local minima (Sen and Stoffa, 2013) of the error function (Equation 7.7). For further detailed description of the algorithm and its application, we refer to Sen and Stoffa (2013) and references therein.

We here also use the algorithm to quantify the uncertainties in the model space. Sen and Stoffa (1996) have shown that VFSA can be used to find a balance between the model evaluation and accuracy, by allowing numerous runs and using appropriate cooling schedule and convergence criteria. However, to avoid the biasness and to sufficiently sample the model space (Sen and Stoffa, 1996) it is advisable to repeat the algorithm for a number of times with a random initial guess of the model parameters. We adopted this strategy and run the algorithm several times with thousands of iterations in each run, so providing a completely random initial guess. We then collected the models (m_i) after the algorithm convergences for each run (misfit error stabilization) and calculated the statistical parameters, mean $\langle m \rangle$ and standard deviation σ as:

$$\langle m \rangle = \frac{1}{N}\sum_{i=1}^{N} m_i \,, \qquad \sigma = \sqrt{\frac{1}{N}\sum_{i=1}^{N}(m_i - \langle m \rangle)^2} \,. \qquad (7.10)$$

in order to estimate the uncertainties associated with a particular unknown parameter.

In the next section we will show the depth estimations by the gravity and scaling function inversions for complex synthetic examples and for a real case example and will discuss the respective uncertainties in the model parameters.

7.3 Model uncertainty estimation

Synthetic Example

We have selected a complex shape model, as shown in Figure 7.1(a) (black solid line) approximating a salt like structure. Chauhan et al., (2018) interpreted the same model for source parameters estimation using inversion of the scaling function only. In this work, they also demonstrated that increasing the number of vertices improve the overall fitting of the scaling function (Figure 4; Chauhan et al., 2018).

Since our goal is here to explore the uncertainties in the source region, we decided to make the problem simpler as possible, which means invert for only four vertices. We here present the analysis led in the case of error-free and noisy data.

ERROR-FREE CASE

We inverted the scaling function and gravity using the same strategy explained in the methodology section. We used the same criteria for inverting both the gravity and scaling function datasets, as presented in the Figure 7.1 and Figure 7.2, respectively. It is immediately clear than, despite of the inherent roughness related to use four vertices only, the scaling function inversion is able to identify quite well the tilt of the structure, while the gravity depicts a too symmetrical source (Figures 7.1a and 7.2a). The associated error bar (Figure 7.1a and 7.2a) shows the standard deviation in the *x*-*z* directions of the estimated vertices, which are calculated using the Equation 7.10. This can be due to the fact that the scaling function is independent on the density in the inversion, leading therefore the fitting of the scaling function deserved only to the geometrical features of the source. Contrarily, density adds as a further unknown parameter in the gravity inverse problem.

Hence, due to inherent ambiguity, there can be a wide range of combination of density and geometrical features, in turn related to the source volume, which fit the gravity equally well.

In the case of the scaling function inversion, the density is post-calculated using a 1st-order regression analysis between the observed gravity anomaly and the data calculated from each reconstructed geometrical model, with a unit density (Chauhan et al., 2018). Since the retrieved models by the scaling function inversion are fairly well consistent, the estimated density distribution (Figure 7.1c) for each model is concentrated almost well around the assumed density contrast (-0.2 g/cm^3).

Instead, the density contrast retrieved by the gravity inversion is widely dispersed (Figure 7.2c) and it is difficult to decide the value to estimate: the mode (most frequent value) is higher than the true one (-0.1 g/cm^3), but the mean is considerably lower (-0.35 g/cm^3) than either the true value (-0.2 g/cm^3) or the mean value estimated in the scaling function inversion (-0.19 g/cm^3, Figure 7.1c).

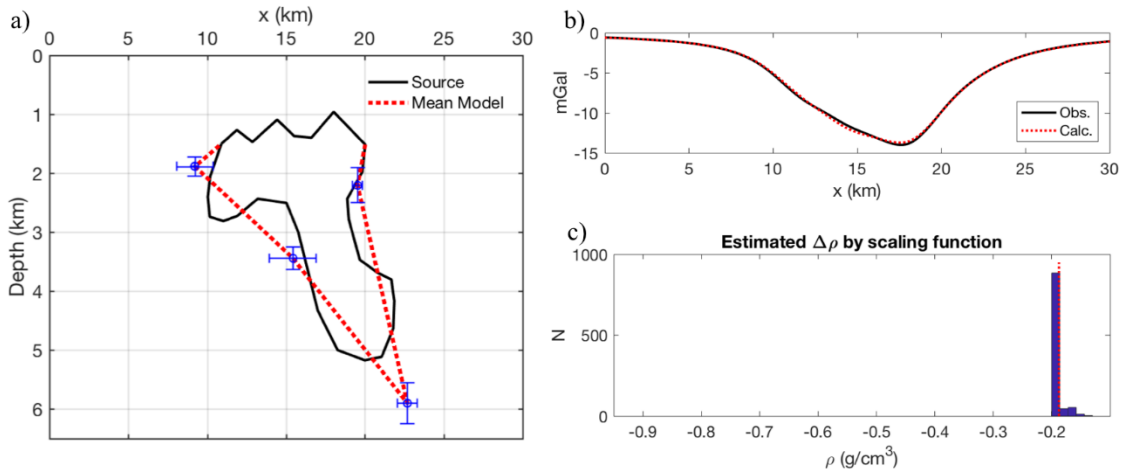

Figure 7.3: a) Inverted model by scaling function inversion and error bars relative to the standard deviation from mean value in x-z direction for each estimated vertex; b) gravity anomaly using the mean model; c) histogram of the densities retrieved for each model. The density retrieved by the mean mode is indicated by a red line.

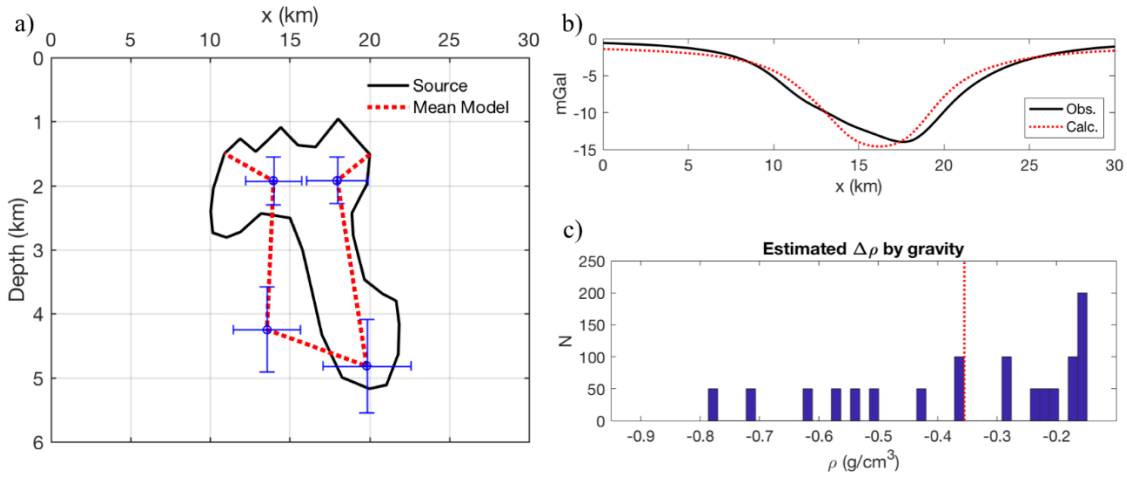

Figure 7.4: a) Inverted model by gravity inversion and error bars relative to the standard deviation from mean value in x-z direction for each estimated vertex; b) gravity anomaly using mean model; c) histogram of the densities retrieved for each model. The density retrieved by the mean mode is indicated by a red line.

NOISY CASE

We repeat the test on the same source by adding Gaussian noise with zero mean and standard deviation equal to 10% of the anomaly amplitude. Taking advantage of the multi-scale approach, we can simply discard the too noisy data at the lower altitudes and calculate the scaling function along the ridges at high altitudes only, that is at altitudes greater than 1.5 km for gravity and greater than 2 km for gravity derivatives (Figure 7.3).

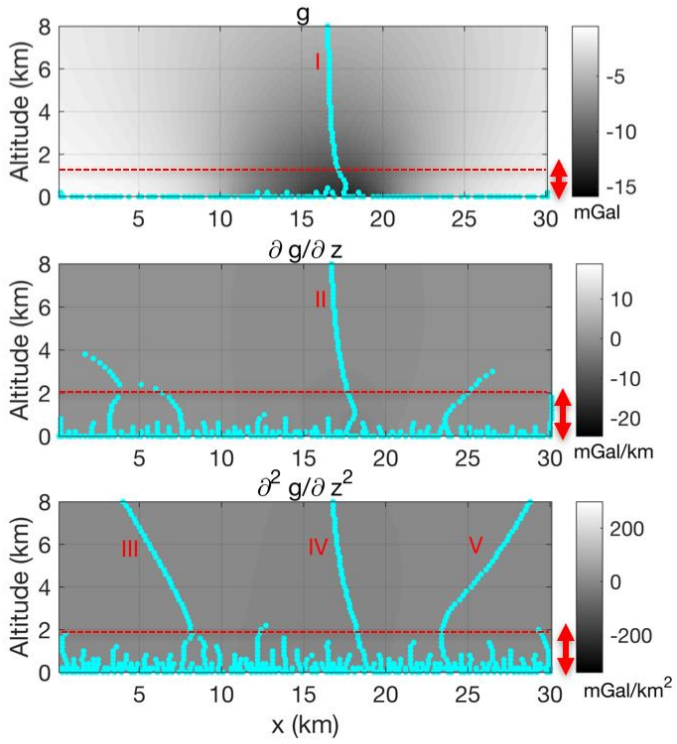

Figure 7.5: Calculated ridges for the noisy gravity data.

We, then invert the scaling function and gravity data using the same approach as for the noise-free case. Once again, the results of scaling function inversion are quite stable and the retrieved models are not only the less ambiguous on both the horizontal and vertical coordinates but also the tiltness of the source is well recognized (Figure 7.4 a-b). Though the error in the depth coordinates of the vertices slightly increased (Figure 7.1a and 7.4a), they are still better than those obtained with the gravity inversion (Figure 7.2a and 7.5a). As a consequence, the distribution of the density contrast in both the cases has the same characteristics as for the noise-free case (Figure 7.4c and 7.5c).

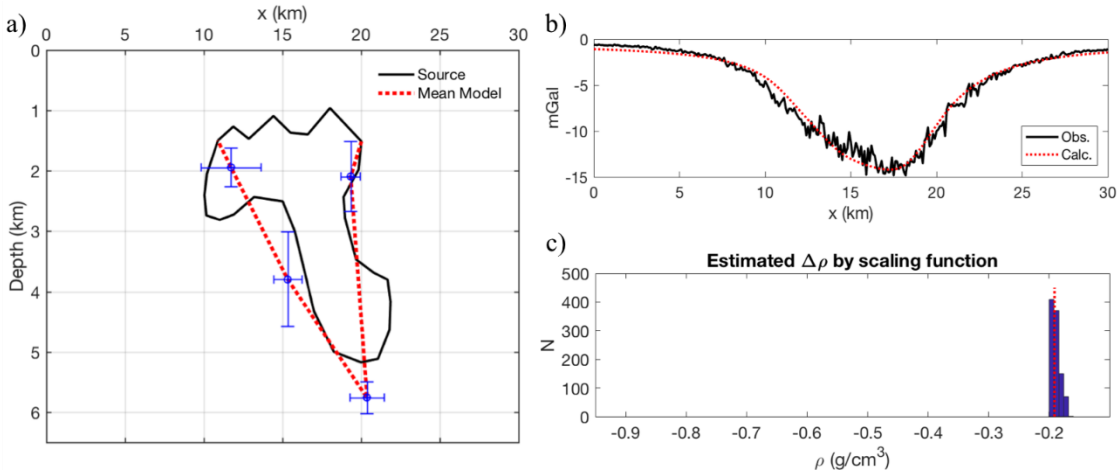

Figure 7.6: Noisy case: a) Inverted model by scaling function inversion and error bars relative to the standard deviation from mean value in x-z direction for each estimated vertex; b) gravity anomaly using mean model; c) histogram of the densities retrieved for each model. The density retrieved by the mean mode is indicated by a red line.

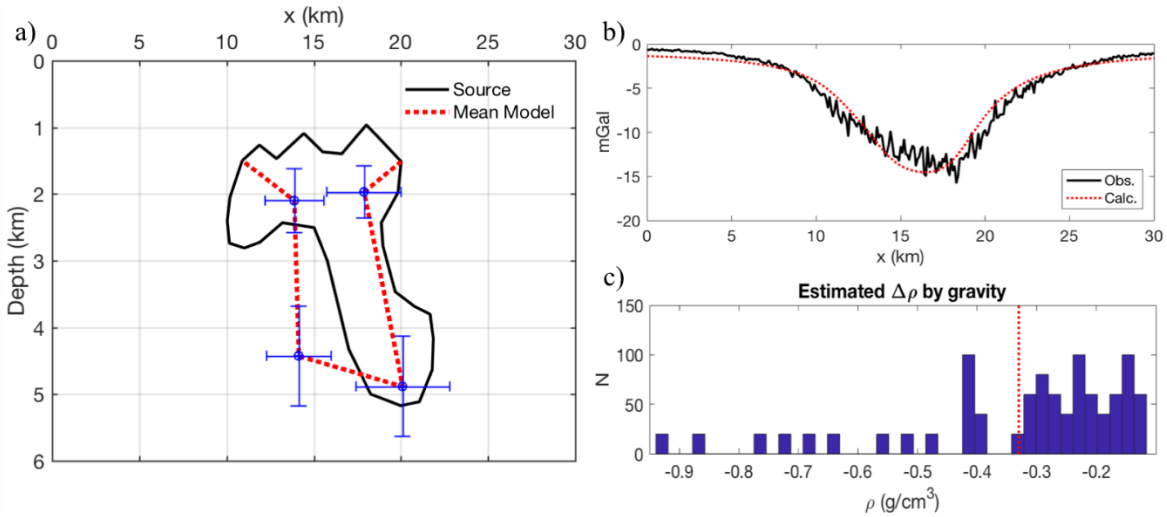

Figure 7.7: Noisy case: a) Inverted model by gravity inversion and error bars relative to the standard deviation from mean value in x-z direction for each estimated vertex; b) gravity anomaly using mean model; c) histogram of the densities retrieved for each model. The density retrieved by the mean mode is indicated by a red line.

7.4 Real Case Examples

Mors Salt dome

We apply the same methodology on the Mors salt dome in Northern Jutland (Reynolds, 1997). The earlier studies (Sharma, 1986; Reynolds, 1997) for this gravity anomaly were done for the safe disposal of the radioactive material. However, our interest is to analyze the above defined methodology on a real data over the salt dome, differently than Chauhan et al. (2018) as they have interpreted the salt dome like structure to find the best fit model from the scaling function inversion. The data for this case study was digitized from the map (Figure 2.37) of Reynolds (1997). The calculated ridges for the gravity data are shown in Figure 7.6.

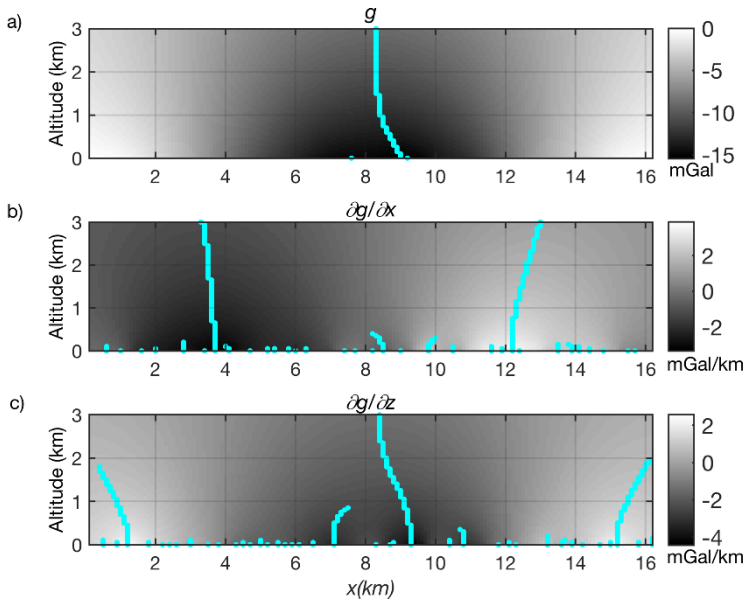

Figure 7.8: Calculated ridge for the gravity anomaly over the Mors Salt Dome.

The resulted models obtained from the scaling function and gravity inversion do not differ very much, but the uncertainty (red color error bar Figure 7.7c and 7.8c) associated with the estimated coordinates of the vertices is slightly higher in the gravity inversion (Figure 7.8c). Interestingly, the estimated density distribution for all the retrieved model is significantly different. In case of the scaling function inversion density distribution (Figure 7.7b) the distribution is very concentrated, with mean value: $-0.163\ g/cm^3$. However, using the bounds (-3.0 to 0 g/cm^3) for density in the gravity inversion, the distribution (Figure 7.8b) of density is comparatively wide and overestimated with the mean occurring nearly at $-0.122\ g/cm^3$. Comparing our analysis of

density estimation with the earlier study ($-0.17\ g/cm^3$ in Chauhan et al., 2018), the density retrieved by the scaling function inversion is better suited.

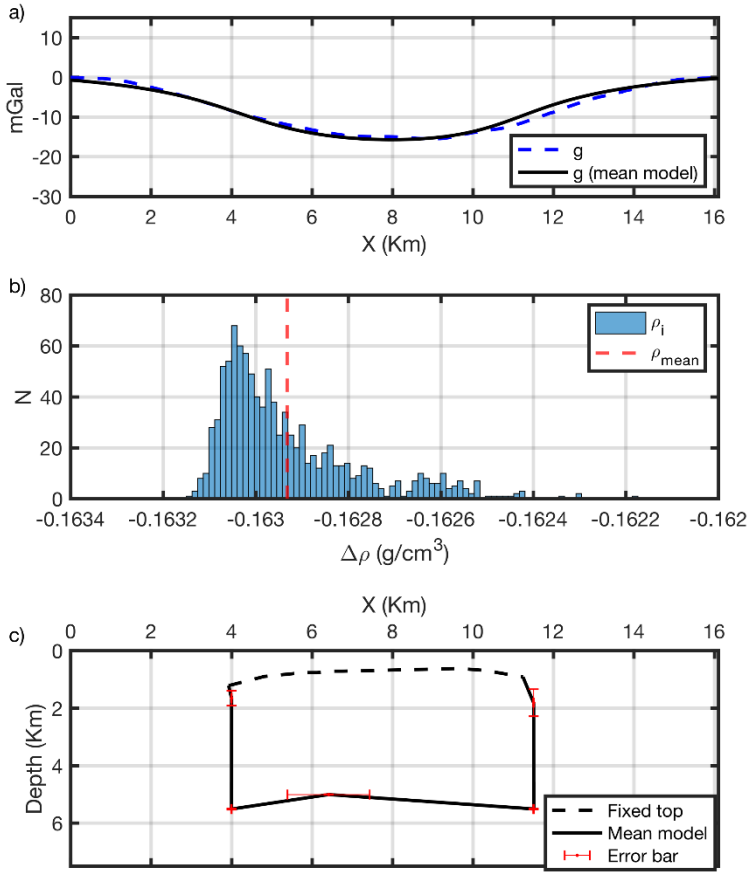

Figure 7.9: (a) gravity anomalies; (b) histogram of the densities retrieved for each model. The density retrieved by the mean mode is indicated by a red line; (c) estimated final mean model with error bar in depth-coordinates whose anomaly is plotted in the upper panel (a) in black solid color.

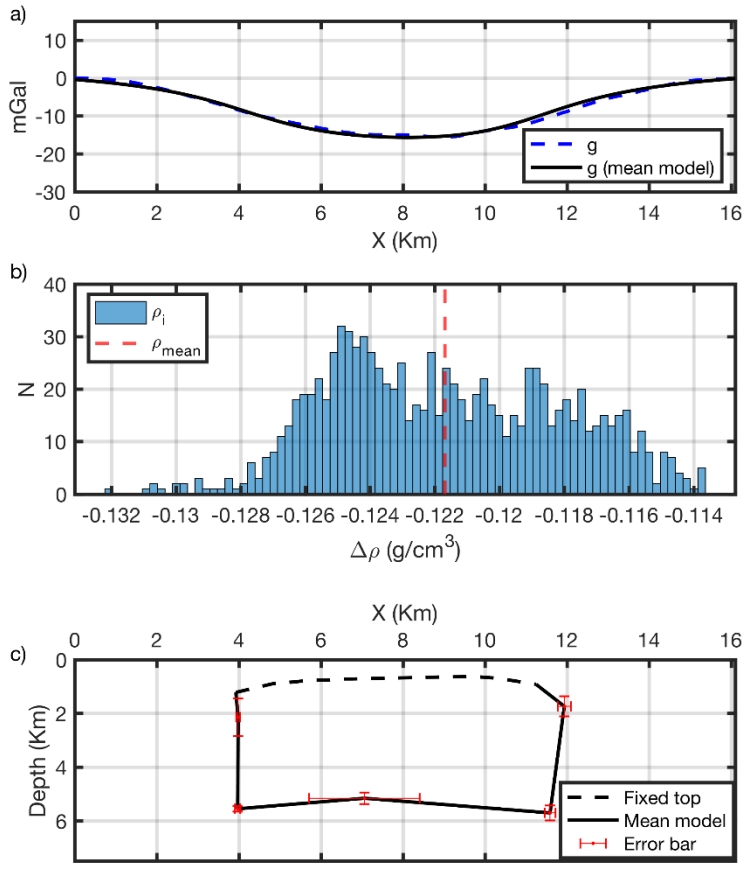

Figure 7.10: (a) gravity anomalies; (b) histogram of the densities retrieved for each model. The density retrieved by the mean mode is indicated by a red line; (c) estimated final mean model with error bar in depth-coordinates.

Decorah Basin

We apply the same strategy for interpretation the gravity data of Decorah, North-Eastern Iowa (USA). The whole surface of Iowa county is deeply covered by deposits of Pleistocene and Recent age; this type of rocks covers the county to a depth varying from a few inches to several hundred feet. The stratigraphic column of IOWA (USA) (IOWA Geological Survey) shows at the top sandstones, siltstones and shales, down to a depth of about 4 km, where these sediments lay on a Palaeozoic carbonate basement, made of limestones and dolomites. At around 14 km there is a crystalline basement constituted of igneous and metamorphic rocks. The observation of this gravity anomaly allows us to assume in the interpretation phase that the gravity data can be interpreted with the undulations of a Palaeozoic carbonate basement, buried under sands and clays.

The gravity map (Figure 7.9a) is obtained from the gradiometry data as described in the Final Report, Processing and Acquisition of Air-FTG® Data Decorah, Iowa for United States Geological Survey (2013). The profile is extracted from the map along the red line profile, that crosses the negative anomaly in the NE on the map. Ridges are calculated for the gravity and the first-order of

vertical and horizontal derivatives, as shown in Figure 7.9 b-d. We then run the algorithm with the similar approach defined above and collected the models obtained from the scaling function and gravity inversion.

The obtained models have a bottom depth which varies from about 5 km to about 2 km (Figure 7.10c and 7.10c) in both the inverted models (scaling function and gravity data). The estimated mean density contrasts from the scaling function and gravity inversion are rather similar, $\Delta\rho \approx -0.242\ g/cm^3$ and $\Delta\rho \approx -0.231\ \mathrm{g/cm^3}$, respectively (Figure 7.10b and 7.10b). Using the mean geometrical model and the estimated mean density, the gravity data are well fitted in both the cases, as shown in Figures 7.10a and 7.11a. The uncertainties in the scaling function inversion are once again lower than those for the gravity inversion (as shown by error bars in Figure 7.10c and 7.11c) and also the obtained density is narrowly distributed in the results obtained from the scaling function inversion (Figure 7.10b), compared to the gravity inversion (Figure 7.11b). So, even though the average density contrasts are rather similar, the inversion for the scaling inversion yields again a more confident result.

Taking into account the obtained information, we can say that the estimated model is consistent with the investigated sedimentary basin. By looking at the stratigraphic column (http://publications.iowa.gov/4862/, 2004) we may notice that the carbonate basement is located approximately at a 4 km depth. Accordingly, we may associate our depth model to the top of the carbonate basement. Besides, assuming that sands and clay density are in the range 2.3 – 2.6 $\mathrm{g/cm^3}$ and the carbonate basement density in the range 2.6 – 2.9 $\mathrm{g/cm^3}$, we may say that the estimated density is very close to their density contrast, $\Delta\rho = -0.3\,\mathrm{g/cm^3}$. In conclusion, gravity data can be interpreted with the undulations of a Palaeozoic carbonate basement, buried under sands and clays.

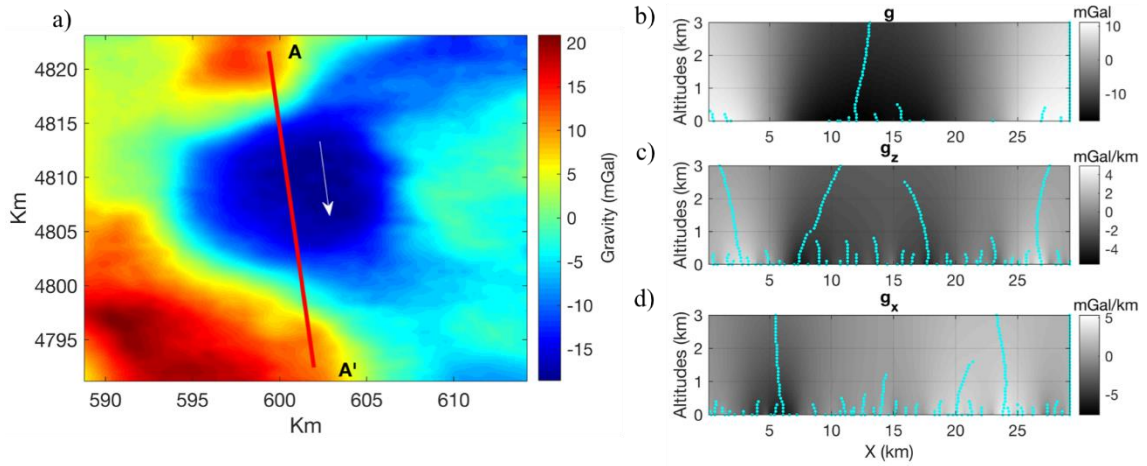

Figure 7.11: (a) Gravity map of the Decorah area (USA); (b) calculated ridges of the extracted gravity profile from map along the red line; (c) ridges of the calculated vertical derivative of the gravity profile; (d) ridges of the horizontal derivative of the gravity profile.

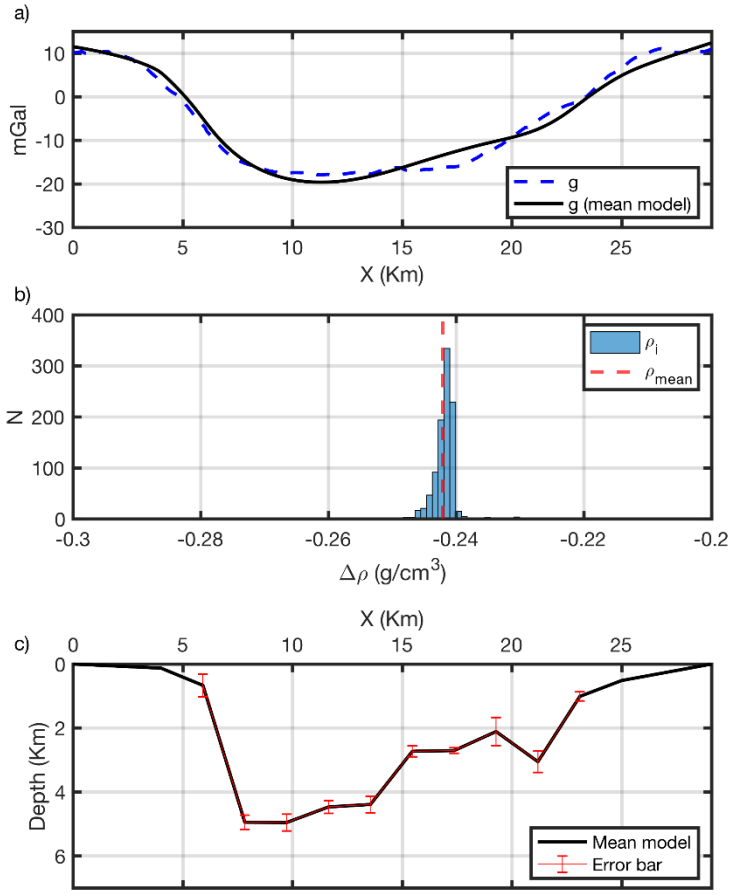

Figure 7.12: (a) gravity anomalies; (b) histogram of the densities retrieved for each model. The density retrieved by the mean mode is indicated by a red line; (c) estimated final mean model with error bar in depth-coordinates whose anomaly is plotted in upper pane (a) in black solid color.

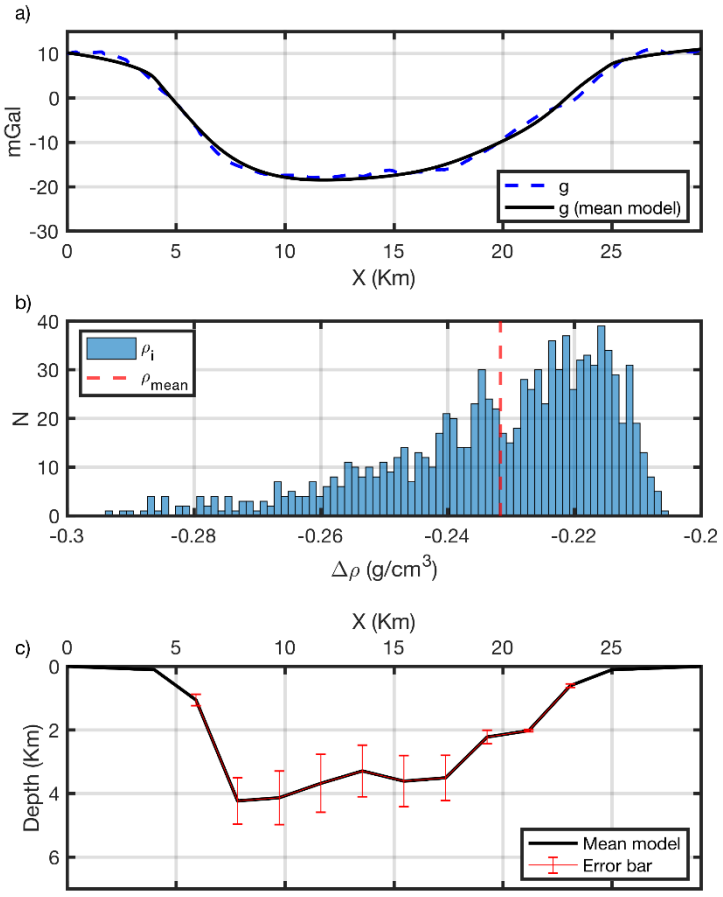

Figure 7.13: (a) gravity anomalies; (b) histogram of the densities retrieved for each model. The density retrieved by the mean mode is indicated by a red line; (c) estimated final mean model with error bar in depth-coordinates and smoothed model.

Conclusions

Uncertainty is an inherent issue in the process of estimating source parameters from inversion of geophysical data. Its evaluation is important to make less ambiguous the geological modelling of potential field data. We here explore whether the newly developed inversion approach, based on the scaling function, is advantageous when compared to the classical gravity inversion. The first advantage comes from mathematical considerations: the scaling function is independent on density or any other physical constant. Therefore, we may form a system of equations whose unknowns are the geometrical parameters of the source only, differently to gravity inversion where density adds as a further unknown quantity. We studied complex structures, such as salt domes or sedimentary basins and used the same constraints, irrespective of the inversion type (scaling function or gravity): we fixed the depth to the top for salt domes and basin-like structures. Given common criteria and constraints, the overall results obtained from the scaling

function results are promising since the error bars of the mean model are lower and the estimated distribution of the density contrast is narrower. In the case of real data analysis, the overall results obtained from the scaling function inversion in both the cases are promising. We estimated a reasonable depth (about 4 km) over the basin, in independent agreement with stratigraphic model. Future developments regard the interpretation of 3D sources and also the application of the method to magnetic data modelling.

CONCLUSIONS

In this thesis we presented a 2.x D MHODE inversion to interpret potential fields and to reconstruct complex geometric structures through the Scaling Function inversion.

In the MHODE framework we invert not the gravity data, but the scaling function (Fedi, 2007), which was introduced in Fedi, 2005 in the context of DEXP theory. This quantity does not depend on density or other physical constants, but only on the geometric characteristics of the model source. It is a dimensionless function of altitude that characterize the behaviour of homogeneity field. Once we obtain a geometrical model for the source, we can then obtain an average value of the density contrast by fitting the observed data vs. the data computed assuming the found geometrical model and a unit-density.

Our goal is to solve a 3D problem with MHODE; for this reason, we first studied a complex-source synthetic case, the *polyhedron*, whose field was computed by a code which I obtained converting to Matlab the original Fortran code realized by Tsoulis (2012). It allows calculating the gravitational potential, the field and its first-order derivative for a generic 3D polyhedral source model. However, the MHODE method would need also the first-order gravity field derivative. Being the calculus of the second-order vertical derivative for the polyhedral source very complex, I decided to use MHODE not for the 3D explicit case, but through inversion of several 2.x D sections. The so obtained depth models and the average density contrast were then used as a priori model for the 3D inversion with VOXEL method.

Even with this approach, I needed developing new formulas for the 2.x D inversion. In fact, MHODE was previously developed (Fedi et al. 2015) for 2D models only. In the 2D case we do not specify the length of the strike direction and consider the profile always symmetric with respect to the source. In this work, we implemented the MHODE method for the 2.5D and 2.x D cases. The 2.5D and 2.x D gravity formulas for arbitrary source sections were obtained by Shuey and Pasquale (1973), who slightly changed the well-known 2-D formulae of Talwani and Heirtzler (1964). However, to obtain the scaling function of orders $p = 1$ and $p = 2$, I calculated during my period at Aristotle University of Thessaloniki (under the guidance of Prof. Tsoulis), the second-order and third-order vertical derivatives of gravity field. These formulae have been developed for the magnetic case too.

In order to invert the scaling function quantity, we used the algorithm VFSA (Sen & Stoffa, 2013), which was very effective for MHODE inversion in the 2D case (Chauhan et al., 2018)

Once implemented the new 2.5D and 2.x D formulae of the field and its derivatives in the MHODE algorithm I tested the whole algorithm for a synthetic case. First, we created a 3D polyhedral model (Tsoulis, 2012) with a 1 g/cm^3 density. From the anomaly of this 3D model we extracted seven profiles and calculated the ridges of the gravity field and of its derivative for each profile. For any acceptable ridge we calculated the scaling function. During the inversion by VFSA algorithm we inverted this quantity and solved the equations system, with the unknowns being the geometric coordinates of vertices. Then, we obtained the final 2.x D model fixing the vertices of the top of the source (constraints from *a priori* information, e.g. from seismic interpretation) and leaving the vertices of the sides and bottom free to move in some prefixed bounded range. Once interpreted the obtained sections, these constitute the *a priori* information for the starting model in 3D inversion. The 3D inversion obtained with VOXI algorithm gave us the 3D density model, that is very close to the synthetic 3D model.

I used the 2.x D MHODE method also for the real case: we inverted the gravity data from a dataset in the Nevada Test Site (Ponce, 1997). We extracted 8 parallel profiles, crossing the minimum on the South-Eastern part of the map. Once extracted the profiles, we calculated the ridges of the gravity field and of the first order derivative of the field for each profile. For each acceptable ridge we calculated the scaling function. During the inversion by VFSA algorithm we inverted this quantity and solved the equations system with the unknowns being the geometric coordinates of vertices. The 2.x D MHODE inversion gives us an estimated density for each profile. So, we calculated the field and its derivative for the new 2.x D model, thanks to the estimated densities, and compared them with the observed gravity and its derivative fields. Then, we represented the final 2.x D models. From the 2.x D models (*a priori* conditions), we calculated the 2.x D density sections forming the starting model of the 3D inversion. By 3D inversion with VOXI algorithm we obtained the 3D density model and from this we calculated a map of distribution of the thickness of the basin, and a plot with the density contrast function. The 3D model defines well a basin of cenozoic deposits, of density lower than that of a paleozoic basement.

The main advantages of this method are:

1) We invert a quantity like the Scaling Function, that is correlated to the gravity field, which does not depend on density, and from its inversion we get geometric information of the investigated model

2) In contrast to the 2D modelling, it allows us to assume a finite strike direction length and so to manage the symmetry with respect to the body source in the most correct way.

3) The utilization of multiscale methods allows us to use ridges of the field derivatives

4) From the 2.x D inversion we may build density sections, manage better its geometry, thus having the opportunity to create a starting model for a 3D inversion.

A possible concern is that this method needs the forward problem to be formulated in terms of scaling function, which involves new mathematical and numerical formulations for the problem. This was an important part of this thesis (see Appendix A).

On the other hand, working with 2.x D sections allows a minor computational cost, guaranteeing in any case a consistent information that constitutes a reasonable starting model to use then in a full 3D inversion.

Future research may concern the development of the method for application to magnetic data and a full 3D MHODE inversion.

REFERENCES

Abbas, M.A., Fedi M. & Florio G., 2014, *Improving the local wavenumber method by automatic DEXP transformation*, Journal of Applied Geophysics, 111, 250 – 255, http://dx.doi.org/10.1016/j.jappgeo.2014.10.004.

Abbas, M.A. & Fedi M., 2014, *Automatic DEXP imaging of potential fields independent of the structural index*, Geophysical Journal International, 199, 1625-1632, http://dx.doi.org/10.1093/gji/ggu354.

Baniamerian, J., Fedi M. & Oskooi B., 2016, *Compact depth from extreme points: A tool for fast potential field imaging*, Geophysical Prospecting, 64, no. 5, 1386-1398, http://dx.doi.org/10.1111/1365-2478.12365.

Barbosa, V.C.F., Silva J.B.C. & Medeiros W.E., 2002, *Practical applications of uniqueness theorems in gravimetry: Part II — Pragmatic incorporation of concrete geologic information*, Geophysics, 67, 795–800, http://dx.doi.org/10.1190/1.1484523.

Blakely, R., 1996, *Potential theory in gravity and magnetic applications*, Cambridge University Press.

Byers, F.M., Carr W.W., Orkild P., Quinliven W.D. & Sargent K.A., 1976, *Volcanic suites and related cauldrons of Timber Mountain-Oasis Valley caldera complex, southern Nevada*. U.S. Geol. Surv. Prof. Paper, 919.

Chauhan, M.S. & Fedi M., 2015, *Multiple source estimation from potential field data by the MHODE method*, 2015 SEG Annual Meeting, https://doi.org/10.1190/segam2015-5877038.1.

Chauhan, M.S., Fedi M. & Sen M.K., 2017, *Gravity Inversion by the MHODE Method – Application to a Salt Dome Case*, 79th EAGE Conference and Exhibition 2017 (1), 1-5, http://dx.doi.org/10.3997/2214-4609.201700561.

Chauhan, M.S., Fedi M. & Sen M.K., 2018, *Gravity inversion by the Multi-Homogeneity Depth Estimation method for investigating salt domes and complex sources*, Geophysical prospecting, 2018, 66, 175-191, http://dx.doi.org/10.1111/1365-2478.12603

Cole, J.C., Harris A.G. & Wahl R.R., 1997, *Sub-crop geologic map of pre-tertiary rocks in the Yucca Flat and Northern Frenchman flat areas, Nevada test site, Southern Nevada*, USGS Open-File Report 97-678, http://dx.doi.org/10.2172/1061.

Cordell, L. & Henderson R.G., 1968, *Iterative Three-Dimensional Solution of Gravity Anomaly Data Using a Digital Computer*, Geophysics, 33(4), 596–601.

Dettinger M.D., 1989, *Distribution of carbonate-rock aquifers in southern Nevada and the potential for their development summary of findings*, 1985-88: State of Nevada, Program for the study and testing of carbonate-rock aquifers in eastern and southern Nevada, Summary Report Number 1, 37 p.

Dimri, V., 1992, *Deconvolution and Inverse Theory- Application to geophysical problems*, Elsevier.

Ellis, R.G., 2012. *Iterative reweighted inversion*, Geosoft Technical Note. Retrieved from http://www.geosoft.com/products/voxi-earth-modelling/Fiterative-reweightinginversion.

Ellis, R.G., Diorio P.A. & Mac Leod I.N., 2013, *Auxiliary Information in Geophysical Inversion*, Geosoft Inc., ASEG Inversion Forum.

Fedi, M., Hansen P.C. & Paoletti V., 2005, *Analysis of depth resolution in potential-field inversion*, Geophysics, 70, no. 6, A1–A11, http://dx.doi.org/10.1190/1.2122408.

Fedi, M., 2005, DEXP: *A fast method to determine the depth to the sources of potential fields*, 75th Annual International Meeting, SEG, Expanded Abstracts, 684-687, http://dx.doi.org/10.1190/1.2144416.

Fedi, M., 2007, *DEXP: A fast method to determine the depth and the structural index of*

potential fields sources, Geophysics, 72, no. 1, I1–I11, http://dx.doi.org/10.1190/1.2399452.

Fedi, M., Florio G. & Quarta T., 2009, *Multiridge analysis of potential fields: Geometric method and reduced Euler deconvolution* Geophysics, 74(4), L53–L65, http://dx.doi.org/10.1190/1.3142722.

Fedi, M., Cella F., Quarta T. & Villani A., 2010, *2D continuous wavelet transform of potential fields due to extended source distributions*, Applied and Computational Harmonic Analysis, 28, no. 3, 320–337, http://dx.doi.org/10.1016/j.acha.2010.03.002.

Fedi, M. & Cascone L., 2011, *Composite continuous wavelet transform of potential fields with different choices of analyzing wavelets*, Journal of Geophysical Research, 116, B7, http://dx.doi.org/10.1029/2010JB007882.

Fedi, M. & Pilkington M., 2012, *Understanding imaging methods for potential field data*: Geophysics, 77(1), G13–G24, http://dx.doi.org/10.1190/geo2011-0078.1.

Fedi, M. & Florio G., 2013, *Determination of the maximum-depth to potential field sources by a maximum structural index method*, Journal of Applied Geophysics, 88, 154–160, http://dx.doi.org/10.1016/j.jappgeo.2012.10.009.

Fedi, M., Florio G. & Paoletti V., 2015, *MHODE: a local-homogeneity theory for improved source-parameter estimation of potential fields* Geophysical Journal International, 202, no. 2, 887-900, http://dx.doi.org/10.1093/gji/ggv185.

Fedi, M., 2016, Scaling laws in geophysics: *Application to potential fields of methods based on the laws of self-similarity and homogeneity*, in V. P. Dimri, *Fractal Solutions for Understanding Complex Systems in Earth Sciences*, Springe International, Cham, Switzerland, 1–18.

Ferguson, J.F., Felch R.N., Aiken C.L.V., Oldow J.S. & Dockery H., 1988, *Models of the Bouguer Gravity and Geologic Structure at Yucca Flat, Nevada*, Geophysics, Vol. 53, pp. 231–244.

Final Report, Processing and Acquisition of Air-FTG® Data Decorah, Iowa for United States Geological Survey (2013).

Florio, G. & Fedi M., 2014, *Multiridge Euler deconvolution*, Geophysical Prospecting, 62, no. 2, 333–351, http://dx.doi.org/10.1111/1365-2478.12078.

Florio, G. (2018), *Mapping the Depth to Basement by Iterative Rescaling of Gravity or Magnetic Data,* Journal of Geophysical Research: Solid Earth, 123, 9101-9120, https://doi.org/10.1029/2018JB015667

Florio, G. (2020), *The ITRESC Method of Basement Morphology Modelling: the Case of Yucca Flat (Nevada)*. In press.

Fueg, J.E. & Xia H., *Estimation of salt base depth using 3d gravity modeling: A case history from the Northern Gulf of Mexico*, 1996, SEG Technical Program Expanded Abstracts: 1384-1386, https://doi.org/10.1190/1.1826366.

Gelbaum, B.R. & Olmsted J.M.H., 2003, *Counterexamples in Analysis*, Courier Corporation.

Gerovska, D., Stavrev P. & Arauzo-Bravo M.J., 2005, *Finite difference Euler deconvolution algorithm applied to the interpretation of magnetic data from Northern Bulgaria*, Pure and Applied Geophysics, 162, 591– 608.

Goetze, H.J. & Lahmeyer B., 1988, *Application of three-dimensional interactive modelling in gravity and magnetics,* Geophysics. vol. 53, 1096-1108, 12 figs.,1 table.

Hansen, R.O., 1999, *An analytical expression for the gravity field of a polyhedral body with linearly varying density*, geophysics, vol. 64, n. 1, 75-77.

Healey, D.L., 1966, *Gravity and seismic study of Yucca Flat, Nevada Test Site, Nye County, Nevada*, In Harrison, D.A. and others (eds.), Mining Geophysics: Case Studies. Society of Exploration Geophysicists, 1, 84-93.

Healey, D.L., Harris R.N., Ponce D.A. & Oliver H.W., 1987, *Complete Bouguer gravity map of the Nevada test site and vicinity, Nevada*, USGS Open-File Report 87-506.

Holstein, H. & Ketteridge B., 1996, *Gravimetric analysis of uniform polyhedral*, Geophysics, vol. 61, n. 2, 357-364, 6 figs., 5 tables.

Holstein, H., Sherratt E.M. & Reid A.B., 2007, *Gravimagnetic field tensor gradiometry formulas for uniform polyhedral*, SEG Technical Program Expanded Abstracts: 750-754, https://doi.org/10.1190/1.2792522.

Ingber, L., 1989, *Very fast simulated reanniling,* Mathematical and Computer Modeling, 12 (8), 967-993.

Ingber, L. & Rosen B., 1992, *Genetic algorithms and very fast simulated reannealing: a comparison*, Mathematical and Computer Modelling 16, 87–100.

Jachens, R.C. & Moring B.C., 1990, *Maps of the thickness of Cenozoic deposits and the isostatic residual gravity over basement for Nevada*, U.S. Geological Survey Open-File Report 90-404, 15 p., 2 plates, scale 1:1,000,000.

Jachens, R.C. & Griscom A., 1985, *An isostatic residual gravity map of California - A residual map for interpretation of anomalies from intracrustal sources*, in Hinze, W.J. ed., The utility of regional gravity and magnetic anomaly maps: Tulsa, Okla., Society of Exploration Geophysics, p. 347-360.

Keating, P. & Pilkington M., 2004, *Euler deconvolution of the analytic signal and its application to magnetic interpretation*, Geophysical Prospecting, 52, 165–182.

Kirkpatrick, S.C., Gelatt D. & Vecchi M.P., 1983, *Optimization by simulated annealing*, Science 220, 671-680.

Laczniak, R.J., Cole J.C., Sawyer D.A. & Trudeau D.A., 1996, *Summary of hydrogeologic controls on ground-water flow at the Nevada Test Site, Nye County, Nevada*, U.S. Geological Survey Water Resources Investigations Report 96-4109, 59 p.

Li, Y. & Oldenburg D.W., 1996, *3D inversion of magnetic data, Geophysics*, 61, 394–408, http://dx.doi.org/10.1190/1.1443968.

Menke, W., 1989. *Geophysical Data Analysis: Discrete Inverse Theory* Academic Press, p. 289.

Moraes R.A.V. & Hansen R.O., 2001, *Constrained inversion of gravity fields for complex 3-D structures*, Geophysics, vol. 66, n. 2, 501-510, 6 figs., 1 table.

Moreau, F., Gibert D., Holschneider M. & Saracco G., 1997, *Wavelet analysis of potential fields*, Inverse Problems, 13, no. 1, 165–178, http://dx.doi.org/10.1088/0266-5611/13/1/013.

Oldenburg, D.W, 1974, *The Inversion and Interpretation of Gravity Anomalies,* Geophysics, 39(4), 526–536

Paoletti, V., Ialongo S., Florio G., Fedi M. & Cella F., 2013, *Self-constrained inversion of potential fields*, Geophysical Journal International, 195, 854–869, http://dx.doi.org/10.1093/gji/ggt313.

Parker, R.L., 1977, *Understanding inverse theory: Annual Review of Earth and Planetary Science*, 5, 35–64, http://dx.doi.org/10.1146/annurev.ea.05.050177.000343.

Phelps, G.A., Langenheim V.E. & Jachens R.C., 1999, *Thickness of Cenozoic deposits of Yucca Flat inferred from gravity data, Nevada Test Site, Nevada*, U.S. Geological Survey Open-File Report 99-310, 32 p.

Phelps, G.A. & Graham S.E., 2002, *Preliminary gravity inversion model of Frenchman Flat basin, Nevada Test Site, Nevada*, USGS Open-File Report 02-363.

Pilkington, M., 1997, *3-D magnetic imaging using conjugate gradients*, Geophysics, 62, 1132–1142, http://dx.doi.org/10.1190/1.1444214.

Plouff, D., 1977, *Preliminary documentation for a FORTRAN program to compute gravity terrain corrections based on topography digitized on a geographic grid*, U.S. Geological Survey Open-File Report 77-535, 45 p.

Pohanka V., 1988, *Optimum expression for computation of the gravity field of a homogeneous polyhedral body*, Geophysical Prospecting 36,733-751.

Ponce, D.A., 1997, *Gravity data of Nevada*, U.S. Geological Survey Digital Data Series DDS-42, CD-ROM.

Ramspott, L.D., Braun R.L. & Wadleigh W.F., 1970, *Mineral composition, CO2 content, and grain density of drill hole samples from Yucca Flat, Nevada Test Site*, Lawrence Radiation Laboratory, University of California, Livermore; TID-4500, UC-51, Geology and Mineralogy.

Rasmussen, R. & Pedersen L.B., 1979, *End Corrections in Potential Field Modeling*, Geophysical Prospecting 27, 749-760.

Rautman, A.C., Flint L.E., Flint A.L. & Istok J.D., 1995, *Physical and hydrologic properties of outcrop samples from a nonwelded to welded tuff transition, Yucca Mountain, Nevada*, U. S. Geological Service, Water-Resources Investigations Report 95-4061.

Ravat, D., 1994, *Use of fractal dimension to determine the applicability of Euler's homogeneity equation for finding source locations of gravity and magnetic anomalies, in Proceedings of the Symposium on the Application of Geophysics to Engineering and Environmental problems*, Boston, Environmental and Engineering Geophysical Society, Englewood, CO, 41–53.

Ravat D., 1996, *Analysis of the Euler method and its applicability in environmental investigations,* Journal of Environmental and Engineering Geophysics, 1, 229–238.

Reid, A.B., Allsop J.M., Granser H., Millett A.J. & Somerton I.W., 1990, *Magnetic interpretation in three dimensions using Euler deconvolution*, Geophysics, 55, no. 1, 80– 91, http://dx.doi.org/10.1190/1.1442774.

Reynolds, J.M., 1997, *An Introduction to Applied and Environmental Geophysics*, Wiley.

Richardson R.M. & MacInnes S.C., 1989, *The Inversion of Gravity Data Into Three-Dimensional Polyhedral Model*, Journal of Geophysical Research, vol. 94, n. b6, 7555-7562.

Roy, L., Sen M.K., Stoffa P.L., McIntosh K. & Nakamura Y., 2005, *Joint inversion of first arrival travel time and gravity data*, J. Geophys.Eng. 2, 277 –289.

Sen, M.K. & Stoffa P.L., 1995, *Global Optimization Method in Geophysical Inversion*-1st edition: Elsevier.

Sen, M.K. & Stoffa P. L., 1996, *Bayesian inference, Gibbs' sampler, and uncertainty estimation in nonlinear geophysical inversion*, Geophys. Prospect. 44 (2), 313 –350.

Sen, M.K. & Stoffa P.L., 2013, *Global optimization method in geophysical inversion*-2nd edition: Cambridge University Press.

Sharma P. V., 1986, *Geophysical methods in geology*-2nd edition: Elsevier.

Shuey, R.T. & Pasquale A. S., 1973, *End corrections in magnetic profile interpretation*, Geophysics 38, 507-512.

Smith, R.A., 1961, *A uniqueness theorem concerning gravity fields*, Proceedings of the Cambridge Philosophical Society, 57, 865–870.

Smith, R.S., Thurston J.B., Dai T.F. & MacLeod I. N., 1998, *iSPI—the improved source parameter imaging method*, Geophysical Prospecting, 46, no. 2, 141–151, http://dx.doi.org/10.1046/j.1365-2478.1998.00084.x.

Snyder, D.B. & Healey D.L., 1983, *Interpretation of the Bouguer gravity map of Nevada, Tonopah sheet*, Nevada bureau of mines & geology, Report 38.

Steenland, N.C., 1968, *The geomagnetic gradiometer by Slack H.A., Lynch V.M. & Langan L.,* (Geophysics, October 1967, 877–892), Geophysics, 33, 680– 686, http://dx.doi.org/10.1190/1.1486915.

Talwani, M., Worzel J.L. & Landisman M., 1959, *Rapid gravity computations for two-dimensional bodies with application to the Mendocino submarine fracture zone*, Journal of Geophysical Research, 64, 49–59, http://dx.doi.org/10.1029/JZ064i001p00049.

Talwani M. & Ewing M., 1960, *Rapid Computation of gravitational attraction of three-dimensional bodies of arbitrary shape*, Geophysics, vol. XXV, n. 1, 203-225, 6 figs.

Talwani, M. & Heirtzler J., 1964, *Computation of magnetic anomalies caused by two-dimensional structures of arbitrary shape, in Computers in mineral industries*, part 1, Stanford Univ. Publ. Geol. Sci., vol. 9, 464-480.

Thompson, D.T., 1982, *EULDPH: a new technique for making computer-assisted depth estimates from magnetic data*, Geophysics, 47, 31–37, http://dx.doi.org/10.1190/1.1441278.

Thurston, J.B. & Smith R. S., 1997, *Automatic conversion of magnetic data to depth, dip, and susceptibility contrast using the SPI method*, Geophysics, 62, 807– 813, http://dx.doi.org/10.1190/1.1444190.

Tsoulis, D. & Petrovic S., *On the singularities of the gravity field of a homogeneous polyhedral body*, Geophysics, vol. 66, n°2, March - April 2001, 535-539.

Tsoulis, D., 2012, *Analytical computation of the full gravity tensor of a homogeneous arbitrarily shaped polyhedral source using line integrals*, Geophysics, vol. 77, n°2, March - April 2012, F1-F11.

United States Department of Energy, 1994, *United States nuclear tests, July 1945 through September 1992*, U.S. Department of Energy, Nevada Operations Office, DOE/NV-209 (rev. 14), 105 p.

Winograd, I.J. & Thordarson W., 1975, *Hydrogeologic and hydrogeochemical framework, south-central Great Basin, Nevada-California, with special reference to the Nevada Test Site*, U.S. Geological Survey Professional Paper 712-C, 126 p.

Wu, W. & Hu P., 2006, *Interactive 3D body inversion on gravity and magnetic data*, SEG Technical Program Expanded Abstracts: 924-927, https://doi.org/10.1190/1.2370407.

Zhdanov, M.S., 2002, *Geophysical inverse theory and regularization problems*, Elsevier.

Appendix A

Gravity case formulae

Here we show the detailed formulae of the second and third order derivative of the field for the symmetrical and asymmetrical cases.

A.1 Second-order 2.5D vertical derivative of gravity field:

$$\frac{\partial^2 g_z}{\partial z^2} = -2G\rho \sum_i \frac{\Delta x_i}{\Delta x_i^2 + \Delta z_i^2} \frac{\partial D}{\partial z} \tag{A.1}$$

where:

$$D = \Delta z_i \, log \frac{r_i(R_{i+1} + Y)}{r_{i+1}(R_i + Y)} - \Delta x_i \left(tan^{-1} \frac{u_{i+1} Y}{w_i R_{i+1}} - tan^{-1} \frac{u_i Y}{w_i R_i} \right) \tag{A.2}$$

Now we may write:

$$D = \Delta z_i C_1 - \Delta x_i C_2 + \Delta x_i C_3 \tag{A.3}$$

with:

$$C_1 = log \frac{r_i(R_{i+1} + Y)}{r_{i+1}(R_i + Y)} \tag{A.4}$$

$$C_2 = tan^{-1} \frac{u_{i+1} Y}{w_i R_{i+1}} \tag{A.5}$$

$$C_3 = tan^{-1}\frac{u_i Y}{w_i R_i} \tag{A.6}$$

So, we have:

$$\frac{\partial D}{\partial z} = \Delta z_i \frac{\partial C_1}{\partial z} - \Delta x_i \left(\frac{\partial C_2}{\partial z} - \frac{\partial C_3}{\partial z}\right) \tag{A.7}$$

with:

$$\frac{\partial C_1}{\partial z} = \frac{\left(\frac{-u_i \sin\varphi + w_i \cos\varphi}{r_i}\right)(R_{i+1} + Y) + r_i\left(\frac{-u_i \sin\varphi + w_i \cos\varphi}{R_i}\right)}{[r_{i+1}(R_i + Y)]} + \\ + \frac{-\left(r_i(R_{i+1} + Y)\right)}{\left(r_{i+1}(R_i + Y)\right)^2}\left(\left(\left(\frac{-u_{i+1} \sin\varphi + w_i \cos\varphi}{r_{i+1}}\right)(R_i + Y)\right) + r_{i+1}\left(\frac{-u_i \sin\varphi + w_i \cos\varphi}{R_i}\right)\right) \tag{A.8}$$

$$\frac{\partial C_2}{\partial z} = \frac{1}{1 + \left(\frac{u_{i+1} Y}{w_i R_{i+1}}\right)^2}\left\{\frac{-Y\sin\varphi}{w_i R_{i+1}} + \frac{-(u_{i+1} Y)}{(w_i R_{i+1})^2}\left[-\cos\varphi\, R_{i+1} + w_i\left(\frac{-u_{i+1} \sin\varphi + w_i \cos\varphi}{R_{i+1}}\right)\right]\right\} \tag{A.9}$$

$$\frac{\partial C_3}{\partial z} = \frac{1}{1 + \left(\frac{u_i Y}{w_i R_i}\right)^2}\left\{\frac{-Y\sin\varphi}{w_i R_i} + \frac{-(u_i Y)}{(w_i R_i)^2}\left[-\cos\varphi\, R_i + w_i\left(\frac{-u_i \sin\varphi + w_i \cos\varphi}{R_i}\right)\right]\right\} \tag{A.10}$$

A.2 Second-order 2.x D vertical derivative of gravity field:

$$\frac{\partial^2 g_z}{\partial z^2} = -G\rho\left\{\sum_i \frac{\Delta x_i}{\Delta x_i^2 + \Delta z_i^2}\frac{\partial D_2}{\partial z} + \sum_i \frac{\Delta x_i}{\Delta x_i^2 + \Delta z_i^2}\frac{\partial D_1}{\partial z}\right\} \tag{A.11}$$

D_2 Depends on the strike length Y_2:

$$D_2 = \Delta z_i \, log \frac{r_i(R_{i+1} + Y_2)}{r_{i+1}(R_i + Y_2)} - \Delta x_i \left(tan^{-1} \frac{u_{i+1} Y_2}{w_i R_{i+1}} - tan^{-1} \frac{u_i Y_2}{w_i R_i} \right) \tag{A.12}$$

Now we may write:

$$D_2 = \Delta z_i C_1 - \Delta x_i C_2 + \Delta x_i C_3 \tag{A.13}$$

with:

$$C_1 = log \frac{r_i(R_{i+1} + Y_2)}{r_{i+1}(R_i + Y_2)} \tag{A.14}$$

$$C_2 = tan^{-1} \frac{u_{i+1} Y_2}{w_i R_{i+1}} \tag{A.15}$$

$$C_3 = tan^{-1} \frac{u_i Y_2}{w_i R_i} \tag{A.16}$$

So, we have:

$$\frac{\partial D_2}{\partial z} = \Delta z_i \frac{\partial C_1}{\partial z} - \Delta x_i \left(\frac{\partial C_2}{\partial z} - \frac{\partial C_3}{\partial z} \right) \tag{A.17}$$

with:

$$\frac{\partial C_1}{\partial z} = \frac{\left(\frac{-u_i \sin\varphi + w_i \cos\varphi}{r_i} \right)(R_{i+1} + Y_2) + r_i \left(\frac{-u_i \sin\varphi + w_i \cos\varphi}{R_i} \right)}{[r_{i+1}(R_i + Y_2)]} + \tag{A.18}$$

$$+ \frac{-\left(r_i(R_{i+1} + Y_2)\right)}{\left(r_{i+1}(R_i + Y_2)\right)^2} \left(\left(\left(\frac{-u_{i+1} \sin\varphi + w_i \cos\varphi}{r_{i+1}} \right)(R_i + Y_2) \right) + r_{i+1} \left(\frac{-u_i \sin\varphi + w_i \cos\varphi}{R_i} \right) \right)$$

$$\frac{\partial C_2}{\partial z} = \frac{1}{1+\left(\frac{u_{i+1}Y_2}{w_i R_{i+1}}\right)^2}\left\{\frac{-Y_2 \sin\varphi}{w_i R_{i+1}} + \frac{-(u_{i+1}Y_2)}{(w_i R_{i+1})^2}\left[-\cos\varphi\, R_{i+1} + w_i\left(\frac{-u_{i+1}\sin\varphi + w_i\cos\varphi}{R_{i+1}}\right)\right]\right\} \quad \text{(A.19)}$$

$$\frac{\partial C_3}{\partial z} = \frac{1}{1+\left(\frac{u_i Y_2}{w_i R_i}\right)^2}\left\{\frac{-Y_2 \sin\varphi}{w_i R_i} + \frac{-(u_i Y_2)}{(w_i R_i)^2}\left[-\cos\varphi\, R_i + w_i\left(\frac{-u_i\sin\varphi + w_i\cos\varphi}{R_i}\right)\right]\right\} \quad \text{(A.20)}$$

where $R_i = (u_i^2 + w_i^2 + Y_2^2)^{1/2}$ and $R_{i+1} = (u_{i+1}^2 + w_i^2 + Y_2^2)^{1/2}$.

Similarly, D_1 will depend on the strike length Y_1:

$$D_1 = \Delta z_i \, log\frac{r_i(R_{i+1}+Y_1)}{r_{i+1}(R_i+Y_1)} - \Delta x_i\left(tan^{-1}\frac{u_{i+1}Y_1}{w_i R_{i+1}} - tan^{-1}\frac{u_i Y_1}{w_i R_i}\right) \quad \text{(A.21)}$$

We may write:

$$D_1 = \Delta z_i C_1 - \Delta x_i C_2 + \Delta x_i C_3 \quad \text{(A.22)}$$

with:

$$C_1 = log\frac{r_i(R_{i+1}+Y_1)}{r_{i+1}(R_i+Y_1)} \quad \text{(A.23)}$$

$$C_2 = tan^{-1}\frac{u_{i+1}Y_1}{w_i R_{i+1}} \quad \text{(A.24)}$$

$$C_3 = tan^{-1}\frac{u_i Y_1}{w_i R_i} \quad \text{(A.25)}$$

So, we have:

$$\frac{\partial D_1}{\partial z} = \Delta z_i \frac{\partial C_1}{\partial z} - \Delta x_i \left(\frac{\partial C_2}{\partial z} - \frac{\partial C_3}{\partial z}\right) \tag{A.26}$$

with:

$$\frac{\partial C_1}{\partial z} = \frac{\left(\frac{-u_i \sin\varphi + w_i \cos\varphi}{r_i}\right)(R_{i+1} + Y_1) + r_i \left(\frac{-u_i \sin\varphi + w_i \cos\varphi}{R_i}\right)}{[r_{i+1}(R_i + Y_1)]} + \tag{A.27}$$

$$+\frac{-\left(r_i(R_{i+1} + Y_1)\right)}{\left(r_{i+1}(R_i + Y_1)\right)^2}\left(\left(\left(\frac{-u_{i+1} \sin\varphi + w_i \cos\varphi}{r_{i+1}}\right)(R_i + Y_1)\right) + r_{i+1}\left(\frac{-u_i \sin\varphi + w_i \cos\varphi}{R_i}\right)\right)$$

$$\frac{\partial C_2}{\partial z} = \frac{1}{1 + \left(\frac{u_{i+1} Y_1}{w_i R_{i+1}}\right)^2}\left\{\frac{-Y_1 \sin\varphi}{w_i R_{i+1}} + \frac{-(u_{i+1} Y_1)}{(w_i R_{i+1})^2}\left[-\cos\varphi\, R_{i+1} + w_i\left(\frac{-u_{i+1} \sin\varphi + w_i \cos\varphi}{R_{i+1}}\right)\right]\right\} \tag{A.28}$$

$$\frac{\partial C_3}{\partial z} = \frac{1}{1 + \left(\frac{u_i Y_1}{w_i R_i}\right)^2}\left\{\frac{-Y_1 \sin\varphi}{w_i R_i} + \frac{-(u_i Y_1)}{(w_i R_i)^2}\left[-\cos\varphi\, R_i + w_i\left(\frac{-u_i \sin\varphi + w_i \cos\varphi}{R_i}\right)\right]\right\} \tag{A.29}$$

where $R_i = (u_i^2 + w_i^2 + Y_1^2)^{1/2}$ and $R_{i+1} = (u_{i+1}^2 + w_i^2 + Y_1^2)^{1/2}$.

A.3 Third-order 2.5D vertical derivative of gravity field:

$$\frac{\partial^3 g_z}{\partial z^3} = -2G\rho \sum_i \frac{\Delta x_i}{\Delta x_i^2 + \Delta z_i^2} \frac{\partial D}{\partial z} \tag{A.30}$$

where:

$$D = \Delta z_i \frac{\partial C_1}{\partial z} - \Delta x_i \left(\frac{\partial C_2}{\partial z} - \frac{\partial C_3}{\partial z}\right) \tag{A.31}$$

and C_1, C_2, C_3 are given by equations (A.4) (A.5) (A.6) respectively.

So, we may write:

$$\frac{\partial C_1}{\partial z} = P_{1a} + P_{1b} \tag{A.32}$$

$$\frac{\partial C_2}{\partial z} = P_{2a} P_{2b} \tag{A.33}$$

$$\frac{\partial C_3}{\partial z} = P_{3a} + P_{3b} \tag{A.34}$$

where:

$$P_{1a} = \left(\frac{\left(\frac{-u_i \sin\varphi + w_i \cos\varphi}{r_i}\right)(R_{i+1} + Y) + r_i \left(\frac{-u_i \sin\varphi + w_i \cos\varphi}{R_i}\right)}{[r_{i+1}(R_i + Y)]} \right) \tag{A.35}$$

$$P_{1b} = \left[\frac{-\left(r_i (R_{i+1} + Y)\right)}{\left(r_{i+1}(R_i + Y)\right)^2} \left(\left(\left(\frac{-u_{i+1} \sin\varphi + w_i \cos\varphi}{r_{i+1}}\right)(R_i + Y) \right) + r_{i+1} \left(\frac{-u_i \sin\varphi + w_i \cos\varphi}{R_i}\right) \right) \right] \tag{A.36}$$

$$P_{2a} = \left(\frac{1}{1 + \left(\frac{u_{i+1} Y}{w_i R_{i+1}}\right)^2} \right) \tag{A.37}$$

$$P_{2b} = \frac{-Y sin\,\varphi}{w_i R_{i+1}} + \frac{-(u_{i+1} Y)}{(w_i R_{i+1})^2} \left[- cos\,\varphi\, R_{i+1} + w_i \left(\frac{-u_{i+1}\, sin\,\varphi + w_i\, cos\,\varphi}{R_{i+1}}\right) \right] \tag{A.38}$$

$$P_{3a} = \left(\frac{1}{1 + \left(\frac{u_i Y}{w_i R_i}\right)^2} \right) \tag{A.39}$$

$$P_{3b} = \frac{-Y sin\,\varphi}{w_i R_i} + \frac{-(u_i Y)}{(w_i R_i)^2}\left[- cos\,\varphi\, R_i + w_i \left(\frac{-u_i\, sin\,\varphi + w_i\, cos\,\varphi}{R_i} \right) \right] \tag{A.40}$$

So, we may write:

$$\frac{\partial P_{1a}}{\partial z} = \left(\frac{\left[\left[\left(\frac{\partial^2 r_i}{\partial z^2} \right)(R_{i+1} + Y) + \frac{\partial r_i}{\partial z}\frac{\partial R_{i+1}}{\partial z} \right] + \left[\frac{\partial r_i}{\partial z}\frac{\partial R_i}{\partial z} + r_i \left(\frac{\partial^2 R_i}{\partial z^2} \right) \right] \right] r_{i+1}(R_i + Y) - \left(\frac{\partial r_i}{\partial z}(R_{i+1} + Y) + r_i \frac{\partial R_i}{\partial z} \right)\left[\frac{\partial r_{i+1}}{\partial z}(R_i + Y) + r_{i+1}\frac{\partial R_{i+1}}{\partial z} \right]}{[r_{i+1}(R_i + Y)]^2} \right) \tag{A.41}$$

$$\frac{\partial P_{1b}}{\partial z} = -\frac{\left[\frac{\partial r_i}{\partial z}(R_{i+1} + Y) + r_i \frac{\partial R_{i+1}}{\partial z} \right]\left(r_{i+1}(R_i + Y) \right)^2 - \left(r_i(R_{i+1} + Y) \right)\left[2\left(r_{i+1}(R_i + Y) \right)\left[\frac{\partial r_{i+1}}{\partial z}(R_i + Y) + r_{i+1}\frac{\partial R_i}{\partial z} \right] \right]}{\left(r_{i+1}(R_i + Y) \right)^4} \left(\left(\frac{\partial r_{i+1}}{\partial z}(R_i + Y) \right) + r_{i+1}\frac{\partial R_i}{\partial z} \right) + \frac{-\left(r_i(R_{i+1} + Y) \right)}{\left(r_{i+1}(R_i + Y) \right)^2}\left[\frac{\partial^2 r_{i+1}}{\partial z^2}(R_i + Y) + \frac{\partial r_{i+1}}{\partial z}\frac{\partial R_i}{\partial z} \right] + \left[\frac{\partial r_{i+1}}{\partial z}\frac{\partial R_i}{\partial z} + r_{i+1}\frac{\partial^2 R_i}{\partial z^2} \right] \tag{A.42}$$

$$\frac{\partial P_{2a}}{\partial z} = -\frac{2\left(\frac{u_{i+1}Y}{w_i R_{i+1}}\right)\left(\frac{-\sin\varphi\, Y(w_i R_{i+1}) - (u_{i+1}Y)\left[-\cos\varphi\, R_{i+1} + w_i \frac{\partial R_{i+1}}{\partial z}\right]}{(w_i R_{i+1})^2}\right)}{\left[1 + \left(\frac{u_{i+1}Y}{w_i R_{i+1}}\right)^2\right]^2} \tag{A.43}$$

$$\frac{\partial P_{2b}}{\partial z} = -\frac{-(Y sin\,\varphi)\left[-cos\,\varphi\, R_{i+1} + w_i \frac{\partial R_{i+1}}{\partial z}\right]}{(w_i R_{i+1})^2} + \\ + \left[\begin{array}{l} \left(-\dfrac{(-sin\,\varphi\, Y)(w_i R_{i+1})^2 - (u_{i+1}Y)\left[2(w_i R_{i+1})(-cos\,\varphi\, R_{i+1}) + w_i \frac{\partial R_{i+1}}{\partial z}\right]}{(w_i R_{i+1})^4}\right) \\ \left(-cos\,\varphi\, R_{i+1} + w_i \dfrac{\partial R_{i+1}}{\partial z}\right) + \left(\dfrac{-(u_{i+1}Y)}{(w_i R_{i+1})^2}\right)\left(\begin{array}{c}\left(-cos\,\varphi \dfrac{\partial R_{i+1}}{\partial z}\right) + \\ \left(-cos\,\varphi \dfrac{\partial R_{i+1}}{\partial z} + w_i \dfrac{\partial^2 R_{i+1}}{\partial z^2}\right)\end{array}\right) \end{array}\right] \tag{A.44}$$

$$\frac{\partial P_{3a}}{\partial z} = -\frac{2\left(\frac{u_i Y}{w_i R_i}\right)\left(\frac{-\sin\varphi\, Y(w_i R_i) - (u_i Y)\left[-\cos\varphi\, R_i + w_i \frac{\partial R_i}{\partial z}\right]}{(w_i R_i)^2}\right)}{\left[1 + \left(\frac{u_i Y}{w_i R_i}\right)^2\right]^2} \tag{A.45}$$

$$\frac{\partial P_{3b}}{\partial z} = -\frac{-(Y sin\,\varphi)\left[-cos\,\varphi\, R_i + w_i \frac{\partial R_i}{\partial z}\right]}{(w_i R_i)^2} +$$

$$+\left[\begin{array}{l}\left(-\frac{(-sin\,\varphi\, Y)(w_i R_i)^2 - (u_i Y)\left[2(w_i R_i)(-cos\,\varphi\, R_i) + w_i \frac{\partial R_i}{\partial z}\right]}{(w_i R_{i+1})^4}\right) \\ \left(-cos\,\varphi\, R_i + w_i \frac{\partial R_i}{\partial z}\right) + \left(\frac{-(u_i Y)}{(w_i R_i)^2}\right)\left(\begin{array}{c}\left(-cos\,\varphi \frac{\partial R_i}{\partial z}\right) + \\ \left(-cos\,\varphi \frac{\partial R_i}{\partial z} + w_i \frac{\partial^2 R_i}{\partial z^2}\right)\end{array}\right)\end{array}\right] \quad \text{(A.46)}$$

where $\frac{\partial R_{i+1}}{\partial z} = \frac{-u_{i+1}\sin\varphi + w_i \cos\varphi}{R_{i+1}}$; $\quad \frac{\partial R_i}{\partial z} = \left(\frac{-u_i \sin\phi + w_i \cos\phi}{R_i}\right)$;

$\frac{\partial r_{i+1}}{\partial z} = \left(\frac{-u_{i+1}\sin\phi + w_i \cos\phi}{r_{i+1}}\right)$; $\quad \frac{\partial r_i}{\partial z} = \left(\frac{-u_i \sin\phi + w_i \cos\phi}{r_i}\right)$;

$$\frac{\partial^2 R_{i+1}}{\partial z^2} = -\frac{(-sin^2\varphi - cos^2\varphi)R_{i+1} - (u_{i+1} sin\,\varphi + w_i cos\,\varphi)\left(\frac{-u_{i+1} sin\,\varphi + w_i cos\,\varphi}{R_{i+1}}\right)}{{R_{i+1}}^2};$$

$$\frac{\partial^2 R_i}{\partial z^2} = -\frac{\left((-sin^2\varphi - cos^2\varphi)\right)R_i - (u_i sin\,\varphi + w_i cos\,\varphi)\left(\frac{-u_i sin\,\varphi + w_i cos\,\varphi}{R_i}\right)}{{R_i}^2};$$

A.4 Third-order 2.x D vertical derivative of gravity field:

$$\frac{\partial^3 g_z}{\partial z^3} = -G\rho\left\{\sum_i \frac{\Delta x_i}{\Delta x_i^2 + \Delta z_i^2}\frac{\partial D_2}{\partial z} + \sum_i \frac{\Delta x_i}{\Delta x_i^2 + \Delta z_i^2}\frac{\partial D_1}{\partial z}\right\} \quad \text{(A.47)}$$

D_2 Depends on the strike length Y_2:

$$D_2 = \Delta z_i \frac{\partial C_1}{\partial z} - \Delta x_i\left(\frac{\partial C_2}{\partial z} - \frac{\partial C_3}{\partial z}\right) \quad \text{(A.48)}$$

and C_1, C_2, C_3 are given by equations (A.14) (A.15) (A.16) respectively.

So, we may write:

(A.49)

$$\frac{\partial C_1}{\partial z} = P_{1a} + P_{1b}$$

$$\frac{\partial C_2}{\partial z} = P_{2a} P_{2b} \tag{A.50}$$

$$\frac{\partial C_3}{\partial z} = P_{3a} + P_{3b} \tag{A.51}$$

where:

$$P_{1a} = \left(\frac{\left(\frac{-u_i \sin\varphi + w_i \cos\varphi}{r_i} \right)(R_{i+1} + Y_2) + r_i \left(\frac{-u_i \sin\varphi + w_i \cos\varphi}{R_i} \right)}{[r_{i+1}(R_i + Y_2)]} \right) \tag{A.52}$$

$$P_{1b} = \left[\frac{-\left(r_i(R_{i+1} + Y_2)\right)}{\left(r_{i+1}(R_i + Y_2)\right)^2} \left(\left(\left(\frac{-u_{i+1} \sin\varphi + w_i \cos\varphi}{r_{i+1}} \right)(R_i + Y_2) \right) + r_{i+1} \left(\frac{-u_i \sin\varphi + w_i \cos\varphi}{R_i} \right) \right) \right] \tag{A.53}$$

$$P_{2a} = \left(\frac{1}{1 + \left(\frac{u_{i+1} Y_2}{w_i R_{i+1}} \right)^2} \right) \tag{A.54}$$

$$P_{2b} = \frac{-Y_2 sin\,\varphi}{w_i R_{i+1}} + \frac{-(u_{i+1} Y_2)}{(w_i R_{i+1})^2} \left[-cos\,\varphi\, R_{i+1} + w_i \left(\frac{-u_{i+1} sin\,\varphi + w_i cos\,\varphi}{R_{i+1}} \right) \right] \tag{A.55}$$

$$P_{3a} = \left(\frac{1}{1 + \left(\frac{u_i Y_2}{w_i R_i}\right)^2} \right) \tag{A.56}$$

$$P_{3b} = \frac{-Y_2 sin\,\varphi}{w_i R_i} + \frac{-(u_i Y_2)}{(w_i R_i)^2}\left[-cos\,\varphi\, R_i + w_i\left(\frac{-u_i\, sin\,\varphi + w_i\, cos\,\varphi}{R_i}\right)\right] \tag{A.57}$$

So, we may write:

$$\frac{\partial P_{1a}}{\partial z} = \left(\frac{\left[\left[\left(\frac{\partial^2 r_i}{\partial z^2}\right)(R_{i+1} + Y_2) + \frac{\partial r_i}{\partial z}\frac{\partial R_{i+1}}{\partial z}\right] + \left[\frac{\partial r_i}{\partial z}\frac{\partial R_i}{\partial z} + r_i\left(\frac{\partial^2 R_i}{\partial z^2}\right)\right]\right] r_{i+1}(R_i + Y_2) - \left(\frac{\partial r_i}{\partial z}(R_{i+1} + Y_2) + r_i\frac{\partial R_i}{\partial z}\right)\left[\frac{\partial r_{i+1}}{\partial z}(R_i + Y_2) + r_{i+1}\frac{\partial R_{i+1}}{\partial z}\right]}{[r_{i+1}(R_i + Y_2)]^2} \right) \tag{A.58}$$

$$\frac{\partial P_{1b}}{\partial z} =$$

$$= -\frac{\left[\frac{\partial r_i}{\partial z}(R_{i+1} + Y_2) + r_i\frac{\partial R_{i+1}}{\partial z}\right]\left(r_{i+1}(R_i + Y_2)\right)^2 - \left(r_i(R_{i+1} + Y_2)\right)\left[2\left(r_{i+1}(R_i + Y_2)\right)\left[\frac{\partial r_{i+1}}{\partial z}(R_i + Y_2) + r_{i+1}\frac{\partial R_i}{\partial z}\right]\right]}{\left(r_{i+1}(R_i + Y_2)\right)^4}\left(\left(\frac{\partial r_{i+1}}{\partial z}(R_i + Y_2)\right) + r_{i+1}\frac{\partial R_i}{\partial z}\right) + \tag{A.59}$$

$$+\frac{-\left(r_i(R_{i+1} + Y_2)\right)}{\left(r_{i+1}(R_i + Y_2)\right)^2}\left[\frac{\partial^2 r_{i+1}}{\partial z^2}(R_i + Y_2) + \frac{\partial r_{i+1}}{\partial z}\frac{\partial R_i}{\partial z}\right] + \left[\frac{\partial r_{i+1}}{\partial z}\frac{\partial R_i}{\partial z} + r_{i+1}\frac{\partial^2 R_i}{\partial z^2}\right]$$

$$\frac{\partial P_{2a}}{\partial z} = -\frac{2\left(\frac{u_{i+1}Y_2}{w_i R_{i+1}}\right)\left(\frac{-\sin\varphi\, Y_2(w_i R_{i+1}) - (u_{i+1}Y_2)\left[-\cos\varphi\, R_{i+1} + w_i \frac{\partial R_{i+1}}{\partial z}\right]}{(w_i R_{i+1})^2}\right)}{\left[1 + \left(\frac{u_{i+1}Y_2}{w_i R_{i+1}}\right)^2\right]^2} \tag{A.60}$$

$$\frac{\partial P_{2b}}{\partial z} = -\frac{-(Y_2 sin\,\varphi)\left[-cos\,\varphi\, R_{i+1} + w_i \frac{\partial R_{i+1}}{\partial z}\right]}{(w_i R_{i+1})^2} + \\ + \left[\begin{array}{l} \left(-\frac{(-sin\,\varphi\, Y_2)(w_i R_{i+1})^2 - (u_{i+1}Y_2)\left[2(w_i R_{i+1})(-cos\,\varphi\, R_{i+1}) + w_i \frac{\partial R_{i+1}}{\partial z}\right]}{(w_i R_{i+1})^4}\right) \\ \left(-cos\,\varphi\, R_{i+1} + w_i \frac{\partial R_{i+1}}{\partial z}\right) + \left(\frac{-(u_{i+1}Y_2)}{(w_i R_{i+1})^2}\right)\left(\begin{array}{c}\left(-cos\,\varphi \frac{\partial R_{i+1}}{\partial z}\right) + \\ \left(-cos\,\varphi \frac{\partial R_{i+1}}{\partial z} + w_i \frac{\partial^2 R_{i+1}}{\partial z^2}\right)\end{array}\right) \end{array}\right] \tag{A.61}$$

$$\frac{\partial P_{3a}}{\partial z} = -\frac{2\left(\frac{u_i Y_2}{w_i R_i}\right)\left(\frac{-\sin\varphi\, Y_2(w_i R_i) - (u_i Y_2)\left[-\cos\varphi\, R_i + w_i \frac{\partial R_i}{\partial z}\right]}{(w_i R_i)^2}\right)}{\left[1 + \left(\frac{u_i Y_2}{w_i R_i}\right)^2\right]^2} \tag{A.62}$$

$$\frac{\partial P_{3b}}{\partial z} = -\frac{-(Y_2 sin\,\varphi)\left[-cos\,\varphi\, R_i + w_i \frac{\partial R_i}{\partial z}\right]}{(w_i R_i)^2} +$$

$$+\left[\begin{array}{l} \left(-\frac{(-sin\,\varphi\, Y_2)(w_i R_i)^2 - (u_i Y_2)\left[2(w_i R_i)(-cos\,\varphi\, R_i) + w_i \frac{\partial R_i}{\partial z}\right]}{(w_i R_{i+1})^4}\right) \\ \left(-cos\,\varphi\, R_i + w_i \frac{\partial R_i}{\partial z}\right) + \left(\frac{-(u_i Y_2)}{(w_i R_i)^2}\right)\left(\begin{array}{c}\left(-cos\,\varphi \frac{\partial R_i}{\partial z}\right) + \\ \left(-cos\,\varphi \frac{\partial R_i}{\partial z} + w_i \frac{\partial^2 R_i}{\partial z^2}\right)\end{array}\right) \end{array}\right] \quad \text{(A.63)}$$

Similarly, D_1 will depend on the strike length Y_1:

$$D_1 = \Delta z_i \frac{\partial C_1}{\partial z} - \Delta x_i \left(\frac{\partial C_2}{\partial z} - \frac{\partial C_3}{\partial z}\right) \quad \text{(A.64)}$$

and C_1, C_2, C_3 are given by equations (A.23) (A.24) (A.25) respectively.

So, we may write:

$$\frac{\partial C_1}{\partial z} = P_{1a} + P_{1b} \quad \text{(A.65)}$$

$$\frac{\partial C_2}{\partial z} = P_{2a} P_{2b} \quad \text{(A.66)}$$

$$\frac{\partial C_3}{\partial z} = P_{3a} + P_{3b} \quad \text{(A.67)}$$

where:

$$P_{1a} = \left(\frac{\left(\frac{-u_i \sin\varphi + w_i \cos\varphi}{r_i}\right)(R_{i+1} + Y_1) + r_i \left(\frac{-u_i \sin\varphi + w_i \cos\varphi}{R_i}\right)}{[r_{i+1}(R_i + Y_1)]}\right) \quad \text{(A.68)}$$

$$P_{1b} = \left[\frac{-\left(r_i(R_{i+1}+Y_1)\right)}{\left(r_{i+1}(R_i+Y_1)\right)^2}\left(\left(\left(\frac{-u_{i+1}\sin\varphi + w_i\cos\varphi}{r_{i+1}}\right)(R_i+Y_1)\right) + r_{i+1}\left(\frac{-u_i\sin\varphi + w_i\cos\varphi}{R_i}\right)\right)\right] \quad \text{(A.69)}$$

$$P_{2a} = \left(\frac{1}{1+\left(\frac{u_{i+1}Y_1}{w_iR_{i+1}}\right)^2}\right) \quad \text{(A.70)}$$

$$P_{2b} = \frac{-Y_1 sin\,\varphi}{w_iR_{i+1}} + \frac{-(u_{i+1}Y_1)}{(w_iR_{i+1})^2}\left[-cos\,\varphi\,R_{i+1} + w_i\left(\frac{-u_{i+1}\,sin\,\varphi + w_i\,cos\,\varphi}{R_{i+1}}\right)\right] \quad \text{(A.71)}$$

$$P_{3a} = \left(\frac{1}{1+\left(\frac{u_iY_1}{w_iR_i}\right)^2}\right) \quad \text{(A.72)}$$

$$P_{3b} = \frac{-Y_1 sin\,\varphi}{w_iR_i} + \frac{-(u_iY_1)}{(w_iR_i)^2}\left[-cos\,\varphi\,R_i + w_i\left(\frac{-u_i\,sin\,\varphi + w_i\,cos\,\varphi}{R_i}\right)\right] \quad \text{(A.73)}$$

So, we may write:

$$\frac{\partial P_{1a}}{\partial z} = \left(\frac{\begin{array}{c}\left[\left[\left(\frac{\partial^2 r_i}{\partial z^2}\right)(R_{i+1}+Y_1) + \frac{\partial r_i}{\partial z}\frac{\partial R_{i+1}}{\partial z}\right] + \left[\frac{\partial r_i}{\partial z}\frac{\partial R_i}{\partial z} + r_i\left(\frac{\partial^2 R_i}{\partial z^2}\right)\right]\right] r_{i+1}(R_i+Y_1) - \\ -\left(\frac{\partial r_i}{\partial z}(R_{i+1}+Y_1) + r_i\frac{\partial R_i}{\partial z}\right)\left[\frac{\partial r_{i+1}}{\partial z}(R_i+Y_1) + r_{i+1}\frac{\partial R_{i+1}}{\partial z}\right]\end{array}}{[r_{i+1}(R_i+Y_1)]^2}\right) \quad \text{(A.74)}$$

$$\frac{\partial P_{1b}}{\partial z} =$$

$$= -\frac{\left[\frac{\partial r_i}{\partial z}(R_{i+1}+Y_1)+r_i\frac{\partial R_{i+1}}{\partial z}\right]\left(r_{i+1}(R_i+Y_1)\right)^2-\left(r_i(R_{i+1}+Y_1)\right)\left[2\left(r_{i+1}(R_i+Y_1)\right)\left[\frac{\partial r_{i+1}}{\partial z}(R_i+Y_1)+r_{i+1}\frac{\partial R_i}{\partial z}\right]\right]}{\left(r_{i+1}(R_i+Y_1)\right)^4}\left(\left(\frac{\partial r_{i+1}}{\partial z}(R_i+Y_1)\right)+\ r_{i+1}\frac{\partial R_i}{\partial z}\right)+ \quad \text{(A.75)}$$

$$+\frac{-\left(r_i(R_{i+1}+Y_1)\right)}{\left(r_{i+1}(R_i+Y_1)\right)^2}\left[\frac{\partial^2 r_{i+1}}{\partial z^2}(R_i+Y_1)+\frac{\partial r_{i+1}}{\partial z}\frac{\partial R_i}{\partial z}\right]+\left[\frac{\partial r_{i+1}}{\partial z}\frac{\partial R_i}{\partial z}+r_{i+1}\frac{\partial^2 R_i}{\partial z^2}\right]$$

$$\frac{\partial P_{2a}}{\partial z} = -\frac{2\left(\frac{u_{i+1}Y_1}{w_iR_{i+1}}\right)\left(\frac{-\sin\varphi\, Y_1(w_iR_{i+1})-(u_{i+1}Y_1)\left[-\cos\varphi\, R_{i+1}+w_i\frac{\partial R_{i+1}}{\partial z}\right]}{(w_iR_{i+1})^2}\right)}{\left[1+\left(\frac{u_{i+1}Y_1}{w_iR_{i+1}}\right)^2\right]^2} \quad \text{(A.76)}$$

$$\frac{\partial P_{2b}}{\partial z} = -\frac{-(Y_1 sin\,\varphi)\left[-cos\,\varphi\, R_{i+1}+w_i\frac{\partial R_{i+1}}{\partial z}\right]}{(w_iR_{i+1})^2}+$$

$$+\left[\begin{array}{l}\left(-\dfrac{(-sin\,\varphi\, Y_1)(w_iR_{i+1})^2-(u_{i+1}Y_1)\left[2(w_iR_{i+1})(-cos\,\varphi\, R_{i+1})+w_i\frac{\partial R_{i+1}}{\partial z}\right]}{(w_iR_{i+1})^4}\right) \\ \left(-cos\,\varphi\, R_{i+1}+w_i\dfrac{\partial R_{i+1}}{\partial z}\right)+\left(\dfrac{-(u_{i+1}Y_1)}{(w_iR_{i+1})^2}\right)\left(\begin{array}{c}\left(-cos\,\varphi\dfrac{\partial R_{i+1}}{\partial z}\right)+ \\ \left(-cos\,\varphi\dfrac{\partial R_{i+1}}{\partial z}+w_i\dfrac{\partial^2 R_{i+1}}{\partial z^2}\right)\end{array}\right)\end{array}\right] \quad \text{(A.77)}$$

$$\frac{\partial P_{3a}}{\partial z} = -\frac{2\left(\frac{u_i Y_1}{w_i R_i}\right)\left(\frac{-\sin\varphi\, Y_1(w_i R_i) - (u_i Y_1)\left[-\cos\varphi\, R_i + w_i \frac{\partial R_i}{\partial z}\right]}{(w_i R_i)^2}\right)}{\left[1 + \left(\frac{u_i Y_1}{w_i R_i}\right)^2\right]^2} \tag{A.78}$$

$$\frac{\partial P_{3b}}{\partial z} = -\frac{-(Y_1 sin\,\varphi)\left[-cos\,\varphi\, R_i + w_i \frac{\partial R_i}{\partial z}\right]}{(w_i R_i)^2} + \left[\begin{array}{l} \left(-\frac{(-sin\,\varphi\, Y_1)(w_i R_i)^2 - (u_i Y_1)\left[2(w_i R_i)(-cos\,\varphi\, R_i) + w_i \frac{\partial R_i}{\partial z}\right]}{(w_i R_{i+1})^4}\right) \\ \left(-cos\,\varphi\, R_i + w_i \frac{\partial R_i}{\partial z}\right) + \left(\frac{-(u_i Y_1)}{(w_i R_i)^2}\right)\left(\begin{array}{c} \left(-cos\,\varphi \frac{\partial R_i}{\partial z}\right) + \\ \left(-cos\,\varphi \frac{\partial R_i}{\partial z} + w_i \frac{\partial^2 R_i}{\partial z^2}\right) \end{array}\right) \end{array}\right] \tag{A.79}$$

where $\frac{\partial R_{i+1}}{\partial z} = \frac{-u_{i+1}\sin\varphi + w_i\cos\varphi}{R_{i+1}}$; $\frac{\partial R_i}{\partial z} = \left(\frac{-u_i\sin\phi + w_i\cos\phi}{R_i}\right)$;

$\frac{\partial r_{i+1}}{\partial z} = \left(\frac{-u_{i+1}\sin\phi + w_i\cos\phi}{r_{i+1}}\right)$; $\frac{\partial r_i}{\partial z} = \left(\frac{-u_i\sin\phi + w_i\cos\phi}{r_i}\right)$;

$$\frac{\partial^2 R_{i+1}}{\partial z^2} = -\frac{(-sin^2\varphi - cos^2\varphi)R_{i+1} - (u_{i+1}\,sin\,\varphi + w_i\,cos\,\varphi)\left(\frac{-u_{i+1}\,sin\,\varphi + w_i\,cos\,\varphi}{R_{i+1}}\right)}{{R_{i+1}}^2};$$

$$\frac{\partial^2 R_i}{\partial z^2} = -\frac{(-sin^2\varphi - cos^2\varphi)R_i - (u_i\,sin\,\varphi + w_i\,cos\,\varphi)\left(\frac{-u_i\,sin\,\varphi + w_i\,cos\,\varphi}{R_i}\right)}{{R_i}^2};$$

Magnetic case formulae

In the next lines we show all the terms that constitute the formulae of the first order derivative of the vertical component B_z of magnetic field for the symmetrical and asymmetrical cases. And the formula of the second order derivative of the vertical component B_z of magnetic field for the symmetrical case.

A.5 First-order 2.5D vertical derivative of the vertical component ΔB_z of magnetic field:

$$\frac{\partial B_z}{\partial z} = -2CmJ \sum_i \frac{\Delta x_i}{\Delta x_i^2 + \Delta z_i^2} \frac{\partial D}{\partial z} \tag{A.80}$$

where:

$$D = (j_x \Delta x_i + j_z \Delta z_i) \, log \frac{r_i (R_{i+1} + Y)}{r_{i+1}(R_i + Y)} - (j_x \Delta z_i - j_z \Delta x_i) \left(tan^{-1} \frac{u_{i+1} Y}{\omega_i R_{i+1}} - tan^{-1} \frac{u_i Y}{\omega_i R_i} \right) \tag{A.81}$$

Now we may write:

$$D = (j_x \Delta x_i + j_z \Delta z_i) C_1 - (j_x \Delta z_i - j_z \Delta x_i)(C_2 - C_3) \tag{A.82}$$

with:

$$C_1 = log \frac{r_i (R_{i+1} + Y)}{r_{i+1}(R_i + Y)} \tag{A.83}$$

$$C_2 = tan^{-1} \frac{u_{i+1} Y}{\omega_i R_{i+1}} \tag{A.84}$$

$$C_3 = tan^{-1}\frac{u_i Y}{\omega_i R_i} \tag{A.85}$$

So, we have:

$$\frac{\partial D}{\partial z} = (j_x \Delta x_i + j_z \Delta z_i)\frac{\partial C_1}{\partial z} + (j_x \Delta z_i - j_z \Delta x_i)\left(\frac{\partial C_2}{\partial z} - \frac{\partial C_3}{\partial z}\right) \tag{A.86}$$

with:

$$\frac{\partial C_1}{\partial z} = \frac{\left(\frac{-u_i \sin\varphi + w_i \cos\varphi}{r_i}\right)(R_{i+1} + Y) + r_i\left(\frac{-u_i \sin\varphi + w_i \cos\varphi}{R_i}\right)}{[r_{i+1}(R_i + Y)]} + \\ + \frac{-\left(r_i(R_{i+1} + Y)\right)}{\left(r_{i+1}(R_i + Y)\right)^2}\left(\left(\left(\frac{-u_{i+1} \sin\varphi + w_i \cos\varphi}{r_{i+1}}\right)(R_i + Y)\right) + r_{i+1}\left(\frac{-u_i \sin\varphi + w_i \cos\varphi}{R_i}\right)\right) \tag{A.87}$$

$$\frac{\partial C_2}{\partial z} = \frac{1}{1 + \left(\frac{u_{i+1} Y}{w_i R_{i+1}}\right)^2}\left\{\frac{-Y\sin\varphi}{w_i R_{i+1}} + \frac{-(u_{i+1} Y)}{(w_i R_{i+1})^2}\left[-\cos\varphi\, R_{i+1} + w_i\left(\frac{-u_{i+1} \sin\varphi + w_i \cos\varphi}{R_{i+1}}\right)\right]\right\} \tag{A.88}$$

$$\frac{\partial C_3}{\partial z} = \frac{1}{1 + \left(\frac{u_i Y}{w_i R_i}\right)^2}\left\{\frac{-Y\sin\varphi}{w_i R_i} + \frac{-(u_i Y)}{(w_i R_i)^2}\left[-\cos\varphi\, R_i + w_i\left(\frac{-u_i \sin\varphi + w_i \cos\varphi}{R_i}\right)\right]\right\} \tag{A.89}$$

A.6 First-order 2.x D vertical derivative of the vertical component ΔB_z of magnetic field:

In the magnetic case equation A.90, in contrast to the gravity case, we notice that the sign of the two parts of the strike length is not the same and in equation A.91 we have other two factors C_4 and C_5 that multiply the direction of magnetization along strike direction j_y.

$$\frac{\partial B_z}{\partial z} = -CmJ \sum_i \frac{\Delta x_i}{\Delta x_i^2 + \Delta z_i^2} \left[\frac{\partial D_2}{\partial z} - \frac{\partial D_1}{\partial z} \right] \tag{A.90}$$

D_2 Depends on the strike length Y_2:

$$\begin{aligned} D_2 = (j_x \Delta x_i + j_z \Delta z_i) \, log \frac{r_i (R_{i+1} + Y_2)}{r_{i+1}(R_i + Y_2)} + (j_x \Delta z_i - j_z \Delta x_i) \left(tan^{-1} \frac{u_{i+1} Y_2}{\omega_i R_{i+1}} - tan^{-1} \frac{u_i Y_2}{\omega_i R_i} \right) + \\ + j_y \left(-\frac{1}{2} log \frac{(R_{i+1} - u_{i+1})(r_{i+1} + u_{i+1})}{(R_{i+1} + u_{i+1})(r_{i+1} - u_{i+1})} + \frac{1}{2} log \frac{(R_i - u_i)(r_i + u_i)}{(R_i + u_i)(r_i - u_i)} \right) \end{aligned} \tag{A.91}$$

Now we may write:

$$D_2 = (j_x \Delta x_i + j_z \Delta z_i) C_1 + (j_x \Delta z_i - j_z \Delta x_i)(C_2 - C_3) + j_y \left(-\frac{1}{2} C_4 + \frac{1}{2} C_5 \right) \tag{A.92}$$

With:

$$C_1 = log \frac{r_i (R_{i+1} + Y_2)}{r_{i+1}(R_i + Y_2)} \tag{A.93}$$

$$C_2 = tan^{-1} \frac{u_{i+1} Y_2}{\omega_i R_{i+1}} \tag{A.94}$$

$$C_3 = tan^{-1}\frac{u_i Y_2}{\omega_i R_i} \tag{A.95}$$

$$C_4 = log\frac{(R_{i+1} - u_{i+1})(r_{i+1} + u_{i+1})}{(R_{i+1} + u_{i+1})(r_{i+1} - u_{i+1})} \tag{A.96}$$

$$C_5 = log\frac{(R_i - u_i)(r_i + u_i)}{(R_i + u_i)(r_i - u_i)} \tag{A.97}$$

So, we have:

$$\frac{\partial D_2}{\partial z} = (j_x\Delta x_i + j_z\Delta z_i)\frac{\partial C_1}{\partial z} + (j_x\Delta z_i - j_z\Delta x_i)\left(\frac{\partial C_2}{\partial z} - \frac{\partial C_3}{\partial z}\right) + j_y\left(-\frac{1}{2}\frac{\partial C_4}{\partial z} + \frac{1}{2}\frac{\partial C_5}{\partial z}\right) \tag{A.98}$$

with:

$$\frac{\partial C_1}{\partial z} = \frac{\left(\frac{-u_i\sin\varphi + w_i\cos\varphi}{r_i}\right)(R_{i+1} + Y_2) + r_i\left(\frac{-u_i\sin\varphi + w_i\cos\varphi}{R_i}\right)}{[r_{i+1}(R_i + Y_2)]} + \\ + \frac{-\left(r_i(R_{i+1} + Y_2)\right)}{\left(r_{i+1}(R_i + Y_2)\right)^2}\left(\left(\left(\frac{-u_{i+1}\sin\varphi + w_i\cos\varphi}{r_{i+1}}\right)(R_i + Y_2)\right) + r_{i+1}\left(\frac{-u_i\sin\varphi + w_i\cos\varphi}{R_i}\right)\right) \tag{A.99}$$

$$\frac{\partial C_2}{\partial z} = \frac{1}{1 + \left(\frac{u_{i+1}Y_2}{w_i R_{i+1}}\right)^2}\left\{\frac{-Y_2\sin\varphi}{w_i R_{i+1}} + \frac{-(u_{i+1}Y_2)}{(w_i R_{i+1})^2}\left[-\cos\varphi\, R_{i+1} + w_i\left(\frac{-u_{i+1}\sin\varphi + w_i\cos\varphi}{R_{i+1}}\right)\right]\right\} \tag{A.100}$$

$$\frac{\partial C_3}{\partial z} = \frac{1}{1+\left(\frac{u_i Y_2}{w_i R_i}\right)^2}\left\{\frac{-Y_2 \sin\varphi}{w_i R_i} + \frac{-(u_i Y_2)}{(w_i R_i)^2}\left[-\cos\varphi\, R_i + w_i\left(\frac{-u_i \sin\varphi + w_i \cos\varphi}{R_i}\right)\right]\right\} \quad \text{(A.101)}$$

For factor $\frac{\partial C_4}{\partial z}$ we have:

$$\frac{\partial C_4}{\partial z} = Q_1 + Q_2 \quad \text{(A.102)}$$

With:

$$Q_1 = \frac{\left(\frac{-u_{i+1}\sin\varphi + w_i \cos\varphi}{R_{i+1}} - (-\sin\varphi)\right)(r_{i+1}+u_{i+1})(R_{i+1}-u_{i+1}) + \left(\frac{-u_{i+1}\sin\varphi + w_i\cos\varphi}{r_{i+1}} + (-\sin\varphi)\right)}{(R_{i+1}+u_{i+1})(r_{i+1}-u_{i+1})} \quad \text{(A.103)}$$

$$Q_2 = \left.\begin{array}{r} -(R_{i+1}-u_{i+1})(r_{i+1}+u_{i+1})\left(\frac{-u_{i+1}\sin\varphi + w_i\cos\varphi}{R_{i+1}} + (-\sin\varphi)\right)(r_{i+1}-u_{i+1}) + \\ +(R_{i+1}+u_{i+1})\left(\frac{-u_{i+1}\sin\varphi + w_i\cos\varphi}{r_{i+1}} - (-\sin\varphi)\right) \end{array}\right/ [(R_{i+1}+u_{i+1})(r_{i+1}-u_{i+1})]^2 \quad \text{(A.104)}$$

And for factor $\frac{\partial C_5}{\partial z}$ we have:

$$\frac{\partial C_5}{\partial z} = Q_3 + Q_4 \quad \text{(A.105)}$$

With:

$$Q_3 = \frac{\left(\frac{-u_i \sin\varphi + w_i\cos\varphi}{R_i} - (-\sin\varphi)\right)(r_i+u_i)(R_i-u_i) + \left(\frac{-u_i\sin\varphi + w_i\cos\varphi}{r_i} + (-\sin\varphi)\right)}{(R_i+u_i)(r_i-u_i)} \quad \text{(A.106)}$$

$$Q_4 = \begin{matrix} -(R_i - u_i)(r_{i+1} + u_i)\left(\frac{-u_i \sin\varphi + w_i \cos\varphi}{R_{i+1}} + (-\sin\varphi)\right)(r_i - u_i) + \\ +(R_i + u_i)\left(\frac{-u_i \sin\varphi + w_i \cos\varphi}{r_i} - (-\sin\varphi)\right) \end{matrix} \Big/ [(R_i + u_i)(r_i - u_i)]^2 \quad \text{(A.107)}$$

where $R_i = (u_i^2 + w_i^2 + Y_2^2)^{1/2}$ and $R_{i+1} = (u_{i+1}^2 + w_i^2 + Y_2^2)^{1/2}$

Similarly, D_1 will depend on the strike length $-Y_1$:

$$D_1 = (j_x \Delta x_i + j_z \Delta z_i)\, log \frac{r_i\big(R_{i+1} + (-Y_1)\big)}{r_{i+1}\big(R_i + (-Y_1)\big)} + (j_x \Delta z_i - j_z \Delta x_i)\left(tan^{-1}\frac{u_{i+1}(-Y_1)}{\omega_i R_{i+1}} - tan^{-1}\frac{u_i(-Y_1)}{\omega_i R_i}\right) + j_y\left(-\frac{1}{2} log \frac{(R_{i+1} - u_{i+1})(r_{i+1} + u_{i+1})}{(R_{i+1} + u_{i+1})(r_{i+1} - u_{i+1})} + \frac{1}{2} log \frac{(R_i - u_i)(r_i + u_i)}{(R_i + u_i)(r_i - u_i)}\right) \quad \text{(A.108)}$$

Now we may write:

$$D_1 = (j_x \Delta x_i + j_z \Delta z_i) C_1 + (j_x \Delta z_i - j_z \Delta x_i)(C_2 - C_3) + j_y\left(-\frac{1}{2} C_4 + \frac{1}{2} C_5\right) \quad \text{(A.109)}$$

With:

$$C_1 = log \frac{r_i\big(R_{i+1} + (-Y_1)\big)}{r_{i+1}\big(R_i + (-Y_1)\big)} \quad \text{(A.110)}$$

$$C_2 = tan^{-1}\frac{u_{i+1}(-Y_1)}{\omega_i R_{i+1}} \quad \text{(A.111)}$$

$$C_3 = tan^{-1}\frac{u_i(-Y_1)}{\omega_i R_i} \quad \text{(A.112)}$$

$$C_4 = log\frac{(R_{i+1} - u_{i+1})(r_{i+1} + u_{i+1})}{(R_{i+1} + u_{i+1})(r_{i+1} - u_{i+1})} \tag{A.113}$$

$$C_5 = log\frac{(R_i - u_i)(r_i + u_i)}{(R_i + u_i)(r_i - u_i)} \tag{A.114}$$

So, we have:

$$\frac{\partial D_1}{\partial z} = (j_x\Delta x_i + j_z\Delta z_i)\frac{\partial C_1}{\partial z} + (j_x\Delta z_i - j_z\Delta x_i)\left(\frac{\partial C_2}{\partial z} - \frac{\partial C_3}{\partial z}\right) + j_y\left(-\frac{1}{2}\frac{\partial C_4}{\partial z} + \frac{1}{2}\frac{\partial C_5}{\partial z}\right) \tag{A.115}$$

with:

$$\frac{\partial C_1}{\partial z} = \frac{\left(\frac{-u_i\sin\varphi + w_i\cos\varphi}{r_i}\right)\left(R_{i+1} + (-Y_1)\right) + r_i\left(\frac{-u_i\sin\varphi + w_i\cos\varphi}{R_i}\right)}{\left[r_{i+1}\left(R_i + (-Y_1)\right)\right]} + \\ + \frac{-\left(r_i\left(R_{i+1} + (-Y_1)\right)\right)}{\left(r_{i+1}\left(R_i + (-Y_1)\right)\right)^2}\left(\left(\left(\frac{-u_{i+1}\sin\varphi + w_i\cos\varphi}{r_{i+1}}\right)\left(R_i + (-Y_1)\right)\right) + r_{i+1}\left(\frac{-u_i\sin\varphi + w_i\cos\varphi}{R_i}\right)\right) \tag{A.116}$$

$$\frac{\partial C_2}{\partial z} = \frac{1}{1 + \left(\frac{u_{i+1}(-Y_1)}{w_i R_{i+1}}\right)^2}\left\{\frac{-(-Y_1)\sin\varphi}{w_i R_{i+1}} + \frac{-\left(u_{i+1}(-Y_1)\right)}{(w_i R_{i+1})^2}\left[-\cos\varphi\, R_{i+1} + w_i\left(\frac{-u_{i+1}\sin\varphi + w_i\cos\varphi}{R_{i+1}}\right)\right]\right\} \tag{A.117}$$

$$\frac{\partial C_3}{\partial z} = \frac{1}{1 + \left(\frac{u_i(-Y_1)}{w_i R_i}\right)^2}\left\{\frac{-(-Y_1)\sin\varphi}{w_i R_i} + \frac{-\left(u_i(-Y_1)\right)}{(w_i R_i)^2}\left[-\cos\varphi\, R_i + w_i\left(\frac{-u_i\sin\varphi + w_i\cos\varphi}{R_i}\right)\right]\right\} \tag{A.118}$$

For the factor $\frac{\partial C_4}{\partial z}$ we have:

$$\frac{\partial C_4}{\partial z} = Q_1 + Q_2 \tag{A.119}$$

with:

$$Q_1 = \frac{\left(\frac{-u_{i+1}\sin\varphi + w_i\cos\varphi}{R_{i+1}} - (-\sin\varphi)\right)(r_{i+1}+u_{i+1})(R_{i+1}-u_{i+1}) + \left(\frac{-u_{i+1}\sin\varphi + w_i\cos\varphi}{r_{i+1}} + (-\sin\varphi)\right)}{(R_{i+1}+u_{i+1})(r_{i+1}-u_{i+1})} \tag{A.120}$$

$$Q_2 = \left.\begin{array}{r} -(R_{i+1}-u_{i+1})(r_{i+1}+u_{i+1})\left(\frac{-u_{i+1}\sin\varphi + w_i\cos\varphi}{R_{i+1}} + (-\sin\varphi)\right)(r_{i+1}-u_{i+1}) + \\ +(R_{i+1}+u_{i+1})\left(\frac{-u_{i+1}\sin\varphi + w_i\cos\varphi}{r_{i+1}} - (-\sin\varphi)\right) \end{array}\right/ [(R_{i+1}+u_{i+1})(r_{i+1}-u_{i+1})]^2 \tag{A.121}$$

And for the factor $\frac{\partial C_5}{\partial z}$ we have:

$$\frac{\partial C_5}{\partial z} = Q_3 + Q_4 \tag{A.122}$$

With:

$$Q_3 = \frac{\left(\frac{-u_i\sin\varphi + w_i\cos\varphi}{R_i} - (-\sin\varphi)\right)(r_i+u_i)(R_i-u_i) + \left(\frac{-u_i\sin\varphi + w_i\cos\varphi}{r_i} + (-\sin\varphi)\right)}{(R_i+u_i)(r_i-u_i)} \tag{A.123}$$

$$Q_4 = \left.\begin{array}{r} -(R_i-u_i)(r_{i+1}+u_i)\left(\frac{-u_i\sin\varphi + w_i\cos\varphi}{R_{i+1}} + (-\sin\varphi)\right)(r_i-u_i) + \\ +(R_i+u_i)\left(\frac{-u_i\sin\varphi + w_i\cos\varphi}{r_i} - (-\sin\varphi)\right) \end{array}\right/ [(R_i+u_i)(r_i-u_i)]^2 \tag{A.124}$$

where $R_i = (u_i^2 + w_i^2 + (-Y_1)^2)^{1/2}$ and $R_{i+1} = (u_{i+1}^2 + w_i^2 + (-Y_1)^2)^{1/2}$

A.7 Second-order vertical derivative of vertical component B_z of magnetic field for the symmetrical case:

$$\frac{\partial^2 B_z}{\partial z^2} = -2CmJ \sum_i \frac{\Delta_{x_i}}{\Delta_{x_i^2} + \Delta_{z_i^2}} \frac{\partial D}{\partial z} \tag{A.125}$$

where:

$$D = (j_x \Delta x_i + j_z \Delta z_i) \frac{\partial C_1}{\partial z} + (j_x \Delta z_i - j_z \Delta x_i) \left(\frac{\partial C_2}{\partial z} - \frac{\partial C_3}{\partial z} \right) \tag{A.126}$$

and C_1, C_2, C_3 are given by equations (A.83) (A.84) (A.85) respectively.

So, we may write:

$$\frac{\partial C_1}{\partial z} = P_{1a} + P_{1b} \tag{A.127}$$

$$\frac{\partial C_2}{\partial z} = P_{2a} P_{2b} \tag{A.128}$$

$$\frac{\partial C_3}{\partial z} = P_{3a} + P_{3b} \tag{A.129}$$

where:

$$P_{1a} = \left(\frac{\left(\frac{-u_i \sin \varphi + w_i \cos \varphi}{r_i} \right) (R_{i+1} + Y) + r_i \left(\frac{-u_i \sin \varphi + w_i \cos \varphi}{R_i} \right)}{[r_{i+1}(R_i + Y)]} \right) \tag{A.130}$$

$$P_{1b} = \left[\frac{-\left(r_i(R_{i+1}+Y)\right)}{\left(r_{i+1}(R_i+Y)\right)^2}\left(\left(\left(\frac{-u_{i+1}\sin\varphi + w_i\cos\varphi}{r_{i+1}}\right)(R_i+Y)\right) + r_{i+1}\left(\frac{-u_i\sin\varphi + w_i\cos\varphi}{R_i}\right)\right)\right] \quad \text{(A.131)}$$

$$P_{2a} = \left(\frac{1}{1+\left(\frac{u_{i+1}Y}{w_iR_{i+1}}\right)^2}\right) \quad \text{(A.132)}$$

$$P_{2b} = \frac{-Y sin\,\varphi}{w_iR_{i+1}} + \frac{-(u_{i+1}Y)}{(w_iR_{i+1})^2}\left[-cos\,\varphi\,R_{i+1} + w_i\left(\frac{-u_{i+1}\,sin\,\varphi + w_i\,cos\,\varphi}{R_{i+1}}\right)\right] \quad \text{(A.133)}$$

$$P_{3a} = \left(\frac{1}{1+\left(\frac{u_iY}{w_iR_i}\right)^2}\right) \quad \text{(A.134)}$$

$$P_{3b} = \frac{-Y sin\,\varphi}{w_iR_i} + \frac{-(u_iY)}{(w_iR_i)^2}\left[-cos\,\varphi\,R_i + w_i\left(\frac{-u_i\,sin\,\varphi + w_i\,cos\,\varphi}{R_i}\right)\right] \quad \text{(A.135)}$$

So, we may write:

$$\frac{\partial P_{1a}}{\partial z} = \left(\begin{array}{c}\left[\left[\left(\frac{\partial^2 r_i}{\partial z^2}\right)(R_{i+1}+Y) + \frac{\partial r_i}{\partial z}\frac{\partial R_{i+1}}{\partial z}\right] + \left[\frac{\partial r_i}{\partial z}\frac{\partial R_i}{\partial z} + r_i\left(\frac{\partial^2 R_i}{\partial z^2}\right)\right]\right] r_{i+1}(R_i+Y) - \\ -\left(\frac{\partial r_i}{\partial z}(R_{i+1}+Y) + r_i\frac{\partial R_i}{\partial z}\right)\left[\frac{\partial r_{i+1}}{\partial z}(R_i+Y) + r_{i+1}\frac{\partial R_{i+1}}{\partial z}\right] \\ \hline [r_{i+1}(R_i+Y)]^2\end{array}\right) \quad \text{(A.136)}$$

$$\frac{\partial P_{1b}}{\partial z} = -\frac{\left[\frac{\partial r_i}{\partial z}(R_{i+1}+Y)+r_i\frac{\partial R_{i+1}}{\partial z}\right]\left(r_{i+1}(R_i+Y)\right)^2-\left(r_i(R_{i+1}+Y)\right)\left[2\left(r_{i+1}(R_i+Y)\right)\left[\frac{\partial r_{i+1}}{\partial z}(R_i+Y)+r_{i+1}\frac{\partial R_i}{\partial z}\right]\right]}{\left(r_{i+1}(R_i+Y)\right)^4}\left(\left(\frac{\partial r_{i+1}}{\partial z}(R_i+Y)\right)+\ r_{i+1}\frac{\partial R_i}{\partial z}\right)+\frac{-\left(r_i(R_{i+1}+Y)\right)}{\left(r_{i+1}(R_i+Y)\right)^2}\left[\frac{\partial^2 r_{i+1}}{\partial z^2}(R_i+Y)+\frac{\partial r_{i+1}}{\partial z}\frac{\partial R_i}{\partial z}\right]+\left[\frac{\partial r_{i+1}}{\partial z}\frac{\partial R_i}{\partial z}+r_{i+1}\frac{\partial^2 R_i}{\partial z^2}\right] \tag{A.137}$$

$$\frac{\partial P_{2a}}{\partial z} = -\frac{2\left(\frac{u_{i+1}Y}{w_iR_{i+1}}\right)\left(\frac{-\sin\varphi\,Y(w_iR_{i+1})-(u_{i+1}Y)\left[-\cos\varphi\,R_{i+1}+w_i\frac{\partial R_{i+1}}{\partial z}\right]}{(w_iR_{i+1})^2}\right)}{\left[1+\left(\frac{u_{i+1}Y}{w_iR_{i+1}}\right)^2\right]^2} \tag{A.138}$$

$$\frac{\partial P_{2b}}{\partial z} = -\frac{-(Y\sin\varphi)\left[-\cos\varphi\,R_{i+1}+w_i\frac{\partial R_{i+1}}{\partial z}\right]}{(w_iR_{i+1})^2}+\left[\left(-\frac{(-\sin\varphi\,Y)(w_iR_{i+1})^2-(u_{i+1}Y)\left[2(w_iR_{i+1})(-\cos\varphi\,R_{i+1})+w_i\frac{\partial R_{i+1}}{\partial z}\right]}{(w_iR_{i+1})^4}\right)\left(-\cos\varphi\,R_{i+1}+w_i\frac{\partial R_{i+1}}{\partial z}\right)+\left(\frac{-(u_{i+1}Y)}{(w_iR_{i+1})^2}\right)\left(\left(-\cos\varphi\frac{\partial R_{i+1}}{\partial z}\right)+\left(-\cos\varphi\frac{\partial R_{i+1}}{\partial z}+w_i\frac{\partial^2 R_{i+1}}{\partial z^2}\right)\right)\right] \tag{A.139}$$

$$\frac{\partial P_{3a}}{\partial z} = -\frac{2\left(\frac{u_iY}{w_iR_i}\right)\left(\frac{-\sin\varphi\,Y(w_iR_i)-(u_iY)\left[-\cos\varphi\,R_i+w_i\frac{\partial R_i}{\partial z}\right]}{(w_iR_i)^2}\right)}{\left[1+\left(\frac{u_iY}{w_iR_i}\right)^2\right]^2} \tag{A.140}$$

$$\frac{\partial P_{3b}}{\partial z} = -\frac{-(Y sin\,\varphi)\left[-cos\,\varphi\, R_i + w_i \frac{\partial R_i}{\partial z}\right]}{(w_i R_i)^2} + \\ + \left[\begin{array}{l} \left(-\frac{(-sin\,\varphi\, Y)(w_i R_i)^2 - (u_i Y)\left[2(w_i R_i)(-cos\,\varphi\, R_i) + w_i \frac{\partial R_i}{\partial z}\right]}{(w_i R_{i+1})^4} \right) \\ \left(-\cos\varphi\, R_i + w_i \frac{\partial R_i}{\partial z}\right) + \left(\frac{-(u_i Y)}{(w_i R_i)^2}\right) \left(\begin{array}{c} \left(-\cos\varphi \frac{\partial R_i}{\partial z}\right) + \\ \left(-\cos\varphi \frac{\partial R_i}{\partial z} + w_i \frac{\partial^2 R_i}{\partial z^2}\right) \end{array} \right) \end{array}\right] \quad \text{(A.141)}$$

where:

$$\frac{\partial R_{i+1}}{\partial z} = \frac{-u_{i+1}\sin\varphi + w_i \cos\varphi}{R_{i+1}}; \frac{\partial R_i}{\partial z} = \left(\frac{-u_i \sin\varphi + w_i \cos\varphi}{R_i}\right);$$

$$\frac{\partial r_{i+1}}{\partial z} = \left(\frac{-u_{i+1}\sin\varphi + w_i \cos\varphi}{r_{i+1}}\right); \qquad \frac{\partial r_i}{\partial z} = \left(\frac{-u_i \sin\varphi + w_i \cos\varphi}{r_i}\right);$$

$$\frac{\partial^2 R_{i+1}}{\partial z^2} = -\frac{(-sin^2\varphi - cos^2\varphi)R_{i+1} - (u_{i+1} sin\,\varphi + w_i cos\,\varphi)\left(\frac{-u_{i+1} sin\,\varphi + w_i cos\,\varphi}{R_{i+1}}\right)}{{R_{i+1}}^2};$$

$$\frac{\partial^2 R_i}{\partial z^2} = -\frac{(-sin^2\varphi - cos^2\varphi)R_i - (u_i sin\,\varphi + w_i cos\,\varphi)\left(\frac{-u_i sin\,\varphi + w_i cos\,\varphi}{R_i}\right)}{{R_i}^2};$$